High Repetition Rate Fiber and Integrated Waveguide Femtosecond Lasers
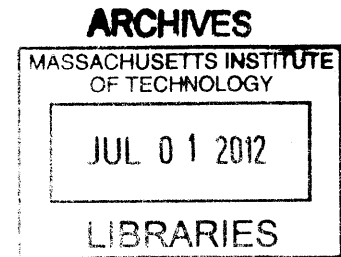
by

Michelle Y. Sander

M.S., Georgia Institute of Technology (2004)

Dipl.-Ing., TU Braunschweig (2006)

Submitted to the Department of Electrical Engineering and Computer Science
in partial fulfillment of the requirements for the degree of

Doctor of Philosophy

at the

MASSACHUSETTS INSTITUTE OF TECHNOLOGY

June 2012

© Massachusetts Institute of Technology 2012. All rights reserved.

Author . . . .
Department of Electrical Engineering and Computer Science
June 2012

Certified by . . . .
Erich P. Ippen
Elihu Thomson Professor of Electrical Engineering
Professor of Physics
Thesis Supervisor

Certified by . . . . :
Franz X. Kärtner
Adjunct Professor, Electrical Engineering and Computer Science
Thesis Supervisor

Accepted by . . . .
Leslie A. Kolodziejski
Chairman, Department Committee on Graduate Theses

High Repetition Rate Fiber and Integrated Waveguide Femtosecond Lasers

by

Michelle Y. Sander

Submitted to the Department of Electrical Engineering and Computer Science
on May 23, 2012, in partial fulfillment of the
requirements for the degree of
Doctor of Philosophy

Abstract

Femtosecond lasers and the development of frequency combs have revolutionized multiple fields like metrology, spectroscopy, medical diagnostics and optical communications. However, to enable wider adoption of the technology and new applications like photonic sampling, optical arbitrary waveform generation or the calibration of astronomical spectrographs, multi-GHz repetition rate femtosecond lasers with robust performance metrics, low cost, and a compact footprint are highly desirable.

In this thesis, different approaches to develop GHz mode-locked laser systems at telecommunication wavelengths are discussed and current achievements presented. Design aspects for constructing a long-term stable and compact fiber laser with 187 fs short pulses at a repetition rate of 1 GHz are covered. In order to scale the repetition rate into the multi-GHz regime, coherent pulse interleaving in novel thermally tunable waveguide interleavers is demonstrated at 10 GHz. A femtosecond erbium-doped waveguide laser is developed at GHz repetition rates and important design guidelines are provided. As saturable Bragg reflectors are crucial in all of the described systems to enable mode-locking, saturable absorber optimization is discussed and their optical performance compared. Thus, this research paves the way for compact, affordable high repetition rate fiber lasers and monolithically integrated femtosecond laser sources which can be combined on-chip with additional functionalities to develop novel photonic systems with impact on spectroscopy, sensing, telecommunications and biomedical applications.

Thesis Supervisor: Erich P. Ippen
Title: Elihu Thomson Professor of Electrical Engineering,
        Professor of Physics

Thesis Supervisor: Franz X. Kärtner
Title: Adjunct Professor, Electrical Engineering and Computer Science

Acknowledgments

With the completion of my PhD, I am particularly grateful to the inspiring faculty and colleagues I met during my years at MIT.

I would like to thank Prof. Franz Kärtner for providing me with the opportunity to conduct the fascinating femtosecond research presented in this thesis and I am grateful for his support. Throughout the years, I have valued his creative ideas, vast scientific knowledge and his inexhaustible research drive.

I would like to express my thanks to Prof. Erich Ippen and the insightful research advice and guidance I had the privilege to receive. His thoughtful appreciation for research inspired me throughout my PhD years and he has been a great mentor. I feel really fortunate to have received research advice by two such amazing professors.

It was a real pleasure to collaborate with Prof. Leslie Kolodziejski on the SBR research. I greatly appreciated her research and career advice and I would like to thank her for the continuous support throughout my graduate studies.

I would like to thank in particular the following colleagues for their contributions: Hyunil Byun who introduced me to the waveguide laser research. We worked closely together on the initial development of the 1 GHz butt-coupled Erbium-doped fiber laser. David Chao and Jonathan Morse for their help on fiber lasers. Gale Petrich for the growth and characterization of saturable Bragg reflectors. Ali Motamedi for pump-probe measurements of the SBRs. Marcus Dahlem for his expertise in thermal tuning of passive integrated devices. Sheila Nabanja and Orit Shamir for sharing their knowledge on SBR mounting, cleaving and lapping. Joseph Shmulovich and Sergey Frolov from CyOptics, Inc., for fabricating the interleaver and waveguide laser chips. Peter O'Brien from MIT Lincoln Labs for the deposition of the pump-reflective coating for the SBRs. Joseph Donnelly from MIT Lincoln Labs for discussions on proton-bombardment optimization. Helder Crespo, Andrew Benedick, Jonathan Birge, Li-Jin Chen for collaborations on Ti:sapphire numerical simulations. Cristian Antonelli, Jeff Chen, Eduardo Granados, Matt Grein, Jungwon Kim, Michael Peng, Ben Potsaid, Dominik Pudo, Jason Sickler, Katia Shtyrkova, and Jaime Viegas for inspiring

conversations.

I would really like to thank all my current and former colleagues in the Optics and Quantum Optics Group for the professional work environment, stimulating discussions, company in lab and long-lasting friendships.

I am grateful to Prof. Ippen, Prof. Kärtner, Prof. Kolodziejski, as well as Gale Petrich and Dorothy Fleischer, for their careful proofreading of my thesis and their feedback. I would also like to acknowledge my academic advisor, Prof. Karl Berggren, and the research collaboration with Prof. Michael Watts and his group members.

Thank you to Dorothy Fleischer and Donna Gale for keeping the group running smoothly and for their support on any purchase orders and travel reimbursements.

I am extremely grateful to all my friends for their wonderful friendship and support throughout this journey of graduate school, and I will cherish the memories of fun outings and precious times spent together. Sidney-Pacific, with Dottie and Roger Mark, and an amazing group of friends has truly been a home away from home for me. Last, but not least, I want to express my deepest gratitude to my family, my sister Christin and my parents, for their unwavering love and their support in all my endeavors.

Table of Contents

TABLE OF CONTENTS

List of Figures

18

List of Figures

List of Tables

List of Abbreviations

ADC	Analog to Digital Converter
ASE	Amplified Spontaneous Emission
CEO	Carrier-Envelope Offset
Cu	Copper
cw	Continuous Wave
DAC	Digital-to-Analog Converter
DWDM	Dense Wavelength Division Multiplexing
EDF	Erbium-doped Fiber
EDFA	Erbium-doped Fiber Amplifier
EDFL	Erbium-doped Fiber Laser
EPHI	Electronic-Photonic Heterogeneous Integration
Er	Erbium
FDTD	Finite-Difference Time-Domain
FSR	Free-Spectral Range
FWHM	Full-Width at Half Maximum

List of Abbreviations

Ge	Germanium
HMLL	Harmonically Mode-Locked Laser
HT	Hankel Transform
IAC	Interferometric Autocorrelation
IHT	Inverse Hankel Transform
IR	Infrared
LPCVD	Low Pressure Chemical Vapor Deposition
MBE	Molecular Beam Epitaxy
MF	Merit Function
MZI	Mach-Zehnder Interferometer
O-CDMA	Optical Code Division Multiple Access
OAWG	Optical Arbitrary Waveform Generation
OC	Output Coupler
PB	Proton Bombardment
PBS	Polarization Beam Splitter
PCB	Printed Circuit Board
PEF	Polarization Evolution Frequency
PI Controller	Proportional Integral Controller
PLVS	Polarization-Locked Vector Solitons
PM	Polarization Maintaining

24

List of Abbreviations

PRC	Pump-Reflective Coating
RF	Radio Frequency
RIN	Relative Intensity Noise
RMS	Root Mean Square
SBR	Saturable Bragg Reflector
SEM	Scanning Electron Microscopy
SPM	Self-Phase Modulation
SRIM	Stopping Range of Ions in Matter
SSB	Single Side-Band
TE	Transverse Electric
TEM	Transmission Electron Microscopy
TM	Transverse Magnetic
TRIM	Transport of Ions in Matter
WDM	Wavelength Division Multiplexer
WG	Waveguide
Yb	Ytterbium

List of Abbreviations

Chapter 1

Introduction

1.1 Background

Since the development of the first lasers that generated femtosecond (fs) pulses in the 1970s, their ultrashort pulse durations have fueled the technological innovations in a wide range of fields from spectroscopy and imaging to micromachining and medical diagnostics. Historic milestones include the first demonstration of sub-picosecond pulses in dye lasers by Shank and Ippen in 1974 [1], the development of a fiber soliton laser by Mollenauer [2], and the discovery of self-mode-locking in Ti:sapphire lasers by Sibbett [3] (for a more detailed overview, see [4, 5, 6]). Energy delivery is limited to ultrashort time durations in ultrafast lasers, thereby yielding high peak intensities. Sub-picosecond pulses enabled detailed studies of ultrafast carrier dynamics for the first time [7, 8] and allowed accurate manipulation of materials in micromachining applications [9, 10]. Medical surgery, especially eye care, has benefited from the higher precision control while related thermal damage to surrounding tissue has been greatly alleviated. Processes that rely on nonlinear effects, such as wavelength conversion or multi-photon absorption, are notably enhanced with femtosecond pulses. Thus, high-resolution imaging and multi-photon microscopy allow the examination of tissue morphologies down to $1\,\mu\mathrm{m}$ resolution. Recently, two-photon absorption was also applied to large-scale wafer inspection. The broadband spectrum of these pulses enables

27

next-generation telecommunication components that feature wider bandwidths by using multiple wavelengths in dense wavelength multiplexing or time-division multiplexing communications systems. Furthermore, this technology led to the development of femtosecond frequency combs which are generated by stabilizing the laser repetition rate and carrier-envelope phase offsets through active feedback control loops. Frequency combs constitute an absolute optical ruler that provides unprecedented wavelength accuracy and reproducibility and revolutionary optical clock applications, frequency metrology, and high resolution spectroscopy [11, 12].

While mode-locked solid-state and fiber lasers have established themselves at the forefront of broadband and low-jitter optical sources, their bulkiness, alignment sensitivity, and cost have prevented their direct integration into more portable applications. Therefore, to enable a wider adoption of the technology and new applications, such as optical sampling [13, 14, 15, 16], optical arbitrary waveform generation [17, 18, 19], or the calibration of astronomical spectrographs [20, 21, 22], low-cost multi-GHz repetition rate femtosecond devices with robust performance metrics, and a compact footprint are highly desirable. For widely spaced frequency comb lines, each frequency line is characterized by higher optical power (assuming the average total output power is constant when compared with a lower repetition rate comb), thus yielding an attractive source for spectroscopy and metrology applications.

In this work, we focus on obtaining few-fs pulses from compact high repetition rate lasers at telecommunication wavelengths near $1.55\,\mu$m in order to advance the following technologies.

1.1.1 Optical Arbitrary Waveform Generation (OAWG)

Pulse-shaping techniques, with which the user can modulate each frequency line individually, have found wide-spread interest and have been adopted as an enabling technology [17]. However, most current pulse-shapers have only limited performance capabilities, since

28

repetition rates of 10 GHz or higher are required to resolve the different optical lines, and, so far, only a small number of optical lines have been fully controlled [23].

However, with the rapid development of mode-locked lasers, ultra-short pulses and frequency comb technology can be leveraged to synthesize user-specific waveforms. By modulating the optical frequency lines in the spectral Fourier domain, the desired time-resolved waveform can be generated continuously over long periods of time. Based on phase-locked femtosecond oscillators, coherently interleaved arbitrary waveforms are attained by demultiplexing, modulation and multiplexing with appropriate integrated encoders and decoders, as shown in Fig. 1-1 [18, 19].
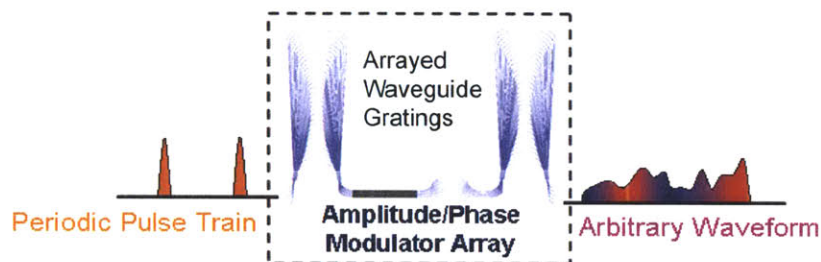
Figure 1-1: Optical Arbitrary Waveform Generation.

For a viable, user-friendly technology, the frequency lines must be individually separated in a compact manner, which can be achieved with integrated arrayed waveguide gratings for line spacings of 10 GHz or greater. This approach allows the phase and amplitude of each frequency component to be fully controlled in its own fast modulator, as illustrated in Fig. 1-2. The resulting pulses from the modulated and recombined frequency lines feature an arbitrary amplitude and phase with sub-femtosecond timing resolution. The goal is to modulate the amplitude and phase of fully stabilized optical frequency combs, which is referred to as full-field modulation. This direct control of all the individual optical lines allows line-by-line shaping instead of previous, resolution-limited pulse shaping of groups of lines [23]. The success of this technology relies on the generation of high repetition rate frequency combs. To obtain full control over individual lines with existing infrastructure, the line spacing must be matched to the grating spacing and modulator bandwidths of 10 GHz

or higher. The superior performance characteristics of this technology, with potential signal bandwidths up to THz, promises a multitude of new applications.

Such an OAWG system can be of particular interest for high-resolution 3D imaging, ultrahigh resolution sensing (novel chemical sensing) or ultra-broadband optical communications. Moreover, the OAWG infrastructure can be applied to Dense Wavelength Division Multiplexing (DWDM) or Optical Code Division Multiple Access (O-CDMA) [24, 25].
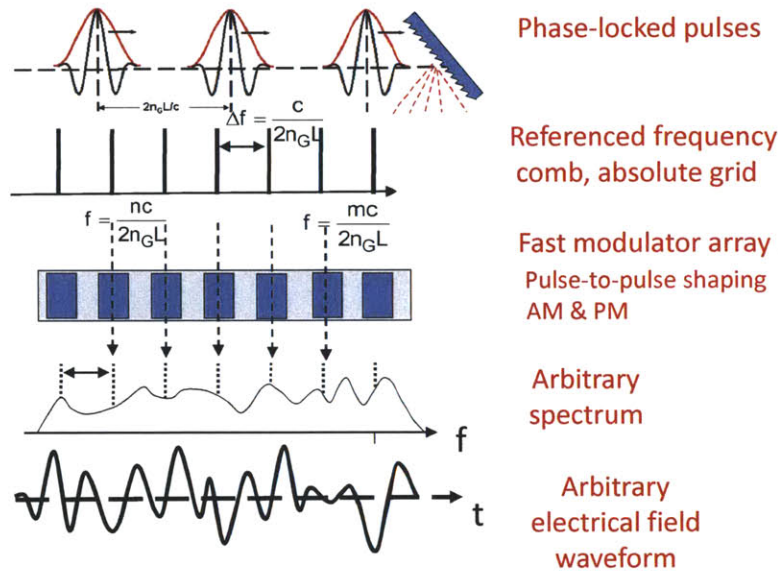
Figure 1-2: Principle of optical arbitrary waveform generation [19].

1.1.2 Photonic ADCs

In the past decades, the number of integrated circuits that contain digital systems has grown tremendously. One significant contributing factor to this rapid progress is the recent advance in analog-to-digital converter (ADC) technology, which converts continuous time information into digitized, binary encodable data streams. However, the performance of state-of-the-art electronic analog-to-digital converters for high-speed optical sampling is limited by the timing jitter, or aperture jitter, of the sampling signal [13, 14, 15]. These timing fluctuations in the sampling pulse lead to discretization errors, thus limiting the
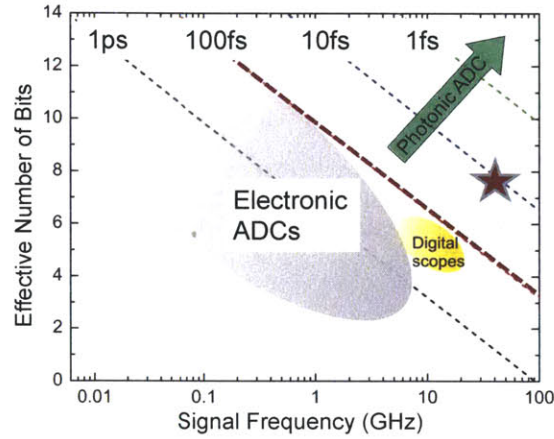
Figure 1-3: Current state of electronic/photonic ADCs based on a modified Walden plot [14]. The diagonal dotted lines indicate the associated timing jitter. The star marks the performance of our demonstrated photonic ADC [27].

effective numbers of bits that can be resolved. Currently, microwave sampling sources barely achieve timing jitters of $\sim 70\,\text{fs}$, although it can be challenging to maintain such low jitter continuously during the sampling process itself. In addition, these microwave sources typically are bulky due to the necessity of high-quality microwave cavities, which hinder their integration into a compact sampling system [16, 26].

Fig. 1-3 illustrates the performance of state-of-the-art electronic analog-to-digital converters, which is marked by the gray area. The resolution, which is measured in effective number of bits, is plotted against the input signal frequency. The dashed lines indicate the timing jitter of the sampling signal that is required to obtain a certain resolution for a specific sampling frequency. Further reduction of the jitter with the existing infrastructure becomes increasingly difficult, especially beyond gigahertz frequencies. However, this electronic bottleneck can be overcome with femtosecond laser systems which offer high timing precision of pulses with as little as sub-femtosecond timing jitter [28]. Thus, photonic ADCs based on femtosecond oscillators promise an enabling technology that can push ADC performance towards new performance horizons with higher sampling rates for wide-band signals and with better resolution. The star in Fig. 1-3 represents the resolution that was

recently achieved at a 40 GHz sampling speed with a photonic sampling system, developed in our group [27].

An important technology that can attain high sampling speeds is a compact, integratable femtosecond laser, with repetition rates of 1 GHz or higher. The overall sampling rate in such systems is determined by the repetition rate of the mode-locked laser multiplied by the number m of WDM channels, permitted by its bandwidth. The operating principle for such a sampling system, as shown in Fig. 1-4, consists of a chain of modulators, filters and detectors. The optical pulse train passes through either dispersive fiber (or a demultiplexer in the discrete case) in order to establish a time-to-wavelength mapping. This optical signal is modulated with the radio frequency (RF) signal that is to be sampled. In another demultiplexer, or ring filter in integrated technology, the individually sampled pulses at different colors/wavelengths are detected. The pulse amplitude then represents the RF signal values for the temporal positions.
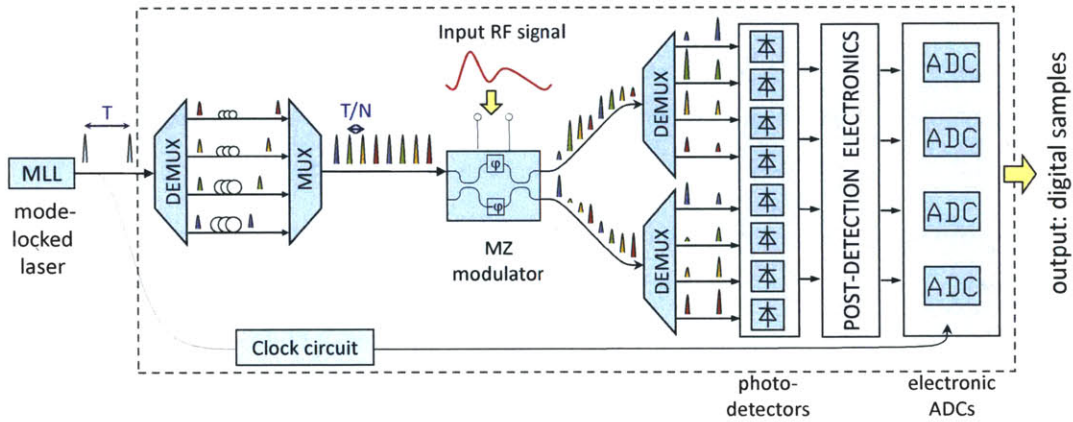
Figure 1-4: Schematic of a discrete photonic ADC system with a fiber-coupled, off-chip mode-locked laser source [27].

After electronic post-processing and AD conversion for each individual channel in electronic ADCs, which are clocked at the laser's repetition rate, the digital samples are effectively determined at an aggregate real-time sampling rate of $m \cdot f_{rep}$. This approach utilizes slow, but precise AD electronic converters in parallel to evaluate the individual channels,

while maintaining an overall data rate in the multi-GHz range. Currently, all the individual elements, except for the mode-locked laser source, can be fully implemented in Si photonics. For more details, the reader is referred to [26, 27, 29, 30].

1.1.3 Frequency Combs for the Calibration of Astronomical Spectrographs

Another recently identified, exciting application for frequency combs is the calibration of astrophysical spectrographs [20, 21, 22]. Currently, most extrasolar planets (exoplanets or planets in other star systems) have been discovered through the radial velocity method where each planet-star system orbits around a common center of gravity. Thus, in the presence of extrasolar planets, the gravitational field of the planet exerts a force on the star, resulting in shifts of the position. For an Earth-bound observer this is translated into Doppler-shifted starlight. This effect causes the characteristic absorption lines in the star's spectrum to shift towards blue wavelengths when the planet is moving away from Earth, and to shift towards red wavelengths when the planet is approaching Earth (and the star is moving away). These shifts (e.g., a $\sim 5\,\mathrm{cm/s}$ for the sun's orbital velocity translates into a $\sim 125\,\mathrm{kHz}$ frequency shift) are measured and compared to a reference source with a wide bandwidth from the visible to the near infrared (IR) in order to identify planets in other star systems. This measurement allows astronomers to determine the orbital periodicity of the exoplanets and to find a lower estimate for the planet's mass. By utilizing frequency combs with their inherent high wavelength accuracy and long-term stability, the calibration resolution can be significantly enhanced. However, for the frequency comb to efficiently match the resolving power of spectrographs, a comb spacing of $10\,\mathrm{GHz}$ or higher are required. In addition, because comparisons are made against the center of gravity spectrum/weighted average of the individual frequency lines, the frequency comb teeth must exhibit uniform intensity over a broadband spectrum and have no asymmetrical side-modes.

1.1.4   Laser Source Requirements

Various applications that were mentioned in the previous sections set the framework for our laser development research. Essential to these technologies is a high-repetition rate, multi-GHz femtosecond laser oscillator with a compact footprint and robust performance metrics. Depending on the application, low timing jitter, turn-key operation, reduced sensitivity to environmental perturbations, and portability are additional desirable features for the femtosecond laser source. In order to have significant impact and to enable wide adoption, laser construction at an affordable price point with an ability to scale up fabrication has to be accomplished. In the following paragraphs, the challenges related to different specifications of the oscillator are summarized:

- **High repetition rate mode-locked sources**

  For higher repetition rates the comb spacing widens, thus providing easier access to individual teeth of the mode-locked laser spectrum by optical filter banks and modulators, which typically operate at ~ 10-$40\,\text{GHz}$. Thus, in order to successfully incorporate a frequency comb source with existing arrayed waveguide gratings, high repetition rates are required, with $10\,\text{GHz}$ marking the lower boundary. Another advantage is that a high repetition rate laser has a proportionately higher optical power per mode and, thus, an improved signal-to-noise ratio in the frequency domain, when assuming a constant average output power. Therefore, the goal of this thesis is to develop stable, compact laser sources with GHz repetition rates.

- **Femtosecond, low timing-jitter, and long-term stable sources**

  Timing jitter describes deviations from the regular temporal spacing between pulses; low timing jitter is desired for optical sampling in order to enable higher sampling resolution. Shorter pulse durations τ, reduce the timing jitter, as given by Eq. 1.1 (compare [16]):

$$\frac{d}{dt}\langle \Delta t_{ML}^2 \rangle = \tau^2 \cdot \frac{1}{W_{Pulse}} \cdot \frac{h\,\omega_C}{2\,\pi\,\tau_{Cav}} \tag{1.1}$$

Furthermore, the timing jitter is inversely proportional to the pulse energy W_{Pulse} and the cavity lifetime τ_{Cav}. Planck's constant h and the carrier frequency ω_C influence the timing jitter $\frac{d}{dt}\langle \Delta t_{ML}^2 \rangle$ as well. Since erbium-doped gain material features a long upper state lifetime of 8-10 ms, technical noise fluctuations (e.g., from the pump diode) can be suppressed, thus resulting in a lower timing jitter. Therefore, Er-doped lasers with high intracavity power and short pulse durations are attractive.

- **Compact, turn-key, and cost-efficient designs**

  While mode-locked lasers have enabled a multitude of promising new technologies, their application has so far been limited by their high cost, complex construction and rather bulky footprints. In order to facilitate market adoption and wide-spread penetration of this technology, compact, robust, turn-key, and cost-efficient laser sources are desired. Designing sources at telecommunication wavelengths allows taking advantage of commercially available and previously developed fiber-based telecommunication-grade components (e.g. wavelength division multiplexers (WDMs), fiber integrated couplers, and isolators).

1.2 Mode-Locking

Ultrashort pulses can be generated by placing an intracavity modulator into a laser resonator. This ensures that mode-locked operation is favored over cw lasing by providing a pulse-shaping mechanism. In order to obtain pulsed laser operation with short pulse durations, all longitudinal modes in a laser cavity must enter into a defined phase relationship. The superposition of these phase-coherent modes allows the generation of a periodically pulsed output in time whose pulse duration is inversely proportional to the frequency bandwidth that is given by the number of lasing modes. Though active and passive mode-locking mechanisms have been demonstrated, the shortest pulses have been achieved by passive mode-locking implementations.

In this thesis, passive mode-locking [31] will be employed to generate short pulse durations with good timing jitter and performance metrics. In these systems, the incident light

induces a nonlinear material response that directly modulates its own optical properties and leads to pulse formation.

A saturable absorber is a device with a nonlinear intensity response that modulates loss in the cavity. During propagation through a saturable absorber, the pulse undergoes temporal narrowing, and the net gain window or the curvature of the absorption modulation determines the pulse length. Different saturable absorber classes exist. A fast saturable absorber is characterized by a nonlinear transmission that is proportional to the pulse intensity. Fast saturable absorber mode-locking is needed when the laser gain medium relaxation time is long when compared to the cavity round-trip time [32]. So-called artificial absorbers (e.g., Kerr-lens mode-locking [3] in solid-state lasers, nonlinear polarization rotation, or additive mode-locking in fiber lasers [33]) directly modulate the absorber loss dynamics according to the pulse intensity. Semiconductor saturable absorbers usually have recovery times longer than the desired pulse duration, and dynamic gain saturation or some other rnonlinear effect is required to assist in the pulse shaping of slow saturable absorbers [34, 35].

The additional nonlinear effect utilized in the presented laser systems is soliton formation. Through the balance of self-phase modulation and anomalous second order dispersion, stable soliton pulses are formed. Fig. 1-5 illustrates how the interplay between self-phase modulation and anomalous dispersion provides an efficient pulse shaping mechanism. The intensity-dependent nonlinear refractive index imposes a nonlinear phase shift ϕ on the pulse. This translates into a varying instantaneous frequency ω in the temporal profile of the pulse, resulting in the illustrated frequency chirp. Thus, the pulse redistributes its energy since low frequencies are created in the leading edge of the pulse and high frequencies in the rear. Through this nonlinear four-wave mixing process, new frequency components are generated within the pulse, thus resulting in spectral broadening until a steady state is reached. In an anomalous dispersive medium, the high frequency wave packets (by self-phase modulation) at the back of the pulse have a chance to catch up with the pulse center, while the opposite effect occurs for the lower frequency components. This leads to temporal pulse shaping. Thus, soliton mode-locking exploits a balance between self-phase modula-
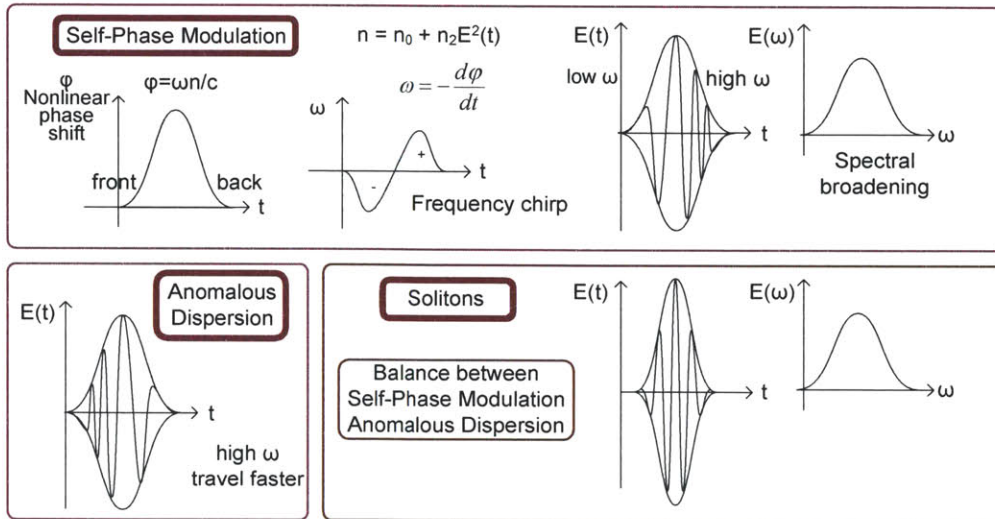
Figure 1-5: Schematic of the interplay of self-phase modulation and group delay dispersion used to form solitary pulses in the time and frequency domain.

tion and anomalous dispersion in order to generate temporally compressed pulses with a broadband spectrum. In this case, the absorber's role is to initiate mode-locking and to stabilize the pulses against continuum break-through [36].

Because fundamentally mode-locked lasers possess better noise properties and lower timing jitter than harmonically mode-locked oscillators, these lasers are the focus of this research. In order to scale cavities to higher repetition rates, the cavity dimensions must be reduced, which results in cavities with short pieces of gain fiber (10 GHz corresponds to a linear cavity length of 1 cm). Thus, the average power is limited by the overall absorbed pump power as well as the available gain, which is determined by the highest achievable doping concentration of the fiber [37].

The soliton area theorem, as shown in Eq. 1.2, governs pulse generation in soliton lasers [38]. If a laser operates with a given constant average power $P_{average}$, this translates into reduced peak power and reduced pulse energy for lasers with a higher repetition rate f_{rep}.

In addition, only limited nonlinearity δ can be exploited in the gain fiber. Thus, in order to maintain soliton operation with short pulse durations $\tau_{FWHM} = 1.76 \cdot \tau$ (assuming sech-pulse shapes), dispersion engineering is crucial, since the second order dispersion D of the fiber D_{Fiber} and the saturable Bragg reflector (SBR) D_{SBR} can make a significant contribution. Moreover, the SBR design must be optimized for low saturation fluences and short recovery times with good thermal properties.

$$W = 4 \cdot \frac{|D_{Fiber} + D_{SBR}|}{\delta \cdot \tau} = \frac{P_{average}}{f_{rep}} \tag{1.2}$$

1.3 Thesis Outline

This thesis describes different approaches that were pursued in order to develop high-repetition rate, femtosecond, compact mode-locked lasers with low timing jitter at $1.55\,\mu$m. The thesis is organized as follows.

- **Chapter 2: Erbium-doped Fiber Lasers**

  As erbium-doped fiber with high doping concentration is commercially available and as erbium lasers are characterized by low timing jitter, fundamentally mode-locked fiber lasers at repetition rates of 1 GHz and higher are designed. Developments in the fiber configuration are presented and the performance is analyzed in detail.

- **Chapter 3: External Repetition Rate Multiplication with Interleavers**

  Since the miniaturization of any fundamentally mode-locked laser eventually becomes limited by the minimum gain length that is required to maintain sufficient intracavity power in order to support mode-locking, methods to multiply the repetition rate externally to the laser cavity are studied. In this work, specifically repetition rate multiplication by compact, waveguide-based interleavers are investigated that can be used to scale a 625 MHz fiber laser to 10 GHz.

- **Chapter 4: Erbium-doped Waveguide Lasers**

  Erbium-doped glass waveguides on a silica platform provide an attractive alternative approach to building soliton mode-locked femtosecond sources, because of their additional robustness, compactness, capability for mass-production, and ease of integration with current chip fabrication. Therefore, integrated high-repetition rate systems are pursued in an on-chip waveguide implementation.

- **Chapter 5: Optimization of Semiconductor Saturable Bragg Reflectors (SBRs)**

  All the above-mentioned systems rely on SBRs to support self-starting and turn-key operation of the mode-locked laser. For high repetition rate laser systems, the SBRs must be carefully designed to provide the desired response for given operating parameters. Thus, SBR optimization aspects are discussed in detail.

- **Pulse Dynamics in Octave-Spanning Ti:Sapphire Lasers**

  As part of this thesis research, a temporal numerical analysis was performed that successfully predicted sub-two-cycle pulse duration in different octave-spanning Ti:Sapphire laser cavities. The model was further extended to analyze contributions to the carrier-envelope phase noise and to optimize intracavity output mirror designs. Because this work was published in detail, the reader is referred to the following publications:

  - M. Y. Sander, J. R. Birge, A. Benedick, H. M. Crespo, and F. X. Kärtner, "Dynamics of Dispersion Managed Octave-Spanning Titanium:Sapphire Lasers," *Journal of the Optical Society of America B* 26, 743-749 (2009), [39].

  - M. Y. Sander, E. P. Ippen, and F. X. Kärtner, "Carrier-Envelope Phase Dynamics of Octave-Spanning Dispersion-Managed Ti:Sapphire Lasers," *Optics Express* *18*, 4948-4960 (2010), [40].

  - L.-J. Chen, M. Y. Sander, and Franz X. Kärtner, "Kerr-Lens Mode Locking with Minimum Nonlinearity Using Gain-Matched Output Couplers," *Optics Letters* *35*, 2916-2918 (2010), [41].

Chapter 2

GHz SBR Mode-Locked Erbium-doped Fiber Lasers

Compact fiber laser cavities can be constructed based on soliton mode-locking with a semiconductor Bragg reflector (SBR) [36, 42, 43, 44]. Such fundamentally mode-locked fiber lasers are attractive femtosecond pulse sources due to their low timing jitter, robust performance metrics at moderate output powers, and compact configuration. In this chapter, the challenges of scaling these lasers towards higher repetition rates are addressed and several erbium-doped cavity configurations at repetition rates of 1 GHz and higher are presented.

2.1   Literature Overview

Conventional fiber lasers based on nonlinear polarization mode-locking [33] or carbon-nanotube saturable absorbers [45, 46, 47, 48] often employ up to meters of fiber in their cavity. Thus, these lasers operate, in general, at repetition rates in the MHz regime. Er/Yb glass lasers [49, 50], harmonically mode-locked lasers [51], and externally multiplied laser systems have approached repetition rates in the multi-GHz operating regime. Recently, fundamentally mode-locked fiber laser systems have been demonstrated which overcame the limited gain from commercially available Er-doped fibers by using specialty, highly doped

Er gain fibers. Fig. 2-1 gives an overview of the high-repetition rate erbium-doped fiber lasers to date. While some fiber lasers with GHz repetition rates at $1550\,\mu$m were demonstrated, most have failed to generate femtosecond pulses and did not provide a long-term stable output.

Fiber lasers with repetition rates up to 2 GHz were reported by McFerran *et al.* [52]. However, these lasers operated in the picosecond pulse regime with low average output power. Recent experimental demonstrations of fiber lasers that were mode-locked with SBRs achieved repetition rates as high as 3 GHz [53], but with similarly low efficiency; for 700 mW of launched pump power, only 2 mW of output power was obtained for a 2 % output coupling ratio. Carbon nanotube fiber lasers with a repetition rate of 5 GHz and a pulse duration of 0.68 ps were presented [54], but the timing jitter was much higher due to the longer pulse durations and lower intracavity pulse energy. An Er:Yb co-doped phosphosilicate fiber laser, mode-locked by carbon nanotubes from optical deposition on one of the cavity mirrors, reached record repetition rates of 10 GHz and 20 GHz [55] with 1.95-ps-long pulse durations. The only long-term stable fiber oscillator with femtosecond pulses that is based on commercially available gain fibers at wavelengths around $1.55\,\mu$m operated at a 500 MHz repetition rate in a butt-coupled SBR fiber laser cavity [56]. Thus, the goal is to scale this fiber laser further to higher repetition rates.

To achieve high-repetition rates, linear laser cavities, where the gain fiber is butt-coupled against a saturable absorber mirror, constitute a promising configuration. However, for any butt-coupled high-repetition rate laser, thermal management between the hot fiber core and the SBR is an important design parameter because thermal damage to the SBR was found to limit the long-term stability of the mode-locked laser output (in [53]). When the gain fiber was butt-coupled to the SBR, the hot fiber core was in direct contact with the SBR surface, which consequently was exposed to intense thermal heating. This can result in failure of the laser after a short period of operation or lead to a continuous performance degradation over time. Minimizing thermal damage is therefore particularly important for high repetition-rate fiber lasers to ensure long-term stable operation, as will be discussed in Section 2.3.4.

42

[1] Harmonic modelocking
800fs, 154GHz, Abedin et al.
[2] Er/Yb glass
1.6ps, 100GHz, Keller et al.

[3] 10GHz, 940fs, Yamashita et al.
[4] 3GHz, 600fs, Chen et al., MIT
[5] 2GHz, 3ps, McFerran et al.
[6] 491MHz, 180fs, Byun et al., MIT
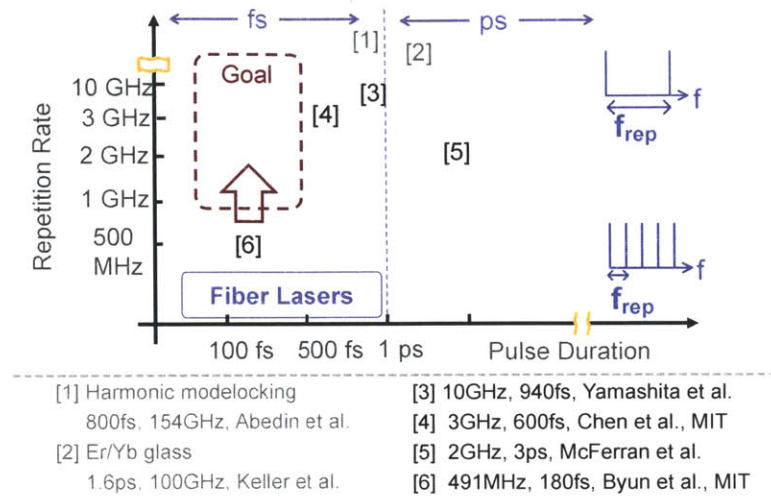
Figure 2-1: Landscape of previous work and target operating regimes for the desired laser sources. The numbers in black present previous work for fundamentally mode-locked lasers.

In this chapter, thermal damage of the saturable absorber is addressed, and a stable, efficient, low-jitter fiber laser with a repetition rate of 1 GHz is demonstrated. A soliton femtosecond laser source with sub-200-fs pulses was constructed in a compact all-fiber set-up with a reduced footprint of 121 mm x 94 mm x 33 mm.

2.2   Experimental Set-Up

In order to obtain soliton mode-locking, a highly-doped, anomalously dispersive, erbium gain fiber is desired. The commercially available Liekki Er80-8/125 gain fiber meets these conditions and can be fusion spliced with low loss (<0.2 dB) to regular SMF-28e fiber. Specialty erbium-ytterbium co-doped fibers (as demonstrated by [53, 55]) with higher doping concentration can be used with even shorter pieces of gain fiber to enable higher repetition rates. However, splicing and coupling into such phosphate fibers is more complicated and, in general, less efficient.

A 1 GHz erbium-doped fiber laser (EDFL) was devised whose experimental set-up is shown in Fig. 2-2. The fiber section of the laser cavity consists of a 92-mm-long Liekki Er80-8/125 erbium-doped gain fiber with anomalous dispersion of -20 fs^2/mm that was fusion-
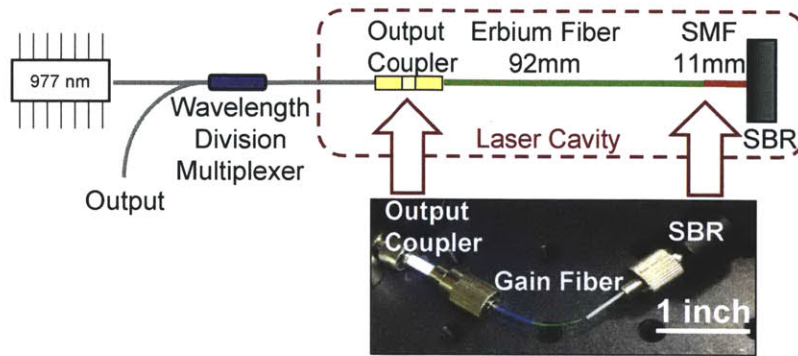
Figure 2-2: Schematic of 1 GHz laser cavity and actual fiber configuration.

spliced to an 11-mm-long piece of standard single-mode fiber (SMF-28e) in collaboration with Hyunil Byun. Different versions of these fiber assemblies were constructed, which featured a 7-mm-long SMF section combined with a 93-mm-long gain fiber section. The SMF physically separated the hot gain fiber core from direct contact with the SBR. In addition, the SMF-28e fiber slightly tapered the focus spot on the butt-coupled SBR from a mode-field diameter of $9.5\pm0.8\,\mu$m in the EDF to $10.4\pm0.8\,\mu$m in SMF. Both fiber ends were polished flat and the gain fiber was secured with epoxy in a $126\,\mu$m inner diameter zirconia ferrule. The length of the SMF-28e section was kept shorter than the ferrule length so that the splice resided within the ferrule for better mechanical stability. Since the splice joint slightly increased the fiber diameter compared to the bare fiber, the SMF fiber end was affixed with epoxy into a $127\,\mu$m inner diameter zirconia ferrule. A coated fiber ferrule served as a 10% output coupler and was connected to the gain fiber ferrule in a mating sleeve. The pump light was fiber-coupled through a wavelength division multiplexer (WDM) and transmitted through the output coupler into the gain fiber. With such a design, a robust and relatively low-loss connection was obtained when compared to free space coupling of the pump into the gain fiber. Fig. 2-3 shows photographs of two different packaged versions of the fiber laser with dimensions of 121 mm x 94 mm x 33 mm and 187 mm x 119 mm x 33 mm, respectively. Although the latter package is slightly larger, the laser is enclosed in an aluminum diecast so that it can be temperature controlled.
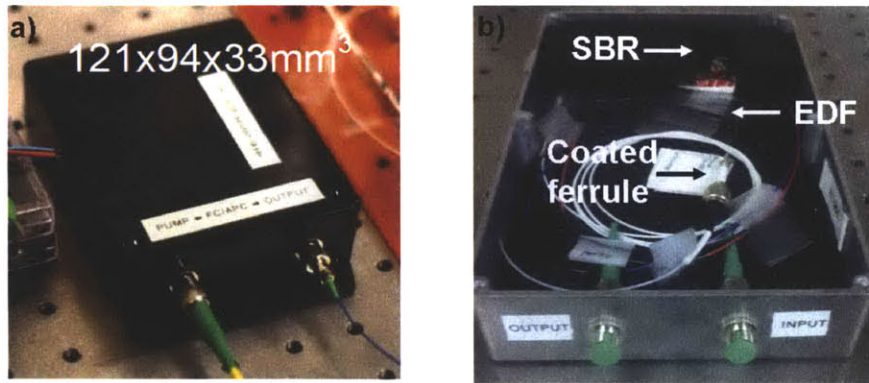
Figure 2-3: (a) EDFL package with dimensions of $12 \times 9 \times 3 \, \text{cm}^3$. (b) Open aluminum package with dimensions of $18 \times 12 \times 3 \, \text{cm}^3$ which allows external temperature stabilization.

The only non-fiber element in the cavity is a semiconductor saturable absorber mirror. The saturable Bragg reflector (SBR) facilitates mode-locking and self-starting operation of the laser. The SBR was butted directly against the fiber connector. If the butt-coupling contact was not optimized, intracavity losses could increase because small air gaps formed etalons that could impair the laser mode-locking. At the same time, this temporary attachment provided the flexibility to exchange the SBR, which would not be the case if the SBR were secured to the fiber connector with epoxy. The butt-coupling mechanism displayed in Fig. 2-4 provided optimized coupling. The SBR was indium-bonded or attached with silver epoxy to a 0.5 inch diameter Cu heat sink at the bottom of a lens tube. The fiber ferrule was mounted into a modified fiber connector adapter from whose surface the fiber ferrule protruded by $\sim 0.5 \, \text{mm}$, so that only the fiber ferrule established contact with the SBR surface and not the adapter plate. Monitoring the output power at low pump powers made it possible to optimize the butt-coupling for maximum efficiency.

The SBR was grown in Leslie Kolodziejski's group by Gale Petrich. The SBR combined a semiconductor saturable absorber section with a high reflectivity mirror, as illustrated in Fig. 2-5. The Bragg mirror, designed for a center wavelength of 1550 nm, consisted of a 22-pair quarter-wave stack of $Al_{0.95}Ga_{0.05}As$ and GaAs. On the surface of the high reflectivity
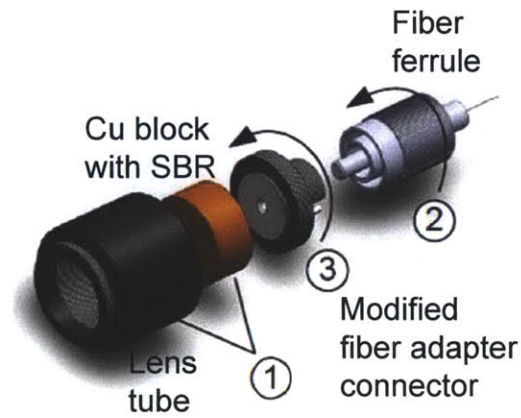
Figure 2-4: Current butt-coupling mechanism between SBR and fiber ferrule (adapted from Hyunil Byun). The numbers indicate the order of assembly for the individual components.
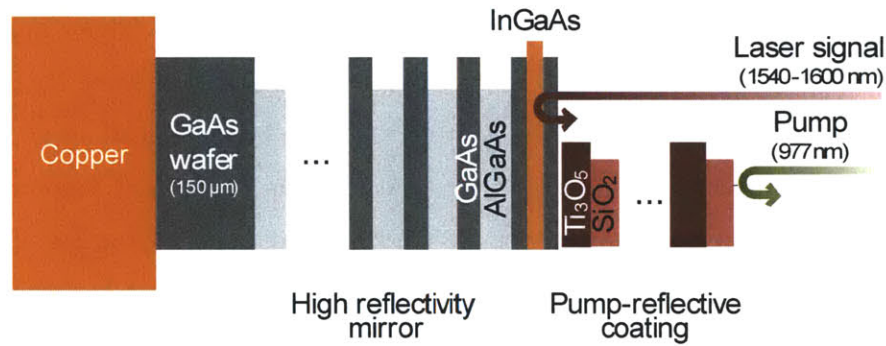
Figure 2-5: Schematic of SBR VA86 with pump-reflective coating.

mirror, an $In_{0.53}Ga_{0.47}As$ absorber was embedded in a half-wave cladding layer of GaAs. In order to reduce absorption of the residual pump power and to further minimize localized heating, a pump-reflective coating (PRC) was deposited on the front surface of the SBR. The quarter-wave layers of Ti_3O_5 and SiO_2 were centered at the pump wavelength of 980 nm. This addional dielectric coating reflected any residual pump power so that absorption of the pump light on the SBR was reduced, and the back-reflection increased the pump power light density in the cavity. A more detailed analysis of this coating (deposited by Peter O'Brien at Lincoln Labs) is found in Section 5.2.1.
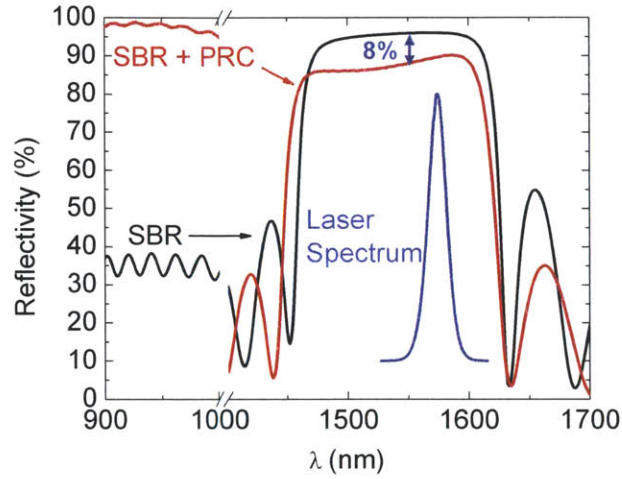
Figure 2-6: Reflectivity of SBR VA86 in red. With the pump-reflective coating, the reflectivity around 1550 nm decreases by 8 % and the pump light around 980 nm is reflected by 98 %. The bandwidth of the EDFL spectrum is depicted in blue.
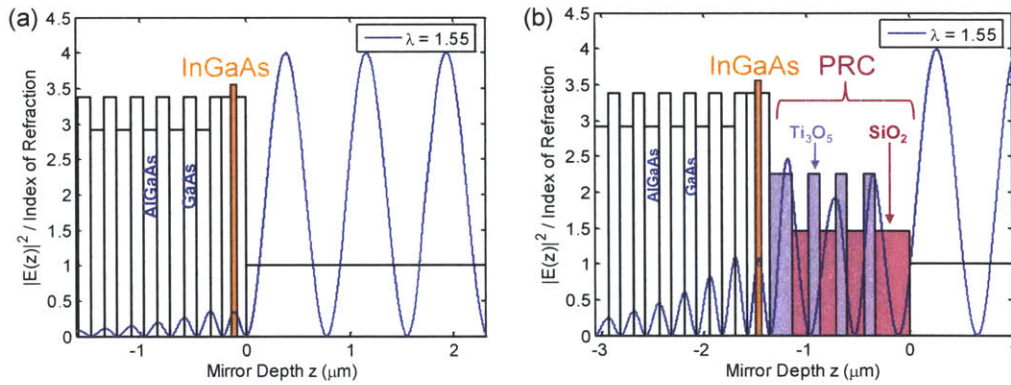
Figure 2-7: Standing wave E-field pattern for SBR VA86 (a) without coating and (b) with pump-reflective coating at a wavelength of 1.55 μm.

As seen in Fig. 2-6, the SBR (denoted by VA86) exhibited a measured reflectivity of 95% at 1560 nm, which was reduced to 88% after the deposition of the pump-reflective coating (photospectrometer reflectivity measurement). The added dielectric coating enhanced the standing electric field at least by a factor of two, as shown in Fig. 2-7, which compares the

field pattern for the uncoated and pump-reflective coated SBR VA86. The impact of the pump-reflective coating for the pump and signal wavelength for the electric wave pattern is shown in Fig. 2-8. At the pump wavelength of 980 nm, barely any light penetrated into the saturable absorber. For the signal wavelength at 1550 nm, the maximum of the electric field standing wave coincided directly with the absorber layer and increased significantly when compared to the regular VA86 SBR. The multi-layer structure, while designed for 980 nm, contributed slight resonant effects at 1550 nm that resulted in the field enhancement in the actual absorber layer. Thus, the PRC led to a higher modulation depth and a reduced saturation fluence.
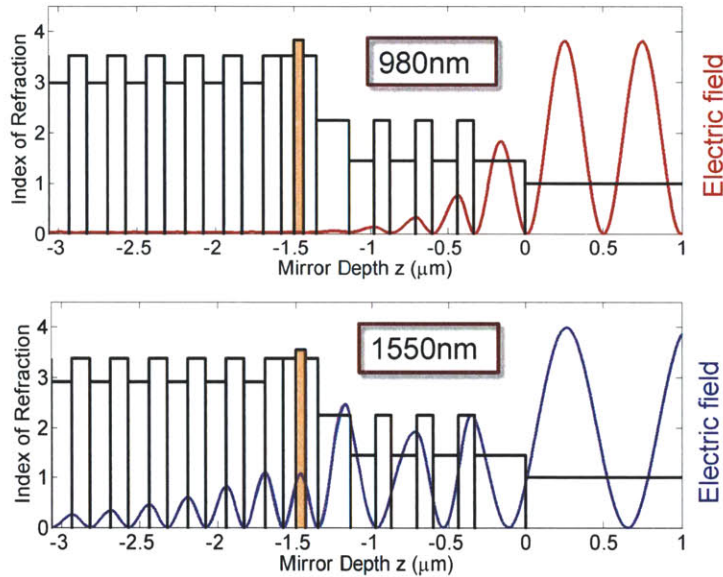
Figure 2-8: Standing electric wave field for the pump wavelength at 980 nm and the signal wavelength at 1550 nm for VA86 SBR with PRC. The pump light is efficiently reflected before penetrating the absorber.

Pump probe measurements performed by Ali Motamedi confirmed an enhanced modulation depth and a reduced saturation fluence after deposition of the pump-reflective coating. In Fig. 2-9, the measured reflectivity of the saturable absorber, with and without the pump-reflective coating, and as a function of the pump fluence at 1560 nm for 150 fs pulses (at
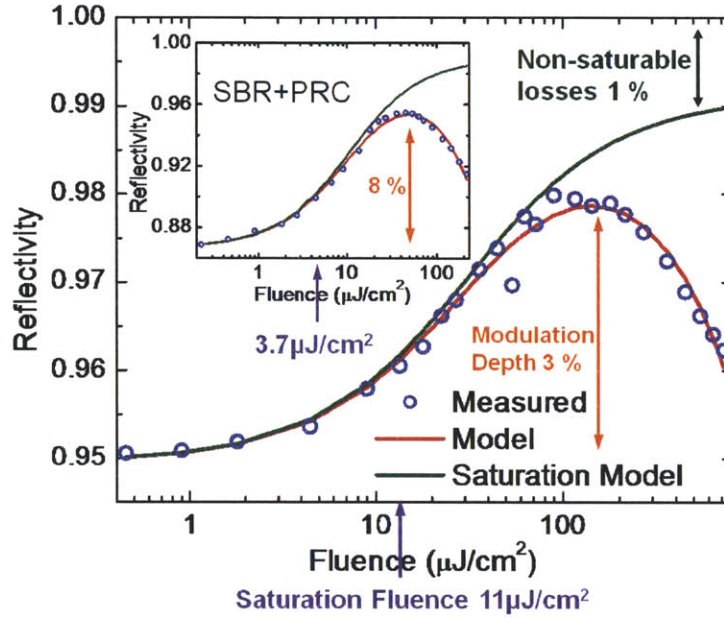
Figure 2-9: Pump probe results for SBR VA86 without the pump-reflective coating and with PRC as inset. The dots mark measured results.

a repetition rate of 80 MHz), is plotted. The solid line denotes the fit of a slow saturable-absorber model plus two-photon absorption to the measured data. While the SBR itself was characterized by 4% of saturable absorption, by 1% of non-saturable loss and a saturation fluence of $11\,\mu\mathrm{J/cm}^2$, the SBR with the PRC exhibited an increased saturable absorption of 8%, non-saturable losses around 2% and a reduced saturation fluence of $3.7\,\mu\mathrm{J/cm}^2$. Since the pulse energies in high-repetition rate cavities are typically small, this reduction of the saturation fluence, when combined with the increased modulation depth, provides favorable mode-locking conditions. Pump-probe measurements for delays of up to 50 ps show that the overall recovery time of the VA86 SBR was 9 ps, see Fig. 2-10.

The group delay dispersion of the SBR with the PRC at a wavelength of 1568 nm was measured as $\sim -1300\,\mathrm{fs}^2$, so that, together with the anomalous dispersive gain fiber, the cavity operated in a net anomalous dispersion regime $(\sim -5300\,\mathrm{fs}^2)$ to support soliton formation.

49
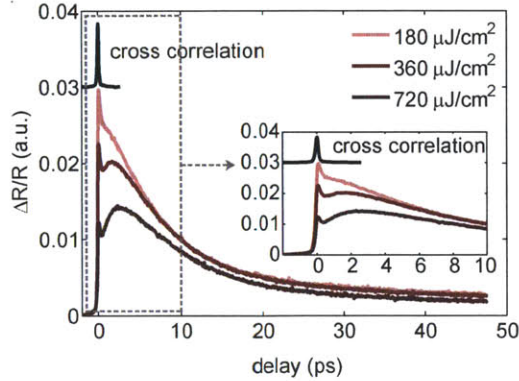
Figure 2-10: Recovery time of 9 ps for SBR VA86.

2.3 Fiber Laser Characterization

2.3.1 Optical Results

The mode-locked laser performance in terms of spectral bandwidth and achievable pulse duration was evaluated in the following: Fig. 2-11 depicts the measured optical spectrum (a) and interferometric autocorrelation (IAC) trace of the laser (b). The optical spectrum supported a 17.5-nm full-width at half-maximum (FWHM) optical bandwidth, thus implying a 150-fs transform-limited FWHM pulse duration. For the autocorrelation measurement, the laser output was amplified by an Er-doped fiber amplifier and the dispersion was compensated in fiber to adjust for the encountered dispersion in the measurement path. The autocorrelation measurement yielded a 187-fs FWHM pulse duration. The small deviation to the transform limited pulse duration could be attributed to a slightly imperfect dispersion compensation.

The optical spectrum was centered around 1573 nm, as determined by the wavelength-dependent reflectivity of the SBR and the gain spectrum at the operating power level. The output signal power was measured to be 27.4 mW, which corresponded to 283-pJ intracavity pulse energy. These values were obtained with 380 mW of pump power that was launched into the Er-fiber, of which an estimated value of 185 mW of power was absorbed in the EDF

core. Separate experiments showed that 30% of the launched pump power was absorbed in a single-pass through the gain fiber, and 90% of the remaining pump was reflected by the butt-coupled pump-reflective SBR. The GHz laser was self-starting; with increasing pump power, the laser first operated in a Q-switched mode-locked state and then transitioned to a soliton mode-locked regime at a pump power of 200 mW with a FWHM optical bandwidth of 9.0 nm. For launched pump powers higher than 382 mW, multiple pulsing occurred. Good signal stability in the RF spectrum is visible in Fig. 2-11(c) with a signal-to-background ratio of 80 dB for the fundamental repetition rate at 967.3 MHz.
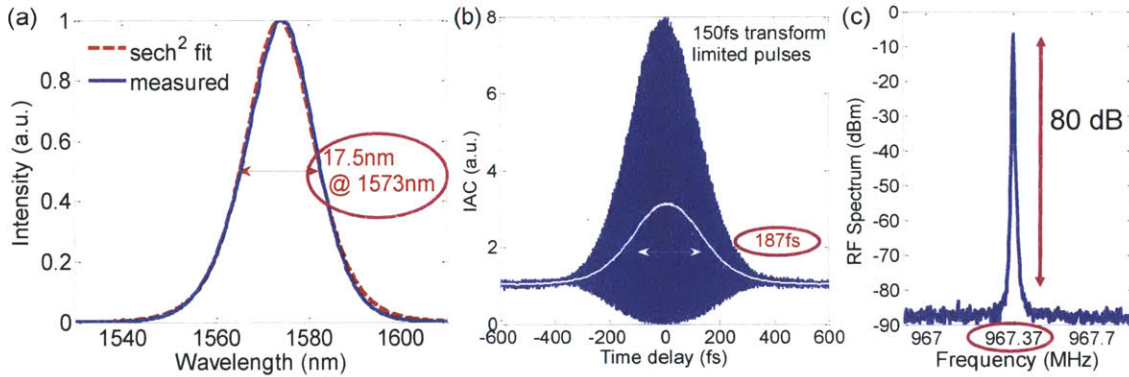
Figure 2-11: Results from the 1 GHz Erbium-doped fiber laser: (a) Optical spectrum with 17.5 nm 3-dB bandwidth with an output power of 27.4 mW. (b) IAC trace with 187 fs FWHM pulse duration. (c) Repetition rate of 967.3 MHz with an 80 dB signal-to-background ratio.

Several versions of the 1 GHz laser were built, and Fig. 2-12 shows the optical and RF characteristics for a laser with 93 mm of Er-doped fiber spliced to a 7-mm-long SMF piece. Depending on the fiber birefringence and butt-coupling, the mode-locked laser states were centered at different operating wavelengths in the C-band. The spectrum centered at 1571.1 nm featured a 16.6 nm, 3-dB bandwidth with an output power of 28.8 mW for a launched pump power of 335 mW (which corresponds to 515 mW coupled into the wavelength division multiplexer (WDM) at a 1100 mA pump current from an EM4-700mW pump diode). For comparable pump powers, pulses centered at shorter wavelengths of 1563.9 nm and 1556.8 nm were recorded with narrower FWHM bandwidths of 9.2 nm and 7.5 nm, re-

spectively, for 13.7 mW and 10.3 mW of output power. The corresponding transform-limited FWHM pulse durations vary between 160 fs and 340 fs. By reducing the SMF fiber piece, a repetition rate of 1.034 GHz was obtained, as shown in Fig. 2-12(b). Multiple lasers with comparable repetition rates between 1.034 to 1.045 GHz were fabricated for different applications. The reproducibility of the laser depended on the length tolerances during the fiber assembly, which determined the repetition rate (1 mm of fiber length corresponds to a change in repetition rate by 10 MHz).
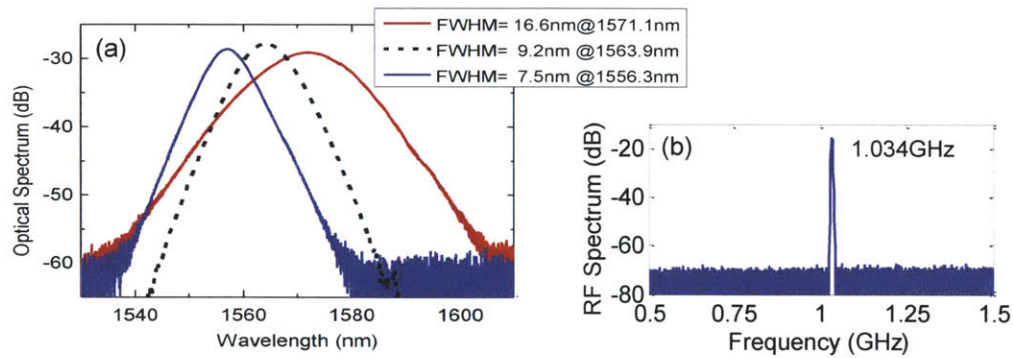
Figure 2-12: (a) Optical spectrum for three different mode-locked states, (b) 1.034 GHz repetition rate.

2.3.2 Long-Term Stability

In order to evaluate the stability of this laser, long-term power measurements were conducted. However, as initial fluctuations of the laser output were directly correlated to power fluctuations from the pump diode, an active feedback control of the output power was implemented in order to negate pump power fluctuations. Fig. 2-13 shows the output power in 2-13 (a), the temperature inside the fiber package in 2-13 (b), the optical spectrum FWHM in 2-13 (c), and the repetition rate drift in 2-13 (d) for 63 hours of continuous operation. For a launched pump power of 270 mW, the output power was measured by using a power meter with an analog output, which recorded data at a sampling rate of 1 sample per second through a data acquisition card (National Instrument PCI-6013). The optical spectral width and the repetition rate were transferred from the instruments (ANDO AQ6317
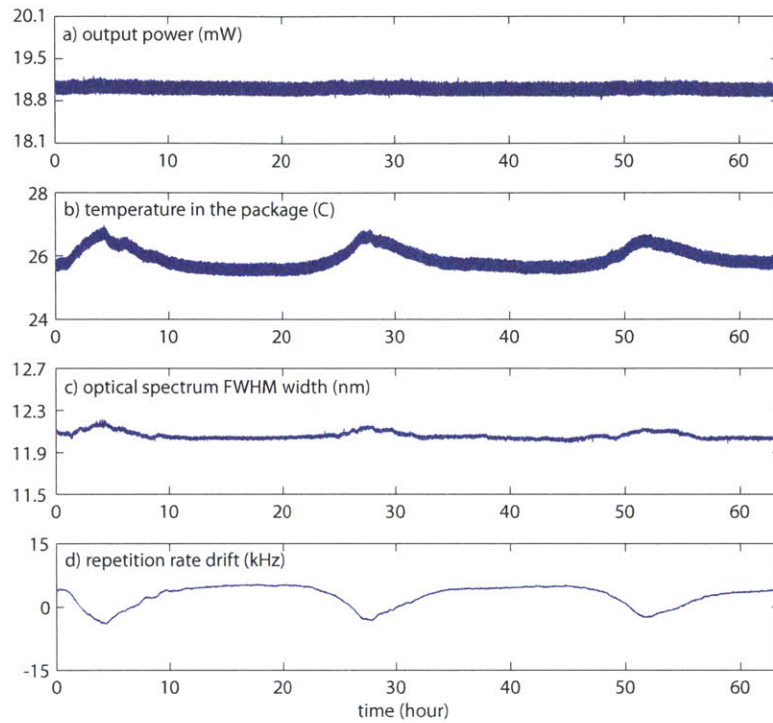
Figure 2-13: Long-term power measurements taken over the span of 63 hours confirmed stable mode-locked operation.(a) Fluctuations in the output power were below 0.5 %, while the environmental temperature (b) drifted by 1.5 °C. Drifts in (c) the optical spectrum and (d) repetition rate were induced by the temperature-dependent fiber birefringence.

and HP 8568B, respectively) through a GPIB interface every five seconds. For the active feedback, the analog output of the power meter was fed into the negative input of a loop filter box (New Focus LB1005) whose output modulated the current of the pump diode driver.

Fig. 2-13 (a) shows the output power over a period longer than two days with fluctuations of only 0.5%. The temperature in the laser package underwent deviations in the temperature cycle of 1.5 °C each day. Measurements started at 10 am and the temperature rose and fell during daytime, while the temperature remained constant overnight. The fairly constant optical spectral width and the repetition rate verified the good laser stability, since variations were induced by the ambient temperature change. Variations in temperature can alter the

birefringence of bent or twisted fibers [57], which affects the pulse energy (see Fig. 2 in [58]) and, as a consequence, the optical spectral width of the solitons. Thus, the temperature-related changes in the optical spectrum can be explained by the temperature-dependent fiber birefringence. Any of these temperature-dependent fluctuations could be suppressed further by actively stabilizing the temperature within the fiber package.

The repetition rate drift of -7 ppm°C in Fig. 2-13 (d), originated mostly from the temperature-dependent refractive index of the fiber. For higher temperatures, the optical path length of the laser cavity increased, and it reduced the repetition rate accordingly. The corresponding change of the optical path length of + 7 ppm °C, agreed well with the measured thermo-optic coefficient dn/dT of + 8.5 ppm °C for fused silica fiber (Table 6 in [59]).

2.3.3 Polarization Rotation in Laser Output

In the previous section, the impact of fiber birefringence on the pulse energy and on the optical spectrum of a mode-locked laser was outlined. In addition, fiber birefringence affects the polarization state, since every single-mode fiber can support two orthogonal polarization modes. In a perfectly circular fiber, the two polarization modes are degenerate and they propagate with identical phase velocities. However, in general, fibers have a slightly elliptical cross-section so that residual stress generates linear birefringence, thereby allowing different polarization components to interact with each other through nonlinear polarization coupling [58]. Therefore, in a laser cavity without any polarizing elements, both polarization eigenmodes can oscillate simultaneously, thus resulting in so-called vector solitons.

Depending on the cavity parameters, including the fiber birefringence, the laser output polarization can evolve periodically or the two polarization components can be locked to emit stable, elliptically polarized solitons, called polarization-locked vector solitons (PLVS's) [60, 61]. PLVS are locked in phase and group velocity, whereas in the case of an evolving output polarization, the two polarizations within the laser cavity are coupled through cross-phase modulation to propagate as one unit. Visible sidebands in the RF spectrum, once a polarization discriminative element was incorporated in the external beam path, can thus be

54
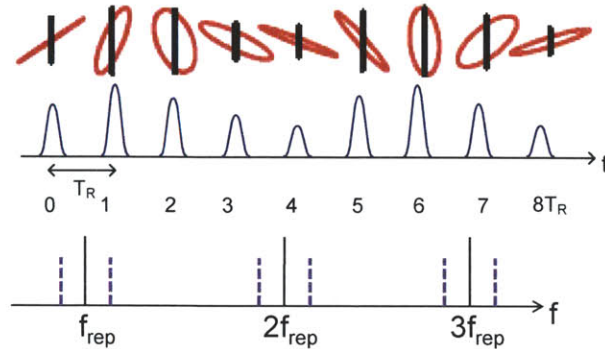
Figure 2-14: Schematic of polarization rotation that was converted into an amplitude modulation of the output pulse train. The polarization evolution (with a periodicity of $8\,T_R$ here) gave rise to frequency sidebands. The first part of this figure was adapted from [60].

explained by a modulation at a polarization evolution frequency (PEF). This is illustrated in Fig. 2-14, where the polarization evolution frequency is equal to eight times the initial round-trip time, $8 \cdot T_R$. In a polarization sensitive set-up (where the fiber laser output was collimated onto a polarization beam splitter and focused with an aspheric lens onto a free-space detector), the polarization rotation was translated into an amplitude modulation. However, this polarization rotation could be eliminated by carefully aligning the fiber so that the laser operated in the PLVS regime [60].

To support PLVS, the fiber was bent and twisted manually until an optimized polarization state was achieved. Bends in the fiber introduced an additional retardation that changed the orientation of an elliptical polarization state, whereas fiber twists rotated any linear polarization (see [57]). However, due to the short fiber cavity, bending and twisting of the fiber introduced additional changes to the butt-coupling contact at both fiber ends.

Therefore, in order to make this procedure more reliable, a commercially available polarization control unit was miniaturized and its length reduced from 76.2 mm to 56 mm, as shown in Fig. 2-15. Although this required some modification of the ferrules to connectorize the fiber ends, the 1 GHz butt-coupled lasers could be accommodated in the modified unit, see Fig. 2-15. By rotating and squeezing the fiber, the number and position of the polarization side-bands visible in the RF domain could be suppressed.
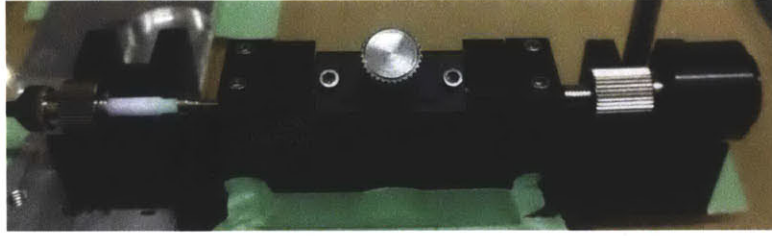
Figure 2-15: Machined polarization control unit (56 mm length) for 1 GHz fiber laser.
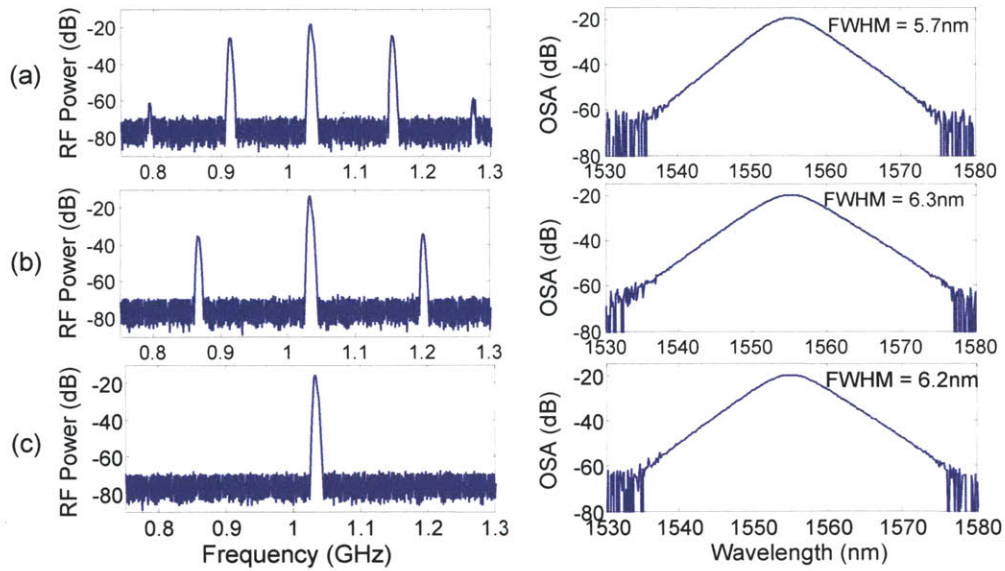
Figure 2-16: Output of 1 GHz EDFL with polarization control unit. For (a) and (b) adjustments to the applied pressure on the fiber were made. The combination of squeezing and rotating the fiber led to polarization-locked vector solitons in (c).

For Figs. 2-16 (a) and (b), each mode-locked laser state was induced by applying additional pressure on the fiber with the adjustment screw. The recorded signal corresponded to the TE polarization, which was recorded on a photodetector for the RF measurements. The output power increased from 12.7 mW in state (a) to 13.2 mW in (b), thus resulting in a slightly wider optical spectral bandwidth from 5.7 nm to 6.3 nm. By adjusting the fiber birefringence in order to move the side-bands closer to the repetition rate line, the side-bands generally collapsed and disappeared as PLVS were generated. With the polarization unit, the combination of introducing a rotational twist and squeezing of the fiber produced

polarization-locked pulses, as shown in Fig. 2-16 (c), with an output power of 13.2 mW and an optical FWHM bandwidth of 6.2 nm. (For these studies, the laser was pumped only with moderate pump powers, thus explaining the narrower FWHM spectral bandwidths of ~6 nm.) The polarization remained stable over hours in the device. The polarization unit reduced the alignment time and a polarization locked output was found in a more controlled fashion that could be easily maintained. However, the degree of freedom from changing the butt-coupling, which enabled tuning of the EDFL center wavelength, was lost due to the residual strain and tight confinement within the polarizer unit.

2.3.4 Thermal Management of the SBR

Particularly for high-repetition rate lasers, good thermal management of the SBR was essential to achieving long-term stable laser sources. During the optimization process of the 1 GHz laser, SBR damage was encountered on different occasions. At times, damage occurred instantaneously before the laser was mode-locked or at high pump-powers, when the laser would fall out of mode-locking. In addition, thermal damage introduced by long-term excessive heat was observed when butt-coupling the gain fiber directly to the SBR, or in configurations without proper heat sinking of the absorber end.

Experiments with a dichroic mirror (which filtered out the 980 nm pump light) in a comparable laser set-up, demonstrated that the pump power significantly contributed to SBR damage. Induced thermal heating from the pump light (for 380 mW of launched pump power, a residual pump power of ~266 mW impinged upon the SBR for the 1 GHz EDFL), in combination with femtosecond pulses at 1550 nm, resulted in a reduced damage threshold. Therefore, the design of a pump-reflective coating was a key aspect in addressing the thermal damage challenge. However, even with this additional dielectric coating, damage was still observed for specific cavity configurations.

Thus, to study the SBR-related thermal damage in more detail, four different fiber cavity set-ups were evaluated, as shown in Fig. 2-17. The EDF and the SBR were in direct contact with each other in configurations (a) and (b), while single-mode passive fiber (SMF-28e) was

spliced to the EDF in configurations (c) and (d). The thickness of the GaAs substrate of the SBR in configurations (a) and (c) amounted to 350 μm (the standard wafer thickness), while the substrate was lapped down to a final thickness of 150 μm in configurations (b) and (d) in order to improve heat sinking of the absorber layer. In all configurations, the total cavity length ranged from 100 mm to 105 mm, with a 6-mm long SMF section incorporated only for configurations (c) and (d). Most of mode-locking results described in this chapter were obtained in a configuration similar to Fig. 2-17 (c), with a slightly longer length for the SMF section.
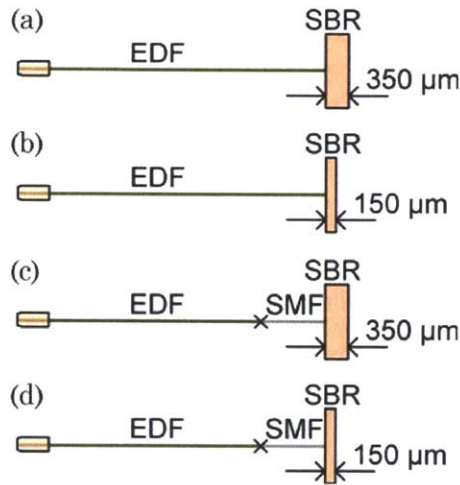
Figure 2-17: Four different EDFL configurations were analyzed in order to minimize thermal damage to the SBR.

Configuration (a) was tested first. For a launched pump power of 180 mW, soliton pulses were generated with an optical spectrum FWHM width of 5.4 nm and an average output power of 5.0 mW at a repetition rate of 975 MHz. However, after tens of seconds, the output power dropped to a few nW, with permanent damage observed on the SBR and fiber ferrule. The hot fiber core most likely caused local deformations of the pump-reflective coating due to different thermal expansion coefficients between the dielectric coating and the underlying III-V compound semiconductor-based SBR. After deformation of the coating, the pump light might no longer have been fully reflected (observed as decreased fluorescence from the

gain fiber before the intracavity losses became too high), which subsequently resulted in additional damage to the SBR by heat that was generated by absorption of the pump light.

Therefore, to prevent thermal damage, two critical protective mechanisms were implemented: (I) the SBR substrate was thinned down, and (II) passive single-mode fiber was inserted between the EDF and the SBR. The GaAs substrate of the SBR was lapped down from $350\,\mu$m to a final thickness of $150\,\mu$m for improved heat sinking of the saturable absorber. With a thermal conductivity of $55\,$W/(K m) [62], the thinner GaAs substrate reduced the overall thermal load by $3.6\,\mu$K/W. Closer proximity to the copper heat sink with a thermal conductivity of $401\,$W/(K m) [63] constituted an improvement by a factor of ten, since a copper layer of comparable thickness only had a thermal resistance of $0.5\,\mu$K/W. The SMF fiber piece reduced the heat transfer from the EDF core to the SBR, and the thinned-down substrate facilitated the heat transfer from the surface of the SBR to the copper mount. As a result of both protective mechanisms, the laser demonstrated stable generation of soliton-like pulses (see Fig. 2-13 and Fig. 2-18) for a time period exceeding three weeks.
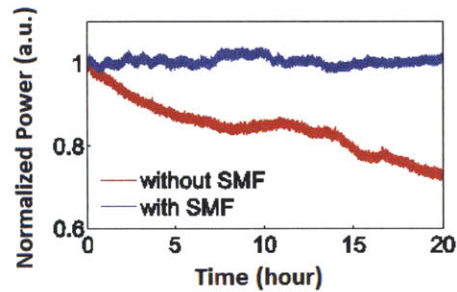
Figure 2-18: Recorded power for 1 GHz laser with and without SMF spliced to the gain fiber. The output power for the laser without the SMF buffer slowly decreases to 70 % of the initial value.

At the same time, a comparison of configurations in Figs. 2-17 (b) and (c) indicated that incorporating the SMF section had more impact than thinning the substrate of the SBR to prevent thermal damage. When the output power from EDFLs with and without SMF was recorded, the output power dropped to 70% of the initial output power over a span of

20 hours for the fiber configuration without SMF, as shown in Fig. 2-18. The SMF-buffered cavity maintained a constant output power with fluctuations of only a few percentage points, which could be attributed to pump power fluctuations.

2.3.4.1 Temperature Evaluation in Gain Fiber

Spatial separation of the hot gain fiber core from the saturable absorber proved an effective means to avoid thermal damage of the SBR. Thus, efforts were made to estimate the gain fiber temperature. Because the core temperature in the fiber could not be easily determined experimentally, this parameter was evaluated by following an approach similar to Li *et al.* [64]. In order to transfer their evaluations for a gain fiber with a core diameter of $20\,\mu$m to the 1 GHz EDFL ($\sim 8\,\mu$m core diameter), Li's calculated values were prorated. By assuming that 185 mW of pump light was absorbed out of 380 mW of launched pump power, an equivalent absorbed pump power was derived. For a pump that was absorbed uniformly over the smaller core, the equivalent absorbed pump power for the $8\,\mu$m core diameter corresponded to $185\,\text{mW} \cdot (20\,\mu\text{m}\,/\,8\,\mu\text{m})^2 = 1.16\,\text{W}$. The total equivalent launched pump power was approximately two times the absorbed pump power, or 2.32 W, which raised the temperature of the core by at least 55 °C above the ambient temperature (this was deduced from Fig. 3 in [64]). In this calculation, the same absorbed pump power per unit area was assumed to induce the same temperature increase of the core fiber. However, the core temperature should be treated as a lower limit estimate, since Li *et al.* actively cooled their Er/Yb gain fiber, whereas, in this system, only passive air convection to the environment provided heat transfer.

Therefore, heat diffusion equations (similar to an analysis conducted in [65], [66] and [67]) were evaluated in order to obtain an analytical approximation for the thermal distribution in steady-state in the fiber. The following two equations for a fiber core radius of r_{core} and cladding radius of $r_{cladding}$ describe any radially symmetric fiber with radius r:

60

$$\frac{1}{r} \cdot \frac{\partial}{\partial r} \cdot \left(r \cdot \frac{\partial T_1(r,z)}{\partial r} \right) + \frac{\partial^2 T_1(r,z)}{\partial z^2} = -\frac{Q_0}{k} \qquad 0 \leq r \leq r_{core} \qquad (2.1)$$

$$\frac{1}{r} \cdot \frac{\partial}{\partial r} \cdot \left(r \cdot \frac{\partial T_2(r,z)}{\partial r} \right) + \frac{\partial^2 T_2(r,z)}{\partial z^2} = 0 \qquad r_{core} \leq r \leq r_{cladding} \qquad (2.2)$$

In the presented fiber laser systems, which consisted of short gain fiber sections, the pump power absorption was assumed to be uniform. Thus, the heat distribution did not vary along the longitudinal cavity dimension z so that the second derivative terms could be neglected in Eq. 2.1 and Eq. 2.2, thus simplifying the temperature distribution $T(r,z)$ to a radially symmetric profile $T(r)$. The thermal conductivity k of SiO_2 was assumed at $k = 1.38 \cdot 10^{-2} \frac{W}{cmK}$ (compare [65]). The heat density Q_0 was calculated based on an absorbed pump power of 183 mW over a 9.2 cm length in the 1 GHz EDFL with a quantum-limited heat absorption of $1 - \frac{\lambda_{pump}}{\lambda} = 0.37$ for the core area. By using boundary conditions for a continuous temperature profile and its derivative, the following equations can be derived:

$$T_1(r) = T_c + \frac{Q_0 \, r_{core}^2}{4k} \cdot \left[2 \ln\left(\frac{r_{cladding}}{r_{core}} \right) + \frac{2k}{r_{cladding} \, h} \right] + \frac{Q_0 \, r_{core}^2}{4k} \cdot \left[1 - \left(\frac{r}{r_{core}} \right)^2 \right]$$

$$0 \leq r \leq r_{core} \qquad (2.3)$$

$$T_2(r) = T_c + \frac{Q_0 \, r_{core}^2}{2 \, r_{cladding} \, h} - \frac{Q_0 \, r_{core}^2}{2k} \cdot \ln\left(\frac{r}{r_{cladding}} \right) \qquad r_{core} \leq r \leq r_{cladding} \qquad (2.4)$$

Here, a convective heat flow in air at the outer radius (heat transfer coefficient of air of $h = 1 \cdot 10^{-3} \frac{W}{cm^2 K}$) was assumed, and T_c describes the temperature of the air coolant. Eq. 2.3 indicates that the temperature in the gain fiber can reach 121.8° C. Depending on the pump power launched into the gain fiber, the temperature can vary between 77.3° C (for the mode-locking threshold of 200 mW launched pump power and an assumed absorbed power of 100 mW) and 121.8° C.

2.3.4.2 Optical Microscopy of SBR Damage

Slow degradation of the optical performance usually indicated the onset of damage to the SBR. In this context, we refer to permanent changes to the SBR surface structure that are visible under an optical microscope and that impaired the optical laser operation.

The above-mentioned mechanisms to protect the SBR from the pump light and to reduce its thermal exposure, effectively mitigated thermal damage effects to the SBR. Thus, continuous long-term stable operation was recorded over months. However, in some other instances, damage to the SBR was still recorded and studied further.

Fig. 2-19 depicts the microscope image of a polished fiber ferrule connector that was butt-coupled to the SBR. The ferrule itself featured a 3.4 mm diameter, with a 125 μm cladding diameter and a $\sim$9 μm diameter core. In Fig. 2-19, the core area exhibited permanent surface damage, which was visible as deposition specks on the otherwise smooth and polished fiber tip surface. At the onset of damage, deposition specks resembling small droplets first formed on the fiber ferrule surface. Usually, these drops had low surface adhesion and could be removed by mechanically cleaning the fiber ferrule. However, with time, any depositions tended to extend across the core area of the ferrule surface, as visible in Fig. 2-19, but they remained limited to the core and its proximity. While damage to the fiber connector end could be removed by mechanical polishing, damage to the SBR was irreversible, as shown in Figs. 2-20 (a) through (c).
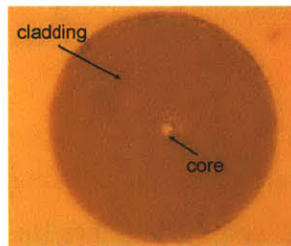
Figure 2-19: Optical microscope image of damage in the core region of a fiber connector.

Fig. 2-20 (a) shows damage spots on the SBR VA86 PRC where the fiber core came in direct contact with the SBR. This damage resulted from a butt-coupled 1 GHz EDFL
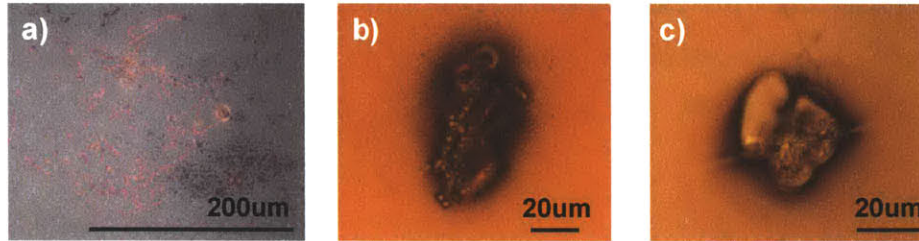
Figure 2-20: Microscope images of SBR damage: (a) SBR VA86 with PRC under 50x magnification, (b) magnification of damage on SBR VA86 PRC, and (c) damage on proton-bombarded SBR VA86 from external 625 MHz fiber laser.

whose mode-locking state was continuously modified, and Fig. 2-20 (a) demonstrates one of the worst case scenarios. During the alignment process, the fiber was slightly bent and the SBR end rotated in order to optimize the mode-locking state. Thus, damage extended over a small, localized area. The damage resembles mechanically abrasive spots on the surface possibly combined with thermal damage to the SBR layers.

Figs. 2-20 (b) and (c) show other examples of inflicted SBR damage. Fig. 2-20 (b) shows two defined ring structures towards the top of the damaged spot, whose dimensions directly correlate with the fiber core diameter of a butt-coupled EDFL. In the center of the image, individual damage combined into more elongated structures, where the fiber position was slightly varied. Thermal damage on SBR VA86 without any pump-reflective coating from an external fiber cavity (cf. Section 3.3) is illustrated in Fig. 2-20 (c). Here, the focus spot on the SBR was moved in order to obtain the best mode-locking state. Excessive pump light leakage at 980 nm onto the SBR was assumed to have contributed to the visible damage and heating of the layers, leading to small surface cracks.

The exact origin of these damage spots is currently being studied further. As the pump-reflective-coated SBRs were used for long-term operation (several months) in the butt-coupled EDFL lasers without performance degradation, extensive damage does not seem to have been caused during steady-state mode-locked operation. However, before stable cw mode-locking is achieved, the laser, in general, goes through a transitionary Q-switching state, during which intensity fluctuations significantly higher than the steady-state mode-

locking intensities can arise. Therefore, damage is likely to occur when these intensity spikes induce rapid temperature changes which can lead to the observed material deformation or buckling of the surface layers.

In addition, preliminary experiments implied that the extent of damage depended on the total absorber layer thickness, as a double-absorber SBR VA148 (see Chapter 5) was more prone to damage while under the comparable mode-locking conditions, the above-mentioned single-absorber VA86 provided a stable output pulse train. Since the SBRs were designed for a maximum overlap of the electric field with the absorber, effects in the GaAs cladding might contribute as secondary effects. Though studies performed on thin quantum-well absorber devices with low modulation depths (smaller than 1%) at multiple mJ/cm^2 fluence levels [68] indicate that inverse saturable absorption effects based on two-photon absorption in the GaAs layers set the damage threshold for SBRs. These findings might not necessarily be transferable to the presented laser systems that operated at reduced $\mu J/cm^2$ fluences. As damage was recorded in an intracavity laser (as compared to an external steady-state femtosecond pulsed source in [68]), transient influences were not considered in the performed study. Therefore systematic studies of determining damage thresholds with a comparable femtosecond laser source for SBRs outside the laser cavity could reveal further insight.

2.3.5 Alternative Butt-Coupling Mechanism

To improve the current butt-coupling mechanism, but continue to offer the capability of exchanging SBRs, a SBR was mounted on the surface of a fiber ferrule. This fiber ferrule with the SBR on top was then butt-coupled in a mating sleeve against the EDFL connector. Such a mounting mechanism offered the advantage that any rotating motion between the SBR and fiber ferrule could be avoided (compare current butt-coupling in Fig. 2-4). For this purpose, small pieces of the SBR sample were cleaved. When the SBR was directly mounted on top of a regular fiber zirconia ferrule with a 2 mm diameter, as seen in Fig. 2-21 (a), thermal damage to the SBR was noted since no heat-sinking mechanism was implemented.

In order to improve the thermal heat transfer, Cu rods of the same diameter as fiber ferrules was machined (with support from Jonathan Morse). Figs. 2-21 (b) and (c) show the SBR that was secured with silver paste on top of the Cu rod. The fiber assembly is illustrated in Fig. 2-21 (d), with the EDFL connector butt-coupled against the SBR on the Cu rod in a brass mating sleeve. (The plastic connector cap merely served to handle the Cu rod more easily.) With this mounting mechanism, stable mode-locked operation for the presented Erbium-doped fiber lasers was achieved for optical spectra centered at ~ 1560 nm. The mode-locked state could be readily reproduced, since slight angle deviations were not permitted in this butt-coupling approach, contrary to the lens tube mounting mechanism. In addition, coupling between fiber connectors in a mating sleeve was reliably used as an optimized configuration between the EDFL fiber ferrule and the OC. It offered the advantage that visual feedback on the position on the SBR was obtained through the slit in the mating sleeve. Therefore, this approach provided a good alternative butt-coupling mechanism.
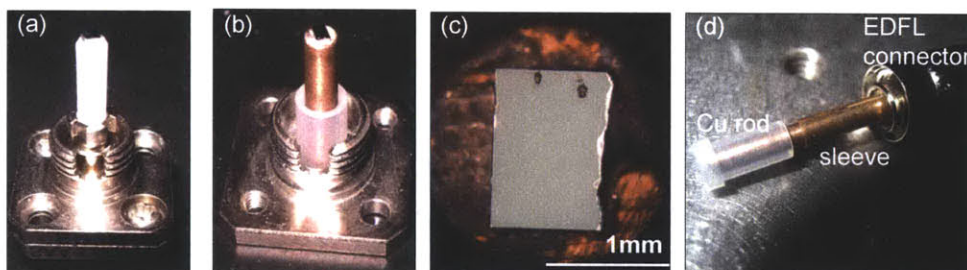
Figure 2-21: (a) SBR mounted on a commercially available zirconia ferrule. (b) SBR mounted on a custom-machined Cu rod. (c) Magnification of SBR secured with silver glue on the top surface of the Cu rod. (d) Assembly of the EDFL connector which is butted against the SBR on top of the Cu rod in a mating sleeve.

2.3.6 Phase Noise

Phase noise is defined as the single-sided spectral density of the temporal phase fluctuations of a desired signal. Rapid, random fluctuations, due to instabilities, lead to a distribution around the desired frequency line so that power is spread to adjacent noise side-bands. This can be captured in the frequency domain by a power spectral density measurement relative

to the signal frequency.

In general, two major noise sources contribute to the phase noise spectrum: Basic quantum mechanical noise from amplified spontaneous emission (ASE) induces amplitude and phase fluctuations. This ASE noise is statistically independent and leads to a random walk of the pulse position each round-trip, proportional to $1/f^2$ [69]. As a second mechanism, the center frequency of the pulse undergoes fluctuations which couple indirectly through dispersion into phase-noise. Thus, the phase noise density spectrum $S_{2\phi}$ (which is the two-sided noise spectrum) can be expressed as (compare [69]):

$$S_{2\phi} \approx 0.53 \frac{\theta \, h \, f}{E} \frac{l_{cav}}{T_{RT}} \frac{\tau_p^2}{(2\pi f)^2} + 0.53 \left(\frac{D}{f \, T_{RT}}\right)^2 \frac{1}{(2\pi f)^2 + \tau_\nu^{-2}} \frac{\theta \, h \, f}{E} \frac{l_{cav}}{T_{RT}} \Delta f \quad (2.5)$$

In Eq. 2.5 the phase noise is proportional to the photon energy $h \, f$, the total intracavity losses l_{cav} and to the square of the pulse duration τ_p. Longer pulses are more susceptible to quantum noise changes over a wider temporal window, which can lead to larger shifts of the weighted center of the pulse. The direct phase noise contribution is inversely dependent on the pulse energy E and round-trip time T_{RT}, since with longer cavity lengths the impact of gain and loss noise acts less frequently on the propagating pulse. θ describes a spontaneous emission factor, Δf the spectral pulse bandwidth and τ_ν describes the filter time constant from gain filtering or other bandwidth limiting devices.

Once the phase noise has been determined, the RMS integrated timing jitter τ can be deduced from the single side-band phase noise density spectrum S_ϕ through Eq. 2.6 for a frequency interval $[f_1, f_2]$.

$$\tau = \frac{1}{2\pi \cdot f_{rep}} \cdot \sqrt{2 \cdot \int_{f_1}^{f_2} S_\phi \, df} \quad (2.6)$$

Fig. 2-22 (a) shows the single side-band (SSB) phase noise for the first harmonic of the 967.3 MHz EDFL. The laser output power was focused on a photodetector (EOTech ET-3500), filtered by a bandpass filter, and amplified to +16 dBm before being measured with a signal source analyzer (Agilent E5052). The timing jitter integrated from 10 MHz

progressively down to 1 kHz is shown as the red dotted line in Fig. 2-22 (a), which indicates an integrated jitter of 22 fs over the entire interval. The phase noise below 10 kHz follows a slope of -20 dBc/decade and can be suppressed by controlling the fiber length with a piezo-based stretcher and locking the repetition rate to an electronic oscillator with better long-term stability. The bandwidth limitations of this approach will likely limit the suppression of the phase noise to frequencies below 10 kHz. Phase-noise contributions at low frequencies can also be attributed to RF amplifiers.
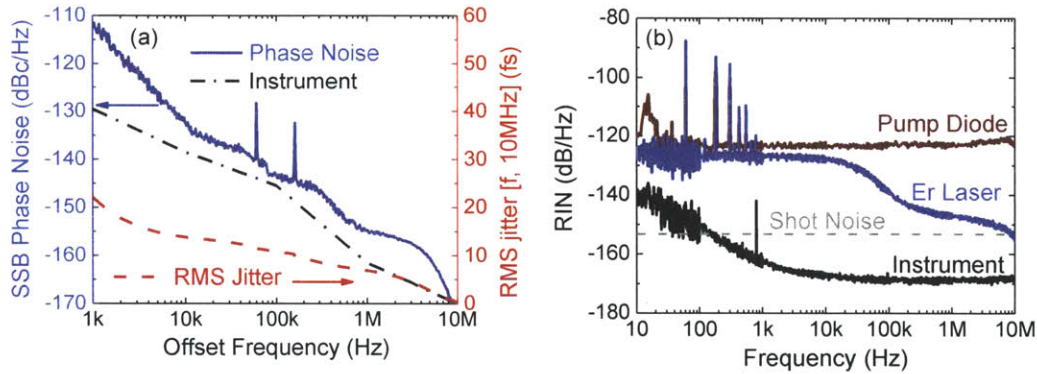
Figure 2-22: (a) Single side-band phase noise and timing jitter (dashed line) and (b) relative intensity noise.

The relative intensity noise (RIN) of the 967 MHz EDFL, see Fig. 2-22 (b), was measured to demonstrate the stability of the output intensity. The laser output was converted to an electrical signal by an amplified InGaAs photodetector (Thorlabs PDA400) with a trans-impedance gain of 7500 V/A. The split output power level of 0.53 mW was generated with a voltage of 3.54 V at the detector output with a 50 Ω termination. The corresponding RIN of the shot noise level, -153 dBc/Hz, exceeded the noise floor of the vector signal analyzer (HP 89410A) so that the measured noise was mainly determined by the laser output noise and not limited by the vector signal analyzer. The integrated relative intensity noise of 0.014 % from 10 Hz to 10 MHz mostly originated from the pump diode noise that is shown as the dark red curve in Fig. 2-22 (b). The RIN of the laser was lower than that of the pump diode because the slope efficiency was reduced at the operation point due to gain saturation. A

rapid drop of the laser RIN above 1 kHz is attributed to the long upper state lifetime of Er-ions. Both RINs, of the pump diode and the laser, show downward slopes near 7-8 MHz, which was consistent with the 3-dB detector bandwidth of 10 MHz.

The 967 MHz EDFL featured an optical spectrum that was centered at 1570 nm with a spectral bandwidth around 16 nm. This phase noise measurement was compared with a 1.044 GHz EDFL, which was centered at 1560 nm with a 3-dB optical bandwidth around 10 nm and 10 mW of output power.

Fig. 2-23 (a) shows the phase-noise and integrated timing jitter for two different mode-locked laser states of the free-running 1 GHz EDFL, as recorded for the fundamental repetition rate with the signal source analyzer. A constant offset in the phase noise is clearly visible. As different RF amplifiers were used in both measurements, the 1.044 GHz measurement was likely limited by the amplifier noise for the whole measurement spectrum. For an integration range of 1 kHz to 10 MHz, the integrated RMS timing jitter depended highly on the mode-locked state, varying between 22 fs for the 967.4 MHz EDFL and 72 fs for the 1.044 GHz EDFL. Thus, a more detailed study of how the different mode-locked states affect the timing jitter is being performed and the influence of different RF amplifiers tested.

In addition, the phase noise measurements of the 967 MHz EDFL and a 509 MHz EDFL (consisting of purely Liekki Er-80 8/125 gain fiber) were compared. The 509 MHz laser, in general, mode-locked at a center wavelength at 1565 nm with a 3-dB bandwidth around 8 nm. In this instance, the slope of both measurements matched, however, the high frequency noise performance for 500 kHz and higher was characterized by saturation effects for the 509 MHz EDFL. Different filter bandwidths could account for the different slopes at high offset frequencies. As for the 1.044 GHz EDFL measurement, the highest offset frequencies dominate the timing jitter, which for the 509 MHz laser amounted to 55 fs for the interval of 1 kHz to 10 MHz.

In general, low phase-noise can best be measured in the optical domain. Thus, a balanced optical cross-correlation for each laser system which can resolve attosecond timing-jitter can therefore reveal the limitations of this measurement and determine the actual timing jitter.
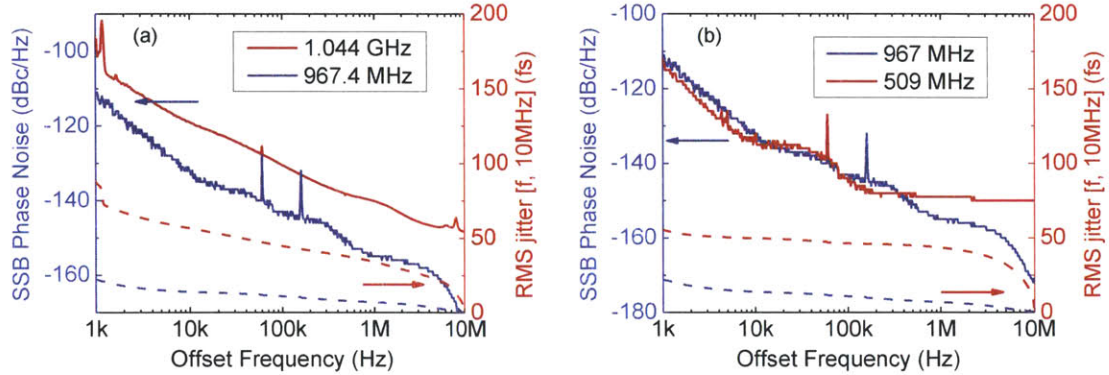
Figure 2-23: Comparison of single-side band phase noise and timing jitter: (a) for different 1 GHz EDFL mode-locked states and (b) for 1 GHz EDFL and 500 MHz EDFL.

2.3.7   Repetition Rate Locked System

In the previous section, the noise performance for offset frequencies from 1 kHz to 10 MHz was studied. As repetition rate fluctuations significantly impacted the phase noise below frequencies of 1 kHz, stabilization of the repetition rate was pursued in collaboration with David Chao and results are described in this section.

Different mechanisms exist for stabilizing the laser repetition rate f_{rep}. In a direct detection scheme, one filtered RF line can be locked to an independent microwave oscillator so that the error signal provides feedback to an actuator within the laser cavity. Common methods include displacing one of the cavity end mirrors through piezo-transducers or motorized stages to adjust the cavity length or utilizing piezo-controlled fiber stretchers. The preferred implementation depends on the cavity configuration and desired locking bandwidth, since fiber stretchers usually exhibit smaller bandwidths.

For the 1 GHz EDFL, a compact actuator scheme had to be implemented as after connectorizing the EDFL only ~ 56 mm of the gain fiber remained accessible. Mounting the EDFL in a fiber stretcher introduced significant strain on the fiber so that during operation, the optical fiber snapped. As an alternative, adjusting the butt-coupling between the SBR and the end facet of the EDFL cavity with a piezo-controller was explored, as illustrated in Fig. 2-24 (a). A special mounting configuration, as shown in Fig. 2-24 (b), was assembled
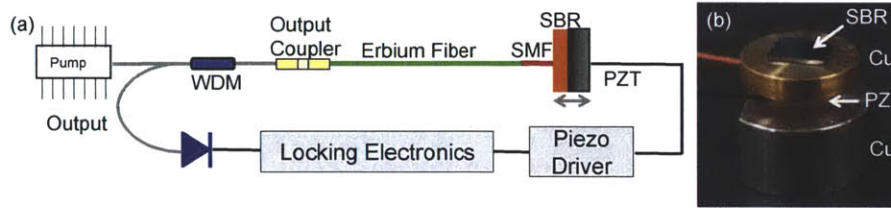
Figure 2-24: (a) Schematic of repetition rate locked EDFL system with a piezo transducer (PZT). (b) Photograph of the mounted SBR VA86 PRC on a Cu-heat sink on top of the piezo transducer which was secured to a Cu block.

to be compatible with a longer lens-tube set-up for butt-coupling. Any movement of the bottom Cu block in the lens tube was restricted by a retaining ring, without limiting the displacement range of the PZT. A reduced diameter Cu plate provided the critical heat sinking for the SBR. A 1 mm thin Cu disc was chosen so as to not significantly increase the load for the piezo-transducer and to not reduce the overall locking bandwidth. Moreover, the mounting procedure of the individual components complied with the damage thresholds of the individual parts. Thus, a combination of Indium soldering, Crystalbond 509 and silver paste was used to secure the individual components, depending on whether a permanent or reversible attachment was considered advantageous.

However, given the high sensitivity of the EDFL to butt-coupling changes, this approach could potentially change the mode-locked states and introduce polarization side-bands with any piezo-electric induced displacements of the SBR. Thus, the feasibility of this approach was tested by determining the range of the piezo-electric transducer for which mode-locking of the EDFL could be supported. The piezo-controller voltage was manually adjusted to induce displacements to the linear cavity of up to $\sim 0.42\,\mu$m in air, which translated to repetition rate changes of ~ 3 kHz. For increasing repetition rates, the center wavelength of the optical spectrum shifted by ~ 0.25 nm to shorter wavelengths, while the 3-dB bandwidth was reduced by up to $\sim 4\%$. For larger length offsets to the cavity, the laser no longer mode-locked. However, as repetition rate changes were observed to be ~ 0.1 kHz over several minutes, which corresponded to ~ 15 nm of cavity length changes for the linear laser, these fluctuations could be adjusted with the available transducer movement range.
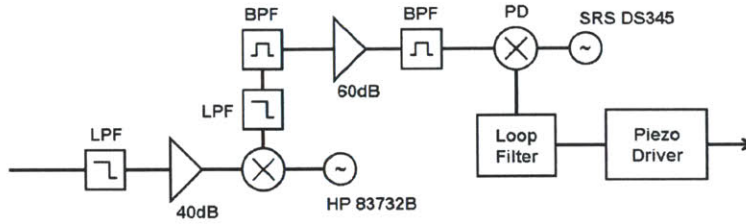
Figure 2-25: Schematic of the locking electronics for the repetition rate lock. Courtesy of David Chao.

The schematic of the repetition rate locking set-up is shown in Fig. 2-25. The fiber laser output power was split in half and detected with a fast photodetector to generate a RF signal train. The fundamental 1 GHz repetition rate was low-pass filtered, RF amplified by 40 dBm and mixed with the output of a signal source generator (HP 83732B) to 10.7 MHz. This RF signal was low- and band-pass filtered, amplified by 60 dB and band-pass filtered in a second stage to improve the spectral purity. The signal was then compared in a phase-detector with a microwave oscillator (SRS DS345) at 10.7 MHz whose error signal provided the input to a servo lock box (Precision Photonics LB 1005). The coarser discretization of the digital mixer (range of $\pm 32 \pi$) limited the lock to a residual phase noise around 0.1 rad (corresponding to 3 mV voltage in the locked state), as shown for the in-loop error signal in Fig. 2-26. An analog phase-detector significantly enhanced the lock as the residual phase noise could be reduced to 1.4 mrad (lock box settings for internal PI-controller of 7.1 for gain and 1 kHz corner frequency).

To evaluate the impact of the repetition rate lock on the noise properties, the single sideband phase noise density was measured. The detected laser output (with an InGaAs pin photodetector EOTech 3500F) was amplified and bandpass filtered to the fundamental repetition rate, before the signal was measured with the signal source analyzer (Agilent 5052A). The best phase noise spectrum was recorded for input signal values close to the maximum input power of +23 dBm. The comparison of the SSB phase noise for the free-running (unlocked) and repetition-rate-locked EDFL is displayed in Fig. 2-27. The low-frequency phase noise was significantly reduced for the locked system within the locking bandwidth
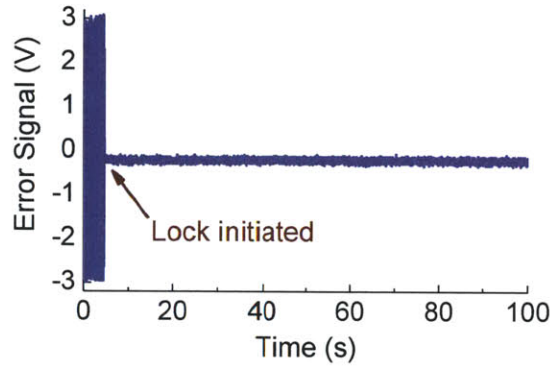
Figure 2-26: In-loop error signal out of the digital phase detector, recorded on an oscilloscope. Once the lock is initiated, the error signal collapses to 3 mV RMS amplitude.

(deduced from this trace) of $\sim 1\,\mathrm{kHz}$. As the low frequencies significantly contributed to the RMS integrated timing jitter, the free-running system featured a timing jitter of 4.8 ps for a 10 Hz to 10 MHz integration range, which was significantly reduced for the locked EDFL with a timing jitter of 215 fs over the same interval.
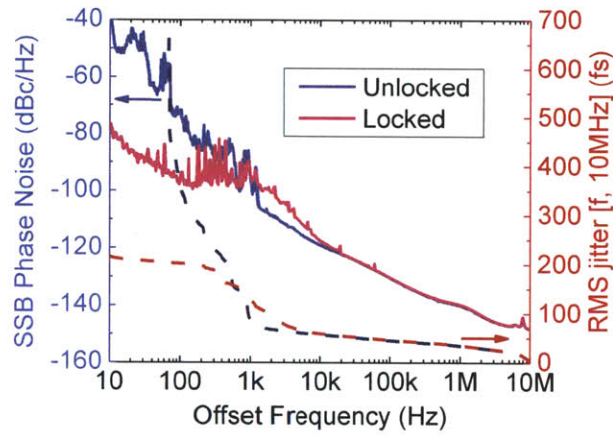
Figure 2-27: Phase noise (solid lines) and timing jitter (dashed lines) for repetition-rate-locked EDFL and free-running EDFL.

2.4 Additional Fiber Laser Designs

2.4.1 2 GHz Harmonically Mode-Locked Laser

While the repetition rate f_{rep} in a fundamentally mode-locked laser cavity is determined by the cavity length, harmonically mode-locked lasers operate at harmonics of the fundamental repetition rate. Thus, in a harmonically mode-locked laser (HMLL) multiple pulses circulate in the laser cavity, as illustrated in Fig. 2-28, resulting in more complex pulse dynamics.

Intracavity amplitude modulation or interferometric filtering can induce HMLL by forcing the pulses into constant temporal spacings. However, under special conditions, self-organization of the pulses at harmonics of the repetition rate can take place, as observed in passive soliton fiber laser systems [70, 71, 72, 73] or stretched-pulsed configurations [74, 75] without any active control. In these cases, any excess soliton pulse energy leads to quantization which, combined with high nonlinear phase shifts and fluences significantly beyond the saturable absorber saturation fluence [71], can induce pulse break-up. For high intracavity pulse energies, the decreasing pulse durations can no longer be supported by the limited gain bandwidth, and multiple-pulse operation with longer pulses at smaller energies is favored [76].

In the previously described 1 GHz SBR butt-coupled EDFL, harmonic mode-locking based on certain fiber birefringence and saturable absorber coupling states was observed. Self-organized pulses at twice the repetition rate were measured, as shown in Fig. 2-29. The optical spectrum of the 2 GHz EDFL was centered at 1566.8 nm with a 3-dB bandwidth of 9.3 nm. The fundamentally mode-locked laser featured a center wavelength of 1565.3 nm
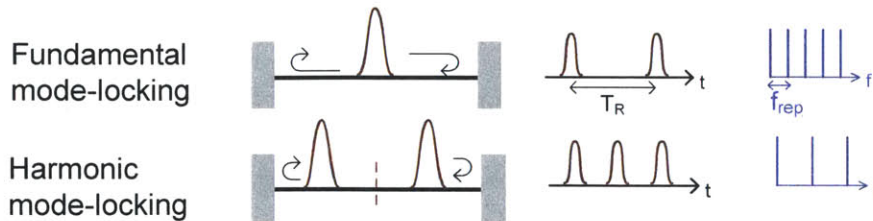
Figure 2-28: Schematic of fundamentally and harmonically mode-locked laser.
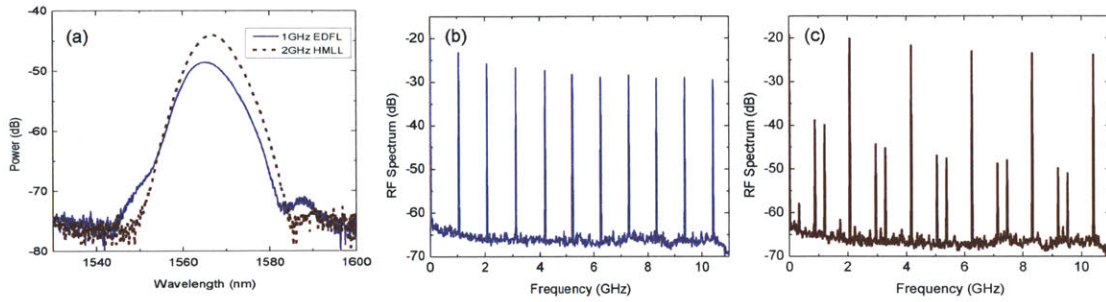
Figure 2-29: Fundamentally and harmonically mode-locked EDFL. (a) Optical spectra of fundamentally mode-locked 1 GHz EDFL and 2 GHz harmonically mode-locked EDFL. (b) RF spectrum of 1 GHz EDFL. (c) RF spectrum of 2 GHz HMLL EDFL. The side-bands in the RF spectrum are due to polarization rotation.

with a 10.9 nm 3-dB bandwidth, as shown in Fig. 2-29 (a), indicating only slightly longer pulse durations for the HMLL. At moderate launched pump powers of 280 mW and output powers of 10.8 mW, break-up into multiple pulses occurred. As higher output powers up to 27 mW and shorter pulse durations for the fundamentally mode-locked laser were observed in the same cavity configuration (compare Section 2.3.1), the fiber birefringence, intracavity losses and SBR coupling were critical to induce higher harmonic mode-locking. The RF measurements in Figs. 2-29 (b) and (c) verified that the RF properties of the 2 GHz output pulse train in terms of supermode noise suppression were on the same order as for the 1 GHz EDFL system. However, the HMLL featured polarization rotation side-bands in the RF spectrum in Fig. 2-29 (c) since it was challenging to suppress the side-bands while maintaining the harmonically self-organized pulse train. Therefore, to obtain stable, higher repetition rate output pulse trains, external repetition rate multiplication mechanisms offer a more reliable method as discussed in Chapter 4.

2.4.2 1.25 GHz Er-doped Fiber Laser

As introduced in the previous section, harmonic mode-locking is one option to extend the repetition rate of mode-locked lasers to higher multiples of the fundamental repetition rate. However, such operation comes at the trade-off of more complex pulse dynamics with

higher timing jitter. Therefore, in this section, the repetition rate of fundamentally mode-locked lasers is increased by reducing the cavity dimensions, as illustrated in Fig. 2-30 since improved timing jitter can be obtained in fundamentally mode-locked lasers.
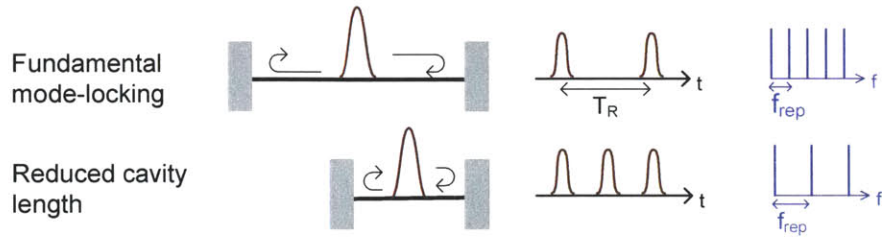
Figure 2-30: Schematic relating reduced cavity dimensions to higher repetition rates for fundamentally mode-locked lasers.

To reduce the cavity dimensions for the presented 1 GHz EDFL while exploiting SBR soliton-mode-locking, the gain fiber lengths of the cavity were reduced. For a cavity configuration similar to Section 2.2 with Liekki Er-80 8/125 gain fiber, no soliton mode-locking beyond 1.5 GHz could be observed since the average power became limited by the available gain. In the following, results are presented for an EDFL with a repetition rate of 1.23 GHz.
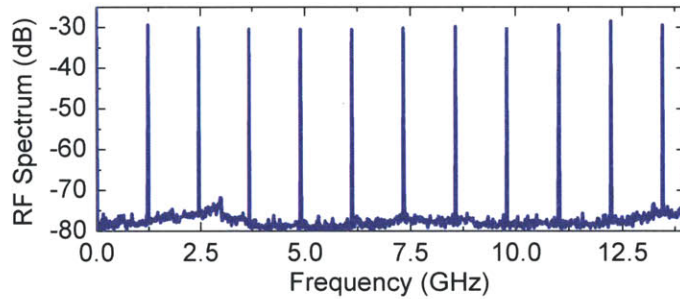
Figure 2-31: RF Spectrum of 1.23 GHz laser.

A repetition rate of 1.23 GHz (cf. Fig. 2-31) was achieved by reducing the cavity length to 77 mm of Er-doped gain fiber (Liekki Er-80 8/125) spliced to 6 mm of SMF-28e passive fiber. For a launched pump power of 290 mW (polarization combined pumps with pump currents of 1250 mA and 920 mA), the center wavelength of the optical spectrum was tunable so that three different mode-locked laser states were characterized, as summarized in Table 2.1. By
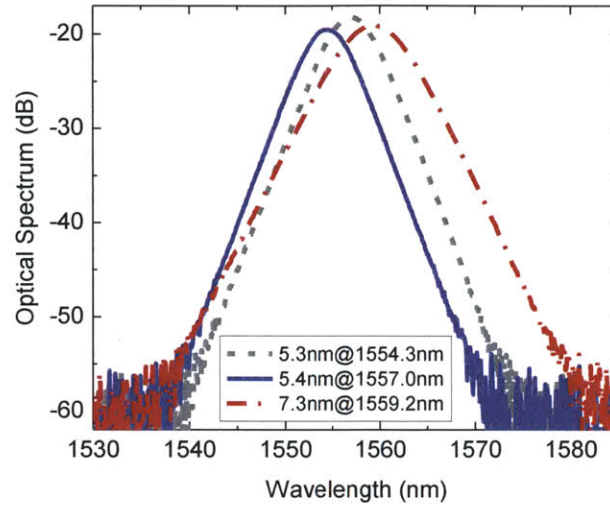
Figure 2-32: OSA traces for 1.23 GHz EDFL with wavelength tunability induced by the butt-coupling state.

Center Wavelength	3-dB Bandwidth	Output Power	Intracavity Pulse Energy
1554.3 nm	5.3 nm	19.0 mW	154 pJ
1557.0 nm	5.4 nm	20.1 mW	163 pJ
1559.2 nm	7.3 nm	22.9 mW	186 pJ

Table 2.1: Performance characteristics of three mode-locked laser states at 1.25 GHz, depending on butt-coupling to the SBR and induced fiber birefringence.

adjusting the gain fiber bend, the inherent birefringence, and the butt-coupling to the SBR, the center wavelength of the optical spectrum was changed between 1554.3 nm and 1559.2 nm, see Fig. 2-32. For longer wavelengths, the intracavity losses decreased, leading to higher pulse energies and stronger nonlinear spectral broadening as reflected by the increasing 3-dB spectral bandwidth from 5.3 nm to 7.3 nm (cf. Table 2.1). The laser cavity supported polarization locked vector solitons after adjustment of the fiber birefringence, as shown by the lack of polarization rotation side-bands in the RF spectrum in Fig. 2-31.

2.4.3 Polarization Maintaining Fiber Designs

Although the 1 GHz EDFLs were optimized for long-term stable operation, the procedure to find the desired operation wavelength regime and to suppress the polarization rotation

side-bands remained time-intensive. During this alignment process, the laser generally was not steadily mode-locked but mostly operated in a Q-switched regime. The SBR was thus exposed to significantly higher fluences than in steady-state and was therefore more susceptible to thermal damage. Reducing any transient states proved critical and was accomplished, e.g. with the polarization controller mount.

In an ideal cavity configuration, the polarization rotation would be suppressed without any external fiber cavity devices, which are sensitive to mechanical perturbations. To accomplish this goal, lasers were implemented in polarization maintaining Er-doped gain fiber (PM). Based on a comparable cavity configuration to the 1 GHz EDFL outlined in Chapter 2.2, 500 MHz PM fiber lasers consisting of 200.8 mm pure Nufern PM 7/125 (55 dB/m absorption and -22.7 fs^2/mm anomalous dispersion) were constructed. Two PM fiber lasers were built with an additional focus on determining how close the repetition rate could be reproduced. After measuring the fiber to 0.1 mm precision, the reflection of the cleaved fiber end resulted in a reflected signal characteristic to the cavity resonance. From the corresponding RF signal, the refractive index of the fiber was determined to $n = 1.46534$ with 5 digits accuracy.

Though the absorption in the 500 MHz PM gain fiber with 55 dB/m was slightly reduced in comparison to the Liekki 8/125 gain fiber with 80 dB/m, high single-pass pump absorption ratios of 76 % were observed for a single-pass through the cavity (compared to 30 % in the 1 GHz EDFL). For a cw laser cavity with two 10 % output couplers defining the cavity, ~ 65 % of the pump light was absorbed and intracavity powers of up to 246 mW measured for 320 mW of coupled pump power. This value was more than double the intracavity power that was determined for the 1 GHz EDFL in the corresponding set-up (50 % total pump absorption for 111 mW of intracavity power).

The mode-locking threshold for the 500 MHz lasers was fairly low at 85 mW of coupled pump power. Fig. 2-33 represents a selection of different spectral output states, centered at 1563 nm, 1557 nm and 1561 nm with 3-dB bandwidths of 10.1 nm, 9.8 nm and 9.0 nm, respectively. All three optical spectra featured a small hump at longer wavelengths. To obtain mode-locking at shorter wavelengths, the coupled pump power was increased to gen-
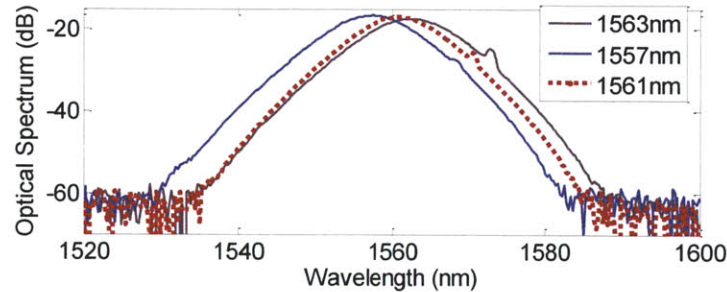
Figure 2-33: Optical spectrum for 509 MHz PM EDFL.

Center Wavelength [nm]	1556	1557	1561	1563	1578
FWHM Bandwidth [nm]	5.0	9.8	9.0	10.1	13.0
Output Power [mW]	3.3	6.3	5.6	5.8	6.7
Coupled Pump Power [mW]	118	212	150	118	150

Table 2.2: Different mode-locked laser states, characterized by center wavelength of optical spectrum and repetition rate for the same PM 500 MHz laser (EDFL2).

erate comparable 3-dB spectral bandwidths, as illustrated in Table 2.2. The presence of small air gaps was assumed to alter the encountered intracavity losses, making the longer wavelengths a more favorable state. Preliminary numerical simulations confirmed that for larger air gaps, the SBR reflectivity increased for longer wavelengths, as the reflectivity profile became tilted. In addition, the SBR dispersion was less anomalous, thereby decreasing the magnitude of the net dispersion, which led to reduced pulse durations, as a consequence of higher intracavity pulse energies and enhanced nonlinear broadening (compare Eq. 1.2). This was in good agreement with the empirical observation that loosening the butt-coupled contact significantly resulted in longer wavelength operation.

Fig. 2-34 (a) compares two different butt-coupled states for the two different PM fiber lasers EDFL1 and EDFL2. EDFL1 was mode-locked with a BATOP SAM-1550-9 SBR whereas EDFL2 utilized SBR VA86 (proton-bombarded with $1 \cdot 10^{15}$ at 40 keV). Both SBRs provided comparable performance. In the current configuration, the repetition rate between the two lasers is spaced apart by 100 kHz (see Fig. 2-34 (b) and (c)). It is expected that this offset can be adjusted by thermal tuning of the lasers. However, the key point of
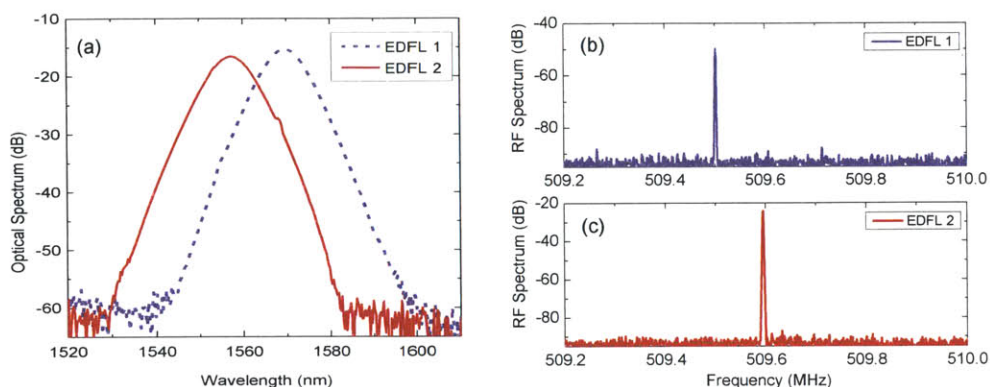
Figure 2-34: Comparison of two PM EDFLs. (a) Optical spectrum centered at 1570 nm and 1557 nm for EDFL1 and EDFL2. (b) EDFL1 featured a repetition rate of 509.50 MHz, (c) EDFL2 a repetition rate of 509.60 MHz.

mitigating the polarization rotation was addressed in these PM fiber lasers as no side-bands were noticeable in the RF spectrum.

To generate higher pulse energies, SBR butt-coupled PM fiber lasers at 204 MHz were constructed, using 49.9 cm of the same Nufern 7/125 PM Er-doped gain fiber. These lasers featured a high pump absorption of 89 % and up to 400 mW intracavity power for cw operation. As these lasers mode-locked (cf. Fig. 2-35), excessive damage of the SBR occurred as the VA86 PRC was not designed for the high fluence levels of up to $2.4 \, \mathrm{mJ/cm^2}$. Mode-locked lasers around 200 MHz in a stretched pulsed configuration (combining longer sections of passive fiber to reduce the gain fiber length) are currently being investigated with the goal of obtaining ultra-low timing jitter laser sources [77].

Incident fluences from this 204 MHz PM laser amounted up to $2.4 \, \mathrm{mJ/cm^2}$ on a coated SBR VA86 PRC and thus exceeded its saturation fluence of $3.7 \, \mu\mathrm{J/cm^2}$ by up to a factor of ~ 650. Though coated with a dielectric coating, operation of the SBR far beyond its saturation fluence was expected to lead to damage (cf. [68]). Thus, the extent of the damage was further analyzed through surface profilometer scans (performed by Sheila Nabanja). In Fig. 2-36 (a) a three-dimensional profilometer scan image is shown together with a cross-sectional cut in Fig. 2-36 (b) for the same severely damaged VA86 PRC. In this case, distinct
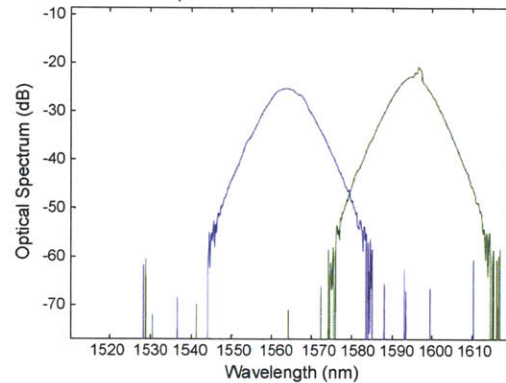
Figure 2-35: Mode-locked spectrum of 204 MHz PM EDFL.

craters are visible, with the deepest one extending over an area of $\sim 20\,\mu$m in diameter and up to $3\,\mu$m in depth, while the other damage spots did not exceed $1\,\mu$m depth with diameters smaller than $10\,\mu$m. For this SBR, the InGaAs absorber was located $\sim 1.5\,\mu$m below the surface of the SBR.

As Fig. 2-36 implies that material expulsion and redeposition might have occurred, a literature review on ablation in dielectric coatings was performed. However, laser induced damage thresholds for dielectric materials (mostly SiO_2) at a wavelength of 800 nm are quoted for sub-picosecond pulses at J/cm^2 fluences. The resulting high peak intensities experienced multi-photon impact ionization with free electrons leading to avalanche effects, thereby resulting in plasma formation and optical damage. In this regime, collateral damage was of secondary nature since the electrons absorbed the energy much faster than they were able to transfer the kinetic energy to the lattice [78, 79].

Any bulk damage thresholds are orders of magnitudes higher than the $2\,mJ/cm^2$ fluence levels encountered in the lasers. Even after taking the field enhancement in the quarter-wave dielectric layer stack into account, as performed by [80] and [81] for a SiO_2 and Ta_2O_5 coating at 800 nm, ablation thresholds are still on the order of $360\,mJ/cm^2$ or higher [80]. For GaAs ablation thresholds (cf. [82, 83, 84, 85]), the onset of ablative damage at 800 nm for 130 fs short pulses was noted for minimum fluence values of $\sim 90\,mJ/cm^2$ and crater formation with rims consisting of resolidified material was inflicted by pulse energies of at
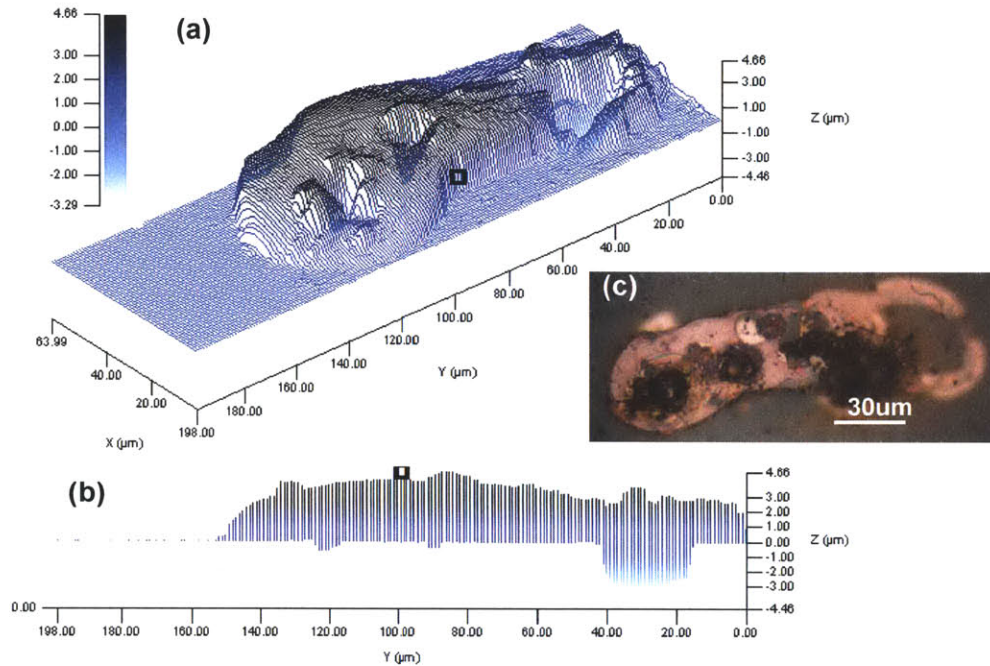
Figure 2-36: (a) Three-dimensional profilometer scan of damaged SBR VA86 PRC in 204 MHz laser, exposed to high fluence values. (b) Cross-sectional profilometer scan and (c) optical microscope image of the same SBR sample.

least 150 nJ [82].

However, in the developed EDFLs, operating wavelengths of ~ 1550 nm are larger than the GaAs absorption band-edge and the lasers operate at pulse energies significantly below the damage thresholds. Thus, the exact damage mechanism is still further studied and TEM studies are expected to reveal more insight.

2.4.4 External Free-Space Section Fiber Lasers

Instead of an all-fiber system, a fiber laser with a free-space section to focus on the SBR provided an alternative approach to remedy the above-mentioned challenges of thermal damage to the SBR and to address the lack of a polarization discriminating element. The free-space section spatially separated the gain fiber and saturable absorber. By choosing appropriate focusing lenses, the incident fluence on the SBR was modified. In addition, a
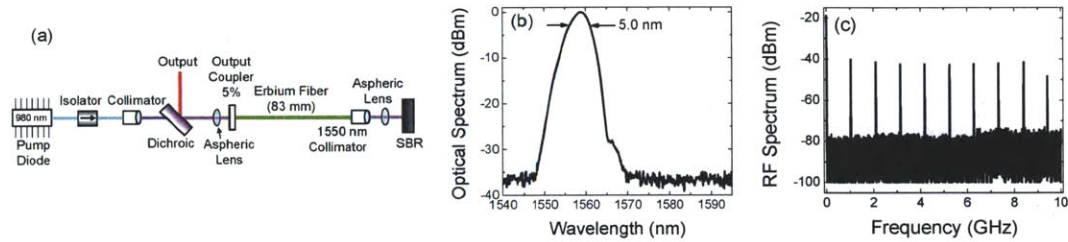
Figure 2-37: (a) Configuration of a free-space 1 GHz EDFL. (b) Optical spectrum and (c) RF trace.

thin-film polarizer could physically be incorporated in the free-space air path. However, collimating and coupling losses from fiber to free-space usually amounted to at least 20 %, so that a SBR with a higher modulation depth was necessary for efficient pulse-shaping (BATOP with 21 % absorber losses), cf. Fig. 2-37 (a). In addition, to attain repetition rates of 1 GHz, the gain fiber section was reduced to 75 mm in length (combined with a 29 mm long air path). These effects led to lower intracavity pulse energies of 20 pJ with a 5 nm FWHM spectral bandwidth at 1560 nm for the free-space fiber set-up, cf. Fig. 2-37 (b), compared to the butt-coupled EDFL, which featured intracavity pulse energies up to 283 pJ. Stable mode-locking at 1.05 GHz repetition rates was confirmed in Fig. 2-37 (c). These results were obtained in collaboration with David Chao and Jonathan Morse.

Replacing the free-space pump end section with the coated output coupled ferrule improved the pump coupling efficiency into the gain fiber. Thus, the gain section was further reduced to 62 mm for a repetition rate of 1.26 GHz. This laser was mode-locked with a 12 %-modulation depth BATOP SBR and the laser featured an 8 pJ intracavity pulse energy with a 5.9 nm 3-dB bandwidth at 1556 nm (pump power of 360 mW). For stable mode-locking, a 3 mm lens focused the beam diameter to a ∼4 mm diameter spot on the SBR.

In general, the butt-coupled EDFL configurations provided superior optical performance, higher output power and were less sensitive to environmental perturbations. However, if exact repetition rate tuning is required, the free-space fiber lasers provide a good solution. More details on external cavity fiber lasers can be found in Section 3.3.
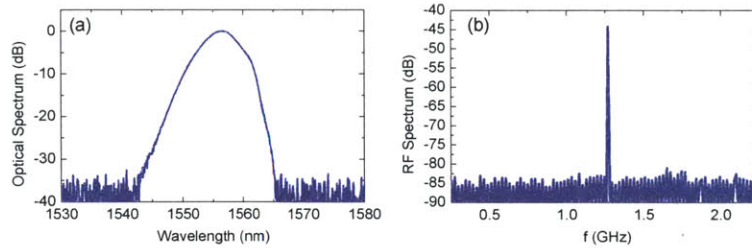
Figure 2-38: EDFL with an external free-space section. (a) Optical spectrum centered at 1556 nm with 5.9 nm 3-dB bandwidth and (b) a repetition rate of 1.26 GHz.

2.5 Applications

The development of the butt-coupled 1 GHz laser with good optical performance metrics fueled the demonstration of two enabling technologies in our group: a 1 GHz frequency comb at 1550 nm and a photonic sampling system.

2.5.1 1 GHz Er-doped Self-Referenced Frequency Comb

For carrier-envelope offset (CEO) control by 1f-2f self-referencing techniques, the respective 1f and 2f frequencies have to feature significant optical power within a generated super-continuum spectrum. To employ highly nonlinear fiber, pulse energies in the nJ regime are generally required, which at repetition rates of 1 GHz translates into average powers at the W level. Thus, key developments by David Chao comprised of a Raman ampli-fier so that in successive amplifier and compressor stages an average power greater than 2 W, corresponding to a 2 nJ pulse energy, was achieved. This allowed the generation of an octave-spanning supercontinuum in a short section of highly-nonlinear-fiber, spanning wavelengths from 1 μm to 2.4 μm. The carrier envelope offset frequency f_{ceo} beat was locked to stable microwave reference oscillators, yielding the first octave-spanning self-referenced optical frequency comb that was centered at the 1.55 μm telecommunication band and that operated with a GHz repetition rate [86, 87]. Such a self-stabilized frequency comb, which can be externally multiplied to higher repetition rates, provided a significant milestone in the OAWG project towards a phase-stabilized oscillator at multi-GHz repetition rates.

2.5.2 Photonic Sampling System

To implement photonic ADC systems, low-timing jitter GHz femtosecond sources for high resolution digitization are required. With the 1 GHz EDFL, an ADC consisting of discrete components (cf. Fig. 1-4), with 7.0 ENOB resolution for a 41 GHz signal was demonstrated. In an integrated version, implemented in Si photonics, a 10 GHz signal was digitized with 3.5 ENOB [30], emphasizing the future potential of photonic sampling systems from an integrated photonics platform. For more details the reader is referred to [27].

2.6 Conclusion and Future Work

In this chapter, fundamentally mode-locked, GHz fiber laser systems were presented. 187 fs short pulses, centered at 1573 nm for an output power of 28.8 mW were demonstrated. Additional mode-locked states within the C-band were found by modifying the butt-coupling state and fiber birefringence to tune the center wavelength of the optical spectrum.

The lack of a polarization discriminating element within the cavity induced the formation of polarization rotating vector solitons. Adjustment of the fiber birefringence led to a polarization locked output pulse train, which was demonstrated also from a custom-machined polarization mount. Thermal damage to the saturable absorber due to high residual pump power and Q-switching in the laser was successfully minimized so that long-term stable operation was achieved.

Mitigating Q-switching in the cavity and completely eliminating SBR damage, can potentially be attained by careful design of the absorber layers and using cladding layers with higher two-photon absorption (e.g. InP) which reduce Q-switching in the cavity. In addition, the individual mode-locked states can be explored further with respect to their noise properties and timing jitter. One pathway forward for low timing-jitter sources could be lower repetition rate stretched pulsed laser systems, since these latter systems were shown to posses lower timing jitters [77].

Chapter 3

External Repetition Rate Multiplication with Interleavers

In Chapter 2, compact fundamentally mode-locked Er-doped fiber lasers based on commercially available gain fibers were presented. However, as the repetition rate is limited to around 1.5 GHz, external repetition rate multiplication methods are pursued to achieve pulse trains with repetition rates in the multi-GHz regime. In this chapter, a novel planar circuit interleaver is designed to generate a 10 GHz femtosecond pulse train. Characterization of the interleaver chips and optical performance results are discussed in detail. This chosen technology provides a robust and compact solution compared to alignment-sensitive free-space approaches.

3.1   Motivation

Frequency combs have become an enabling technology for a vast range of applications. Combs with wide frequency spacing - at repetition rates of 10 GHz or higher - exhibit the advantage that their individual frequency lines can be accessed with current filter and modulator technology to efficiently shape the frequency spectrum. Thus, high repetition rate femtosecond oscillators are attractive for optical arbitrary waveform generation [19],

high-resolution sampling and frequency metrology [12]. Furthermore, frequency combs have successfully opened a pathway to improve the calibration accuracy of astronomical spectrographs [20, 21, 22]. In order to detect extra-solar planets, changes in the radial velocity of stars with extra-solar planets are measured by Doppler shifted starlight, as described in Section 1.1.3. However, to utilize the precision of frequency combs, their comb teeth have to be separated by at least 10 GHz or higher in order to be compatible with the operating regime of existing spectrographs. Currently, fundamental frequency combs at lower repetition rates are therefore externally filtered with Fabry-Perot cavities to obtain the desired multi GHz spacing and to suppress the extraneous comb lines by ~ 25 dB [21, 22]. However, any non-uniform intensity distribution, like asymmetric amplitudes of the filtered side-modes in the frequency comb, gets enhanced in any nonlinear broadening process used to obtain a wide-band frequency comb. This leads to a center of gravity frequency shift that can result in systematic wavelength offsets, limiting the detection resolution and distorting the absolute stellar radial velocity values. Therefore, a long-term stable, wide-spaced frequency source with high wavelength accuracy and good side-mode suppression is essential to identifying planets beyond the resolving range of current state-of-the-art spectrographs.

Optical frequency combs can also be utilized to generate low-noise microwave signals through optical frequency division [88, 89, 90]. By detecting the optical pulses with a wide-bandwidth photodiode, an electric pulse train is generated, consisting of single tones at the laser repetition rate and its harmonics up to the cut-off frequency of the detector. The phase-coherence of the optical lines enables a RF signal train with good stability, low noise and high spectral purity. After subsequent filtering of the desired RF frequency line, the obtained microwave source can outperform current state-of-the-art low-phase microwave oscillators. Diddams *et al.* [91] demonstrated an improvement in the shot-noise-limited signal-to-noise performance of higher harmonic microwave signals by external optical filtering with a Fabry-Perot cavity before detection on the photodiode. Thus, for the filtered 10 GHz signal, a 10 dB signal strength could be gained, compared to the 10th harmonic of the fundamental 1 GHz source. Instead of a Fabry-Perot cavity to filter the signal, which requires a high finesse for sharp transmission peaks, interleavers based on Mach-Zehnder interferometers

present an elegant alternative. These interleavers can be implemented in planar waveguide circuits with a small and compact footprint. As such, they have distinct advantages over free-space, alignment sensitive set-ups like Fabry-Perot cavities, since they offer long-term reliability, robustness and easy portability.

Interleaver filters that are based on planar waveguide technology have consistently evolved over the years, in particular for dense wavelength division multiplexed optical fiber systems. To satisfy the growing demand for more information capacity, fiber coupled and planar waveguide optical interleavers have been utilized to increase the channel spacing. These interleaving filters were primarily designed for wide-bandwidth pass-bands by cascading multiple stages and optimizing the coupling coefficient ratios at each individual interleaver stage in order to achieve operating frequencies around 50-100 GHz [92, 93, 94, 95]. Good overviews over different interleaver implementations can be found in Cao [96] and Kawachi [97], who outlines the various silica waveguide technology components. Waveguide interleavers can be directly coupled to existing fiber platforms or integrated in the same fabrication process with silicon photonics, thus providing a compact solution with robust performance metrics. In addition, the waveguide chip fabrication is scalable. For this work, technology elements of interleavers with thermal phase shifters are combined to explore coherent pulse interleaving. By cascading several interleaver stages, higher multiples of the initial repetition rate are achieved.

To realize optical time division multiplexing systems with transmission speeds above 1 Tbit/s, femtosecond pulses can be used in combination with different fiber based techniques [98]. Recently, Nakazawa demonstrated a 32-times interleaved femtosecond-pulse system for 2.56 Tbit/s/ch polarization multiplexed transmission with reduced polarization-mode dispersion impairments in a differential quadrature phase-shift keying configuration [99]. For these applications, the pulses have to arrive within given time slots, however, the frequency response in the optical domain is of secondary nature and is not necessarily optimized for a high side-mode suppression. For frequency comb applications, exact timings and phase-coherency are crucial to obtain a clean frequency comb with good side-mode suppression. Thus, planar waveguide interleavers for coherent pulse interleaving of

femtosecond pulses, where the phase-coherent property of the pulses is maintained, will be studied. An integrated waveguide system consisting of a 500 MHz waveguide laser that was combined with a two-stage interleaver to produce a 2 GHz fs-pulse output train was previously demonstrated [100]. However, the maximum RF side-mode suppression was limited to 15 dB due to fabrication tolerances in the coupling ratios.

In the following, a hybrid system of an Er-doped fiber laser combined with silica waveguide interleavers is presented. The goal of this research is to demonstrate that an integrated waveguide device can be utilized for coherent pulse interleaving at 1550 nm and for scaling the repetition rate to 10 GHz. The interleavers are designed specifically to incorporate a thermal tuning mechanism so that fabrication tolerances that otherwise limit the side-mode suppression can be compensated. Combining the recent progress in mode-locked fiber lasers [101, 102, 103] with waveguide interleavers enables the repetition rate of a fundamentally mode-locked femtosecond laser to be reliably scaled by a factor of 16. At the same time, a good side-mode suppression of at least 30 dB is achieved and a compact footprint and robust system to obtain a 10 GHz coherent pulse train is demonstrated. The following results underline the promising potential of this technology for various applications in science and engineering.

3.2 Interleaver Design

In this section, design considerations to obtain multi-GHz-spaced frequency lines in a waveguide interleaver are discussed.

3.2.1 10 GHz Pulse Train Interleaver Parameters

The operating schematic for waveguide interleavers, implemented in planar waveguide technology, is illustrated in Fig. 3-1. In each interleaver stage, the input signal is divided by a directional coupler into two pulse trains, one of which experiences a differential delay $\tau_1 = \frac{1}{2 \cdot f_{rep}}$ of half the initial pulse train spacing $T_R = 1/f_{rep}$, before both waveguide arms are re-combined. By incorporating two interleavers with the respective delay line lengths
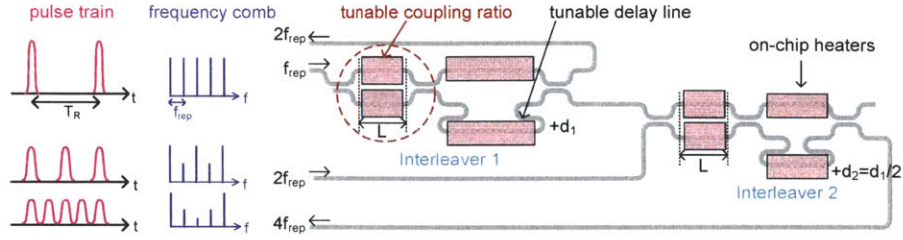
Figure 3-1: Schematic of a two-stage interleaver to quadruple the input repetition rate.

$d_1 = c/(n \cdot \tau_1)$ and $d_2 = d_1/2$ (with c the speed of light and n the refractive index) on the same interleaver chip, the input repetition rate is quadrupled on each chip. This first interleaver chip, consisting of a 2-stage interleaver, is cascaded with a second interleaver chip, featuring another 2-stage interleaver with respective delay line lengths of $d_3 = d_1/4$ and $d_4 = d_1/8$ (for exact lengths see Table 3.1). Thus, in four interleaver stages on two chips, the repetition rate can be multiplied by a factor of 16.

Description	Parameter	Length
Input repetition rate	$f_{rep,in}$	625 MHz
Delay line length stage 1	d_1	16 cm
Delay line length stage 2	d_2	8 cm
Output repetition rate	$f_{rep,out}$	2.5 GHz
Input repetition rate	$f_{rep,in}$	2.5 GHz
Delay line length stage 1	d_3	4 cm
Delay line length stage 2	d_4	2 cm
Output repetition rate	$f_{rep,out}$	10 GHz

Table 3.1: Design parameters for the four interleavers to obtain a repetition rate multiplication by a factor of 16.

The output field E_1 of the first interleaver stage can be mathematically expressed in terms of the incoming electric field E_0, a power coupling coefficient of c_1 for the first directional coupler at the input in Fig. 3-1 and of c_2 for the directional coupler at the end

of the first interleaver stage, as described in Eq. 3.1.

$$E_1 = \sqrt{c_1 \cdot c_2} \cdot E_0 + \sqrt{(1 - c_1) \cdot (1 - c_2)} \cdot \exp\left(-j\, 2\,\pi\tau_1 f\right) \cdot E_0 \tag{3.1}$$

$$I_1 = E_1 \cdot E_1^*$$

$$= \left[c_1\, c_2 + (1 - c_1) \cdot (1 - c_2) + 2\,\sqrt{c_1\, c_2 \cdot (1 - c_1) \cdot (1 - c_2)} \cdot \cos\left(2\,\pi\tau_1 f\right) \right] \cdot E_0^2 \tag{3.2}$$

In Eq. 3.2, I_1 denotes the intensity at the output of the first interleaver stage, and f represents the frequencies in the RF domain. For a time delay of $\tau_1 = \frac{1}{2 \cdot f_{rep}}$, the resulting output frequencies are maximized if the arguments of the cosine correspond to a multiple of 2π:

$$\Delta\phi = 2\,\pi\tau_1 f = m\, 2\,\pi,$$

with m being an integer. Thus, multiples of the repetition rate f_{rep} at

$$f = 2\, m\, f_{rep}$$

are maximized, while frequencies at

$$f = 2\,(m + 1)\, f_{rep}$$

are filtered out: The output power is proportional to a cosine curve depending on the accumulated phase shift $\Delta\phi$ which doubles the input repetition rate for specific values of f.

3.2.2 Modeling of Femtosecond Pulse Interleaver

The goal of the designed interleaver system is to generate a clean frequency response with a high side-mode suppression in the optical domain. Therefore, as a first step, detailed modeling was conducted to understand the impact of various parameters on the side-mode suppression.

In Fig. 3-2 (a), the optical transmission of a two-stage interleaver from 625 MHz to 2.5 GHz was modeled as the blue continuous curve (normalized to the maximum transmis-

sion). In an ideal system, the frequency lines exactly coincide with the peaks and valleys of the transmission curve, resulting in an extremely high suppression. However, in any real system, dispersion (modeled here with an anomalous waveguide dispersion $D = -5\,\text{fs}^2/\text{mm}$) limits the overall achievable filter response, as illustrated in Fig. 3-2 (a). In order to relate the transmission curve (blue curve) to the expected optical suppression for a femtosecond pulse train, red dots mark multiples of the repetition rate at 625 MHz. The waveguide dispersion shifted the optical transmission curve slightly towards longer wavelengths since the time delay accumulated in the delay lines got modified by group delay dispersion. Thus, over a given wavelength interval (a wavelength range of 80 pm corresponds to 10 GHz), a walk-off between the frequency lines and the minima in the transmission curve occurred, reducing the side-mode suppression. For a one-stage interleaver from 625 MHz to 1.25 GHz (625 MHz correspond to a wavelength spacing of 5 pm), the impact of waveguide dispersion for the maximum and minimum values at harmonics of the repetition rate (in this case of 623 MHz) is plotted in Fig. 3-2 (b). The side-mode suppression in Fig. 3-2 (b) decreases with increasing wavelength offsets from 1560 nm due to group delay: Over a large bandwidth the filter notches and frequency lines eventually became significantly misaligned. This process is periodic in wavelength and, in this particular case, a good suppression was reached again within an 8 nm interval. As the dispersion accumulated in subsequent stages is smaller due to the shorter delay line lengths in the interleaver arms, the first interleaver stage contributes the limiting effect in such a configuration.

So far, ideal coupling ratios for the directional couplers were assumed in the analysis. However, the coupling efficiency depends on the effective coupler length and the gap between the two waveguide arms, which is fabrication sensitive. Thus, deviations from the ideal 50 % - 50 % splitting ratio by at least ± 5% have to be considered. For a coupling ratio of 60 % - 40 % in all directional couplers, the side-mode suppression degrades further and becomes limited by the coupling coefficient offsets, as marked by the black stars in Fig. 3-2 (a).

Aside from fabrication tolerances impacting the coupling ratio, also length offsets in the fabricated delay line lengths have to be taken into account. Such offsets modify the
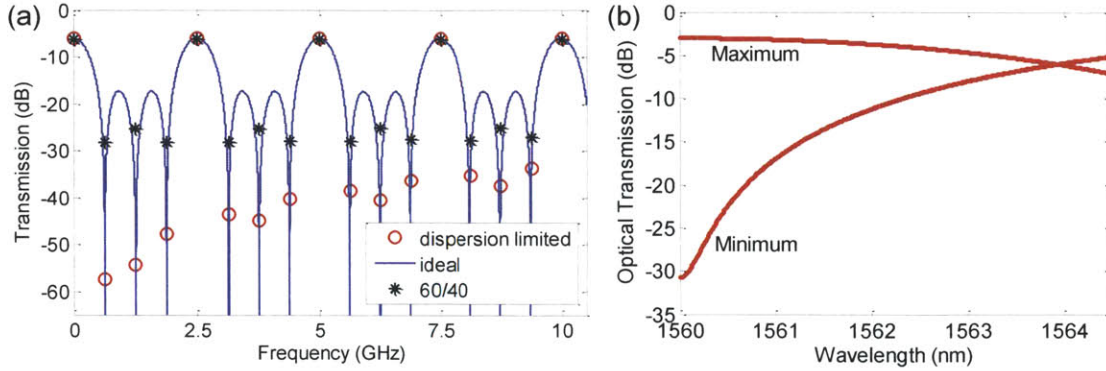
Figure 3-2: (a) Modeled transmission of two-stage interleaver from 625 MHz to 2.5 GHz with red dots/black stars marking multiples of the repetition rate at 625 MHz. (b) Limited side-mode suppression for one-stage interleaver due to waveguide dispersion $(D = -5\,\text{fs}^2/\text{mm})$.

accumulated phase shift $\Delta\phi$ in Eq. 3.2, which can be expressed in terms of an additional time delay $\Delta\tau$ or a corresponding delay line length offset ΔL:

$$\Delta\phi = 2\pi(\tau_1 + \Delta\tau)f = \frac{2\pi n}{\lambda}(d_1 + \Delta L) \tag{3.3}$$

Fig. 3-3 shows the transmission for the two-stage interleaver, including anomalous wave-guide dispersion of $D = -5\,\text{fs}^2/\text{mm}$, offsets in the coupling coefficients of around ± 2-$3\,\%$ and a delay line length offset of $0.01 \cdot \lambda$. In Fig. 3-3 (a), both interleaver delay lines are characterized by a $\sim 15.5\,\text{nm}$ physical length deviation, whereas in Fig. 3-3 (b) the first and second interleavers are implemented with a $0.01 \cdot \lambda$ and $0.005 \cdot \lambda$ offset, respectively. These additional phase shifts that are accumulated in the longer delay line length arm degrade the phase-coherence of the output pulse train. Thus, to compensate for such deviations it is crucial to have some post-processing tuning mechanism.

However, the limiting effects of anomalous waveguide dispersion, coupling offsets and length tolerances can be slightly compensated for by optimizing the repetition rate with respect to the interleaver response. In Fig. 3-4, the optical transmission, including off-sets in the coupling ratio of ± 2-$3\,\%$, dispersion, and delay line lengths deviations of
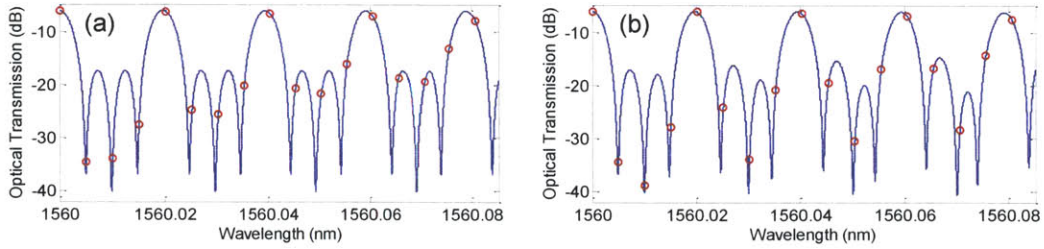
Figure 3-3: Two-stage interleaver with delay line length offsets of (a) $0.01 \cdot \lambda$ in both interleavers and (b) $0.01 \cdot \lambda$ and $0.005 \cdot \lambda$ for the first and second stage, respectively. The dots mark multiples of the repetition rate at 625 MHz.

$0.004\,\lambda = 6.24$ nm (corresponding to an additional time delay of 6.4 ps) for a repetition rate of (a) 625 MHz and (b) 622 MHz is shown. Assuming that a mechanism to compensate for larger fabrication tolerances is incorporated in the final interleaver design, only a smaller residual offset in the delay line lengths, which is representative of the uncompensated length offsets, is assumed. The walk-off between the harmonics of the repetition rate and the interleaver filter can be compensated for by adjusting the repetition rate to slightly lower values. This further optimizes the side-mode suppression, even in the presence of remaining length deviations.
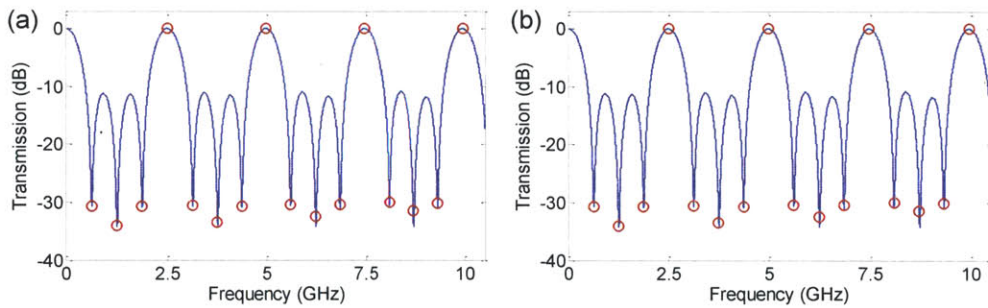
Figure 3-4: Two-stage interleaver transmission for delay line length offsets of $0.004\,\lambda$ for a (a) 625 MHz repetition rate, and (b) 622 MHz repetition rate.

Numerical evaluations in the time domain revealed that temporal broadening due to group velocity dispersion of the pulses themselves can be neglected. For a FWHM pulse duration of 420 fs, the total accumulated dispersion in the 4-stage interleaver system amounted

to $-1500\,\text{fs}^2$ (based on the measured waveguide dispersion of $-5\,\text{fs}^2/\text{mm}$). This induced a negligible total dispersive phase shift of $\sim 0.02\,\text{rad}$. Theoretical modeling confirmed that no significant pulse stretching occurred ($< 0.5\,\%$ in pulse duration). Moreover, for the considered frequency comb applications, the absolute pulse duration itself is only of secondary nature, as long as the desired spectral bandwidth is covered.

3.2.3 Implementation of Phase-Coherent Pulse Interleaver

The detailed analysis in the previous section emphasized the importance of post-fabrication tuning mechanisms in order to match the repetition rate with the interleaver filter spacing. Moreover, in order to obtain phase-coherent output pulses with a high side-mode suppression ratio, the absolute positions of the frequency lines have to coincide with the filter notches, requiring an 'interferometric'/coherent pulse interleaving process. Fig. 3-5 illustrates the developed solution: Tuning mechanisms to compensate for any fabrication tolerances were implemented so that the delay lines could be tuned to the desired length by thermal heaters. Therefore, heaters were included on top of each interleaver delay line. In order to achieve exact phase delays and an effective 50/50 splitting ratio, an additional Mach-Zehnder interferometer with a thermally tunable waveguide section of $L \sim 2\,\text{mm}$ was included for each stage. For a thermal expansion coefficient α in glass/silica of $8.5\,\text{ppm/K}$, a phase shift of π, corresponding to an optical length change of $\Delta L = \frac{\lambda}{2 \cdot n} = 527\,\text{nm}$ (with $n = 1.47$) can be expected for the following temperature change of ΔT of the waveguide core: $\Delta T = \dfrac{\Delta L}{\alpha \cdot L} = \dfrac{\lambda/2n}{8.5 \cdot 10^{-6} \cdot 2\,\text{mm}} = 31°\text{C}$. The induced relative phase-shifts by thermal tuning of the heaters on the Mach-Zehnder interferometers with up to $50\,\text{mW}$ of applied heater power counterbalanced nominal deviations of $\pm\,5\%$ from 50% in the coupling ratio.

3.2.4 Modeling of Phase-Coherent Interleaver

The phase-coherent interleaver response was modeled based on Eq. 3.1, by including an additional Mach-Zehnder interferometer stage for fine-tuning of the phase. Fig. 3-6 denotes the
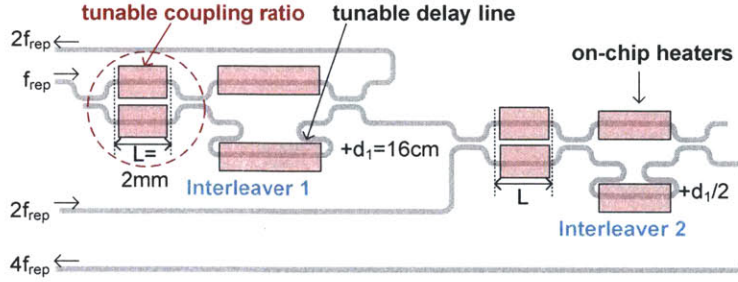
Figure 3-5: Design of thermally tunable interleaver with on-chip heaters to tune the coupling ratio and the delay line lengths.
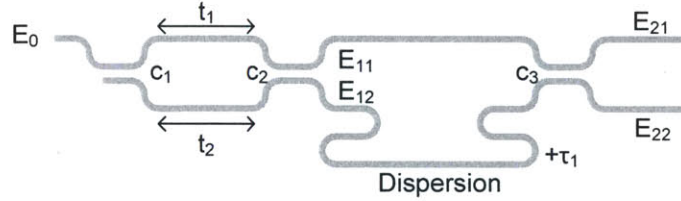
Figure 3-6: Schematic for interleaver modeling with power coupling coefficients c_i and temporal delays t_i and τ_i accumulated for the individual electric fields.

power coupling coefficients c_1, c_2, c_3 and temporal delay τ_1 for the differential delay line. The first Mach-Zehnder stage with a length of $\sim 2\,\text{mm}$ in both arms was modeled by t_1 and t_2 so that the impact of thermal tuning on each waveguide arm was independently controlled. Experimentally, heaters on the delay line and opposite waveguide arm were necessary to induce relative offsets. However, for the modeling, these differential offsets (of positive and negative value) were lumped into τ_1. Waveguide dispersion (with $D = -5\,\text{fs}^2/\text{mm}$ as measured) was incorporated for the long delay line arm. Dispersive effects were assumed negligible for all other waveguide sections since their lengths were significantly shorter ($L \sim 2\,\text{mm}$ compared to $d_1 = 16\,\text{cm}$).

In Eq. 3.4 and Eq. 3.5, E_{11} and E_{12} describe the electric field at the output of the additional Mach-Zehnder interferometer. The electric fields E_{21} and E_{22} in Eqs. 3.6 and 3.7

describe the output of the first interleaver stage.

$$E_{11} = \sqrt{c_1 \cdot c_2} \cdot E_0 + \sqrt{(1 - c_1) \cdot (1 - c_2)} \cdot \exp\left[-j\,2\,\pi \cdot t_1 \cdot f\right] \cdot E_0 \tag{3.4}$$

$$E_{12} = j \cdot \sqrt{c_1 \cdot (1 - c_2)} \cdot E_0 + j \cdot \sqrt{(1 - c_1) \cdot c_2} \cdot \exp\left[-j\,2\,\pi \cdot t_2 \cdot f\right] \cdot E_0 \tag{3.5}$$

In these equations, the constant dispersive phase that was imparted by the optical carrier frequency $f_0 = 193.5\,\mathrm{THz}$ was extracted since it added the same linear phase offset to both pulse trains. By varying the coupling coefficients, the delay offsets in the waveguides and the input repetition rate, this model provided better understanding of the experimental results. This framework formed the theoretical background for all of the simulations that are presented in this Chapter.

$$E_{21} = -\sqrt{c_3} \cdot \exp\left[-j\,2\pi \cdot \tau_1 \cdot f \; - \; j\,\beta\left[2\,\pi\,(f \; + \; f_0)\right]^2 + \; j\,\beta\,(2\,\pi\,f_0)^2\right] \cdot E_{11}$$
$$+ j \cdot \sqrt{1 - c_3} \cdot E_{12} \tag{3.6}$$

$$E_{22} = j \cdot \sqrt{1 - c_3} \cdot \exp\left[-j\,2\pi \cdot \tau_1 \cdot f \; - \; j\,\beta\left[2\,\pi\,(f \; + \; f_0)\right]^2 + \; j\,\beta\,(2\,\pi\,f_0)^2\right] \cdot E_{11}$$
$$- \sqrt{c_3} \cdot E_{12} \tag{3.7}$$

3.2.5 Fabrication Details

In order to obtain low loss and low dispersion waveguides around 1550 nm, passive Ge-doped $4\,\mu\mathrm{m} \times 4\,\mu\mathrm{m}$ silica waveguides with a $10\,\mu\mathrm{m}$ silicon oxide cladding were fabricated by CyOptics, Inc., on a silicon wafer substrate. The high index contrast of 1.5% allowed tighter bending radii ($> 1\text{-}2\,\mathrm{mm}$) for the waveguide without introducing significant mode losses. A folded design layout was pursued to obtain a compact chip, in particular of interest for the interleaver stages with longer delay lines ($d_1 = 16\,\mathrm{cm}$ for the first interleaver stage from 625 MHz to 1.25 GHz). Two interleaver stages were integrated on each chip with a footprint of 19.4 mm x 10.5 mm. To multiply the repetition rate by a factor of 16 from 625 MHz to 10 GHz, four interleaver stages were designed and fabricated on two different interleaver chips.
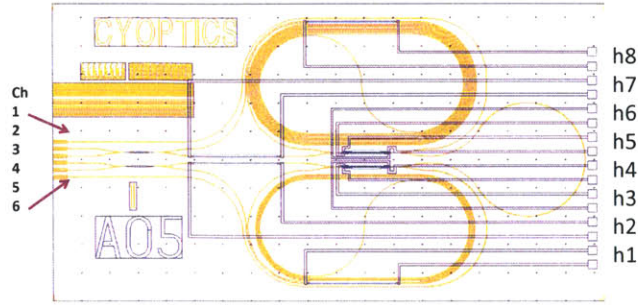
Figure 3-7: Layout of interleaver chip with a grid of 1 mm, adapted from CyOptics. The heaters are color-coded in light blue, the heater metalization in purple and the waveguides in orange/red. The numbering was introduced for later reference to specific heaters or input channels.

The actual chip layout is shown in Fig. 3-7 and illustrates the waveguides and the position of eight Cr heaters per chip and metalization. The cross-section of the waveguide chip consists of Ge-doped waveguide cores embedded in a 10 μm silicon dioxide cladding with a 100 nm thick Ti 'glue' layer on top. A 200 nm thick Pt barrier layer was deposited beneath the 100 nm thick Cr heaters. The metal contacts on top of the heaters consisted of Au.

In order to minimize coupling losses to a permanently attached fiber array with regular SMF-28e fiber, mode-converters tapered the mode size from waveguide dimensions of 4 μm x 4 μm to 7 μm x 7 μm. The waveguide input/output facets were polished at an angle of 8° to minimize possible back-reflections. As the mode size was matched well to regular SMF-28e fiber, direct coupling from the interleaver to a permanently attached fiber array (six input fibers with a pitch of 250 μm) resulted in a good coupling efficiency.

The interleaver chips were attached with thermally conductive silver paste to a special copper mount. The heater connection pads were gold wire-bonded to the fingers of a custom-designed printed circuit board (PCB, initial layout by Marcus Dahlem) so that each heater could be individually controlled through a digital-to-analog converter board (DAC). Gold wire-bonding with 1 mil diameter wire resulted in around 160 μm pitches on the metal heater pads. As the wire was mechanically broken by ultrasonic vibrations, the starting point of the wire-bonding was crucial: Since the PCB was slightly elevated with

respect to the interleaver chips on the engineered mount, wire-bonding from a lower point to a higher target was favored. Thus, the first bond pad connection was made on the heater pads and was then run to the respective finger on the printed circuit board. A picture of the two mounted interleaver chips is shown in Fig. 3-8. Unfortunately, on the second interleaver chip, wire-bonds lifted off, so that electrical contact to only five out of eight heaters could be established (heaters 5, 6, and 8 were not connected).
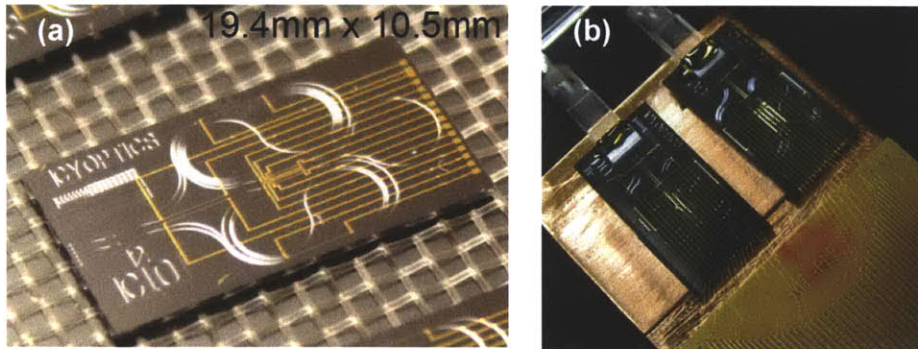
Figure 3-8: Photograph of interleaver chip with dimensions of 19.4 mm x 10.5 mm. For the wire-bonded interleaver chips the upper interleaver multiplies the repetition rate from 625 MHz to 2.5 GHz, while the bottom one quadruples it to 10 GHz.

The wire-bond connections between the heater pads and the PCB fingers featured resistances mostly around 300 Ω. With a digital-to-analog converter board, a constant voltage source was adjusted accordingly so that each heater could be individually addressed with a maximum electric power of 50 mW. For higher electrical powers, an external voltage source was utilized.

3.3 Experimental Set-Up: Er-doped Fiber Laser at 625 MHz

For this interleaver design, the interleaver was intentionally de-coupled from the waveguide chip so that the overall yield could be improved by selecting the most efficient interleaver chip and combining it with an optimized available laser source. A fiber laser configuration was chosen to supply a repetition rate tunable femtosecond laser source: A soliton mode-

locked fiber laser served as the input source to the waveguide interleaver chip, see Fig. 3-9. The linear fiber laser cavity consisted of 12.5 cm long Er-doped gain fiber (Liekki Er80-8/125 with anomalous dispersion of $-20\,\mathrm{fs^2/mm}$) that was imaged onto an in-house fabricated semiconductor saturable Bragg reflector (VA86 PRC and VA148 PRC) [101, 102, 103]. For details on the saturable absorber, the reader is referred to Chapter 2.2 or Chapter 5. The gain fiber end that faced the free-space section was polished and epoxied into a FC/APC connector to minimize any back-reflections which could otherwise counteract the mode-locking. The collimated fiber output (Thorlabs F240APC-1550) was focused on the SBR by an aspheric lens (Thorlabs A240TM-C or C240TM-C). Both lenses featured a focal length of 8 mm so that the beam diameter ($\sim 8\,\mu\mathrm{m}$) at the fiber output was imaged directly onto the SBR. The other end of the gain fiber was butt-coupled to a FC/PC ferrule in a mating sleeve to provide 10 % output coupling. To mitigate any polarization rotation of the output pulses (compare Chapter 2.3.3), a thin-film polarizer in the free-space section served as a polarization discriminating element that ensured a certain intracavity polarization and thus suppressed the periodic polarization rotation of vector solitons [60]. The experimental set-up is shown in Fig. 3-9.
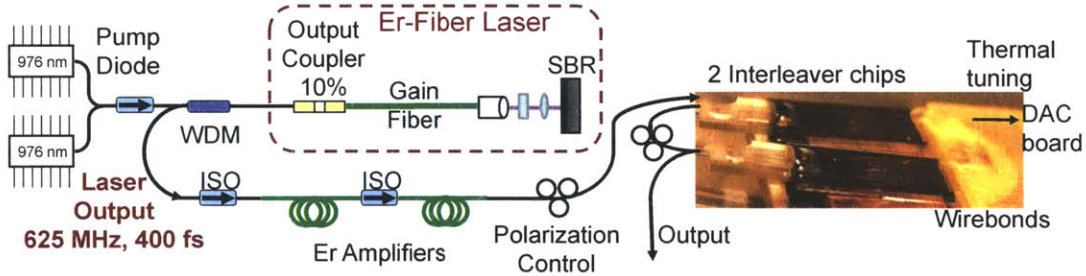
Figure 3-9: Experimental set-up, consisting of a free-space, repetition rate tunable 625 MHz EDFL, amplifiers and the waveguide interleavers.

The choice of a thin-film polarizer in terms of insertion losses, thickness and AR coating was critical as the polarizer was used as an intracavity element. A commercially available LP NIR polarizer from Thorlabs was tested but the single-pass transmission of 85.5 % for the wavelength region of interest introduced too high intracavity losses and prevented mode-

locking. A custom-ordered thin-film polarizer (dimensions of $3\,\text{mm} \times 3\,\text{mm}$ and $0.5\,\text{mm}$ thickness) exhibited a higher measured transmission of 98.5 %. The polarizer (inset of Fig. 3-10) was glued to a half inch diameter ring and mounted such that the rotation could be adjusted to the preferred polarization to minimize intracavity losses, cf. Fig. 3-10. In Fig. 3-11 the polarizer was affixed so that the center of the polarizer was automatically self-aligned to the focusing lens. This configuration allowed tuning of the repetition rate over a larger range. After insertion of the polarizer, the intracavity power was reduced by $\sim 10\,\%$, which resulted in the stable mode-locking results shown in the following.
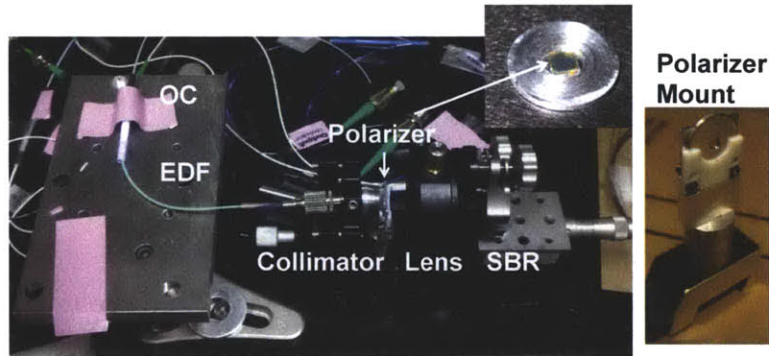
Figure 3-10: Photograph of 625 MHz EDFL. The inset shows the thin-film polarizer with $3\,\text{mm} \times 3\,\text{mm}$ dimensions, glued to a 1/2 inch diameter holder. The custom-machined polarizer mount allows rotation of the polarizer to the desired angle.
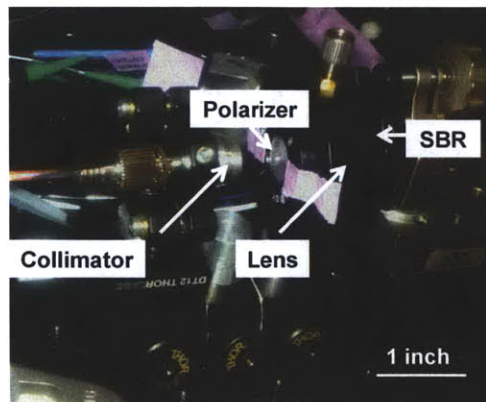
Figure 3-11: Compact mounting of the polarizer in the EDFL cavity.

The modular approach with an Er-doped fiber laser source provided the distinct advantage that the repetition rate, input polarization and pulse duration could be adjusted to best match the operation of the interleaver filters. The pulses were amplified using two isolated stages of Er-doped amplifiers (EDFA), which were optimized in their design for maximum gain and minimum amplified spontaneous emission. The amplifiers incorporated Er-doped normal dispersion gain sections of 55 cm and 48 cm (Liekki Er110-4/125 gain fiber). They were pumped in a counter-propagating scheme with launched pump powers of 500 mW and 400 mW. The spectral characteristics of the first amplifier at pump powers of 500 mW, 370 mW and 270 mW (corresponding to 1100 mA, 800 mA and 600 mA of pump current) are shown in Fig. 3-12 for a cw input power of 840 μW from the tunable laser source that was swept over the wavelength range of interest. By using a cut-back approach for the gain fiber length, a uniform amplification over a broad bandwidth and maximum power around 1560 nm was achieved.

With an external fiber polarization control unit, the input polarization into each interleaver chip was optimized to the preferred waveguide mode (cf. Fig. 3-9 for the set-up). Parts of the system, which were encapsulated in an enclosure in order to reduce the sensitivity to environmental perturbations, are shown in Fig. 3-13. The pump diodes and the second amplifier were placed outside the enclosure. The free-space section in the fiber laser cavity allowed tuning of the laser repetition rate around 625 MHz so that the laser frequency lines could be matched to the interleaver filter response and the device performance could be optimized. Further fine-adjustments to the optical transmission function were made afterwards by thermal tuning of the delay lines.

3.4 Characterization

3.4.1 Optical Characterization

The Er-doped fiber laser could be mode-locked over a range of repetition rates (a 2 mm path length change in air induced a 5 MHz shift), with the region of interest being between 620 MHz and 630 MHz. For the following results, the laser was stably mode-locked at a
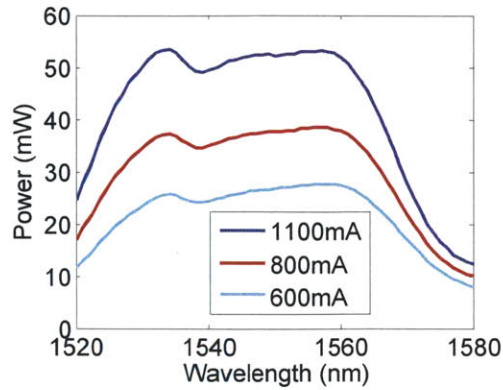
Figure 3-12: Amplification of the first amplifier stage for $840\,\mu W$ of signal power for launched pump powers of $500\,mW$, $370\,mW$ and $270\,mW$ (corresponding to pump currents of $1100\,mA$, $800\,mA$ and $600\,mA$, respectively).

fundamental repetition rate of $624.5\,MHz$, since this repetition rate proved to result in optimized performance. An output power of $4.6\,mW$ was obtained for $420\,mW$ of coupled pump power from two polarization-combined pump diodes. The optical spectrum of the Er-doped fiber laser, shown in Fig. 3-14 (a), featured a 3-dB bandwidth of $6.1\,nm$. For soliton propagation in the form of sech-shaped pulses, this optical bandwidth corresponded to transform limited pulses of $420\,fs$ in duration. The laser output, after passing through a $1550\,nm$ isolator, was amplified in two isolated Er-doped amplifier stages from $3\,mW$ to $82\,mW$ before being coupled into the waveguide chips. In both amplifiers, gain narrowing and spectral shaping due to nonlinearities and self-phase modulation could be observed. This resulted in additional spectral side-lobes, as seen in Fig. 3-14 (a) (dotted gray line). The second amplifier stage limited the optical bandwidth further so that the output spectrum of the interleaver featured only a $\sim 4\,nm$ 3-dB bandwidth, cf. Fig. 3-14 (a) (red line). Nonetheless, pre-amplification was favorable as opposed to post-amplification of the interleaver output pulse train; otherwise the side-band suppression got distorted due to the subsequent four-wave mixing and nonlinear amplification (see Section 3.4.3 for details). The optical modes with a spacing of $\sim 0.08\,nm$ in the interleaver output spectrum, as shown in Fig. 3-14 (b), had only limited contrast due to the $0.1\,nm$ resolution of the optical spectrum analyzer
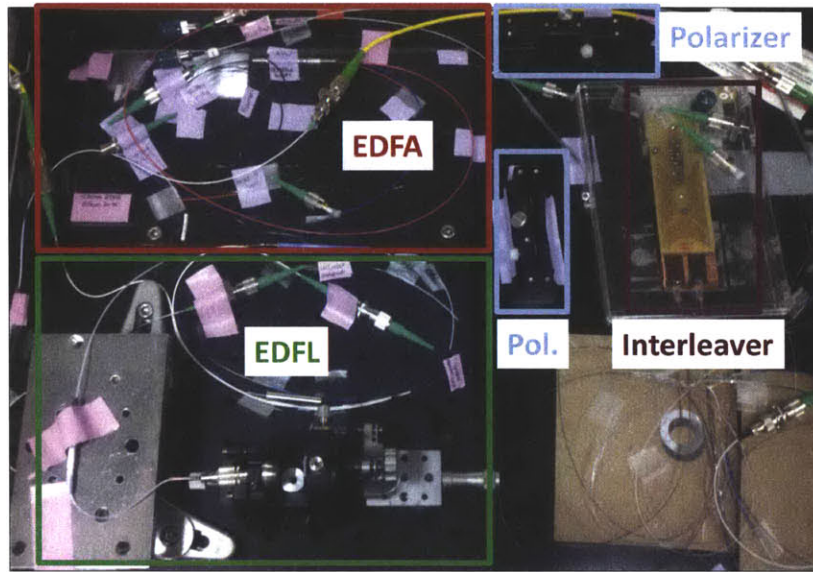
Figure 3-13: Photograph of parts of the interleaver system which are encased in an enclosure (not shown): 625 MHz fiber laser, the first amplifier and the encapsulated interleaver chips. The second amplifier, pump diodes and the thermal tuning set-up were outside the box which served to stabilize the laser against air currents.

used. Though not fully resolved, these optical modes were evidence of the phase-coherence of the 10 GHz output pulse train. The time-domain oscilloscope traces of the laser output in Fig. 3-14 (c) and the two-stage interleaver output at 2.5 GHz in Fig. 3-14 (d) verified the good signal stability. The pre- and post-pulses in Fig. 3-14 (d) could be attributed to detector ringing, and ghost images were likely caused by cable artifacts.

The Ge-doped silica waveguides were low-loss (around 0.01 dB/cm waveguide propagation losses), which resulted in a propagation loss of 0.3 dB for the longest arm in the four-stage interleaver. Interleaver losses of 3 dB due to power division into the two arms were encountered in every stage, resulting in a minimum expected loss of 12 dB for the four-stage interleaver. With standard coupling losses of 1.5 dB between the chip and fiber array, theoretically expected losses for the overall waveguide system amounted to approximately 18 dB. However, the 10 GHz interleaver output signal with $\sim 150\,\mu W$ of output power (for 82 mW input power), indicated that additional losses in the interleaver system were in total
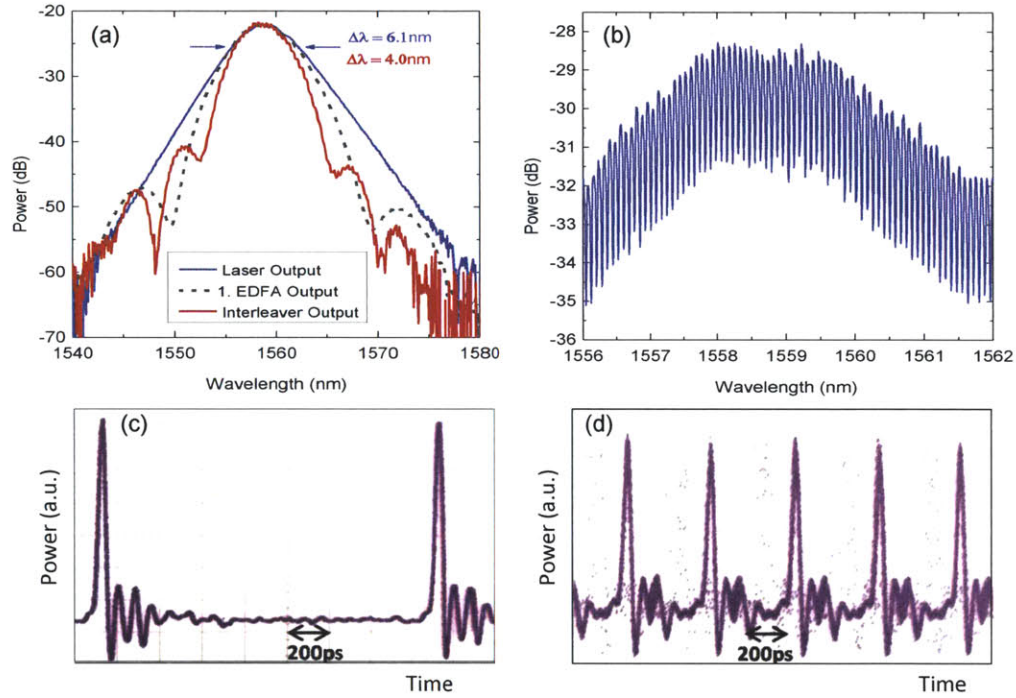
Figure 3-14: (a) Optical spectrum of the laser output with 6.1 nm 3-dB bandwidth (blue line); output after the first Er-doped fiber amplifier (EDFA) (dotted gray line) and output from the 10 GHz interleaver with ~ 4 nm FWHM bandwidth (red line). (b) Optical spectrum of the four-stage interleaver output; the optical modes corresponding to 10 GHz line spacing are barely resolved by the 0.1 nm resolution of the optical spectrum analyzer used. (c) Time-domain oscilloscope trace of the laser output shows pulse train spacing corresponding to ~ 625 MHz repetition rate. (d) Time-domain oscilloscope trace of the two-stage interleaver output at 2.5 GHz.

around 27 dB. Optical time domain reflectometry measurements established the occurrence of high front-end reflections. Thus, these excess losses of 9 dB were partially attributed to high input facet and surface scattering losses, polarization coupling losses, and inherent waveguide losses augmented for pulsed operation in this initial waveguide fabrication run.

3.4.2 Optical Transmission

In order to characterize the interleaver chips and their performance independently from the fiber laser pulses, the optical transmission of each individual interleaver stage was measured with a tunable, continuous wave (cw) laser. That way, the linear chip losses and the expected suppression levels could be determined. A tunable, high precision laser source (TLS, Agilent 81640A, 2 mW output power) was swept with 0.1 pm step size resolution over different wavelength ranges. For each measurement, the input polarization of the TLS into the interleaver and its thermal tuning state were adjusted. In the following, results centered at 1560 nm are presented. For the first interleaver stage from 625 MHz to 1.25 GHz (corresponding to 10 pm of wavelength spacing at 1550 nm), the measured maximum suppression for the optical transmission with thermal tuning was at least 27.3 dB, as shown in Fig. 3-15 (a).
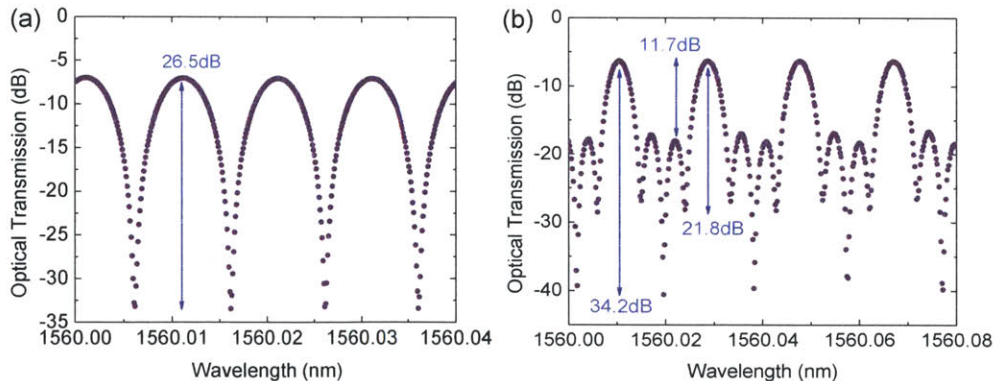
Figure 3-15: Optical transmission measurements of (a) first interleaver stage at 1.25 GHz with thermal tuning and (b) two cascaded interleaver stages at 2.5 GHz.

However, these results were highly polarization sensitive and depended explicitly on the applied heater power due to additionally introduced waveguide birefringence and subsequent polarization conversion with thermal tuning. Given the different degrees of freedom in the system, optimizing the input polarization sufficiently at the filter minima (down to $-35\,\text{dBm}$) so that only one waveguide polarization was guided proved challenging. Thus, by monitoring the power at one input wavelength, the thermal tuning and polarization were adjusted until a state close to a local minimum was found. However, with only one single point for feedback, the global system minimum did not necessarily have to coincide with the optimized state. By taking multiple measurements at different initial polarizations and optimizing the thermal tuning in each wavelength regime, the risk of missing a state with better suppression was reduced, at the expense of increasing the number of measurements.

Simulations of the transmission characteristics indicated that even with small deviations in the coupling ratio, an optical suppression better than $26.5\,\text{dB}$ for the first interleaver stage should be attainable. At the same time, it was inferred from the modeling that a source resolution and stability better than $0.2\,\text{pm}$ was required to measure optical suppression levels beyond $30\,\text{dB}$ for the first interleaver stage, which featured the narrowest dips of all the interleaver stages. Therefore, due to TLS wavelength jitter and superimposed polarization states, the actual depth of the notches in the optical transmission might not have been fully detected. Fig. 3-15 (b) depicts the optical transmission for two interleaver stages without thermal tuning. Maximum suppression levels of $34.2\,\text{dB}$ were recorded. In this particular state, the maximum optical suppression obtained from the first interleaver was measured to be $21.8\,\text{dB}$. In addition, the measurement confirmed high excess losses, also in cw operation, for the waveguide chips.

The impact of small polarization changes on the transmission characteristics is visible in Fig. 3-16, which shows the measured optical transmission curves for the cascaded first two interleaver stages at $2.5\,\text{GHz}$. For slight variations in the input polarization, the shape of the side-lobes was modified and the maximum suppression was reduced by at least $6\,\text{dB}$. Therefore, optimization of the input polarization proved critical to achieve optimized suppression levels.

106
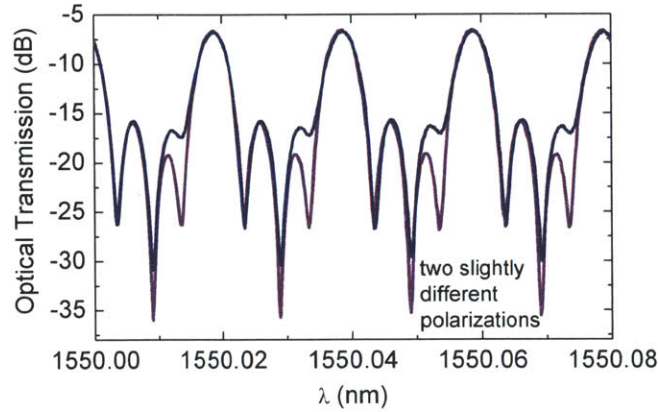
Figure 3-16: Variation in optical transmission plot depending on the input polarization. In this case, only slight adjustments to the polarization state were made in between measurements.

Due to the lack of a polarization discriminating element and because of the multi-mode waveguide character, the interleaver supported both TE and TM polarizations simultaneously, as shown in Fig. 3-17. Hence, for the second interleaver stage, from 1.25 GHz to 2.5 GHz, the cw transmission through the interleaver for each polarization was measured. Either the TE and TM output were selected by collimating the output into a free-space section containing a polarizing beam splitter (PBS). For the given input polarization in Fig. 3-17, which was maximized for the TE output power transmission, the phase shift between the TE and TM modes could be attributed to inherent waveguide birefringence. Thus, from Fig. 3-17, the overall birefringence could be estimated from the slightly different periodicities recorded. For a 20.0 pm free-spectral range (FSR) for the TE mode and 19.9 pm for the TM mode, the respective refractive indices were estimated according to $n = \frac{c}{\Delta f_{TE} L}$. With $n_{TE} = 1.5210$ and $n_{TM} = 1.5286$ a birefringence value $B = |\Delta n| = 7.6 \cdot 10^{-3}$ was derived. Because the resolution of the tunable laser source was limited at 0.1 pm, this birefringence value constituted an upper bound result. This value included modal and geometrical birefringence but no thermally induced contribution. Therefore, polarization optimization through external fiber polarization control units was crucial to match the polarization to the best supported waveguide mode.
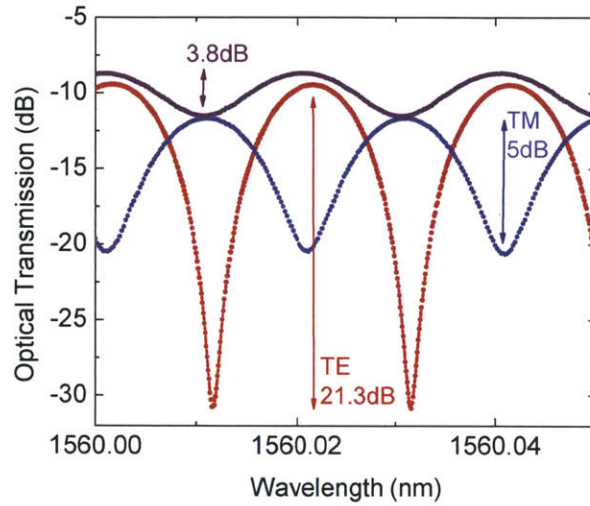
Figure 3-17: Polarization dependence of interleaver (transmission was maximized for TE output) which shows simultaneous propagation of TE and TM modes.
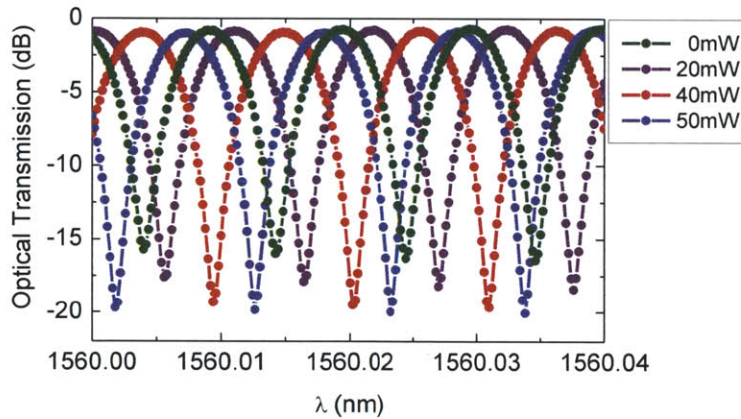
Figure 3-18: Optical transmission for one-stage interleaver (channel 1 to 3) for various heater powers in order to tune the coupling ratio (with heater h5).

By thermal tuning, additional phase shifts were introduced, as illustrated in Fig. 3-18. Here, the applied power to a heater, affecting the coupling ratio (h5), was varied up to 50 mW while the input polarization for the first stage interleaver from 625 MHz to 1.25 GHz remained constant. For applied heater powers of 0 mW, 20 mW, 40 mW and

50 mW, as denoted in Fig. 3-18, the suppression increased from 14.8 dB, to 16.7 dB, 18.4 dB, to a maximum of 18.9 dB, respectively. At the same time, phase shifts were introduced. If a maximum phase shift up to π was assumed as an upper limit (corresponding to $\frac{\lambda}{2\,n} = 500\,nm$), a minimum birefringence due to thermal tuning of $B_{thermal} = \frac{500\,nm}{L_{delay}} = \frac{500\,nm}{16\,cm} = 3.125\,10^{-6}$ could be estimated.

However, from the measurement in Fig. 3-18, only the remaining modulus of the phase shift can be determined. As the phase shifts for the various applied heater powers increased incrementally, it was assumed that no multiples of $2\,\pi$ had to be added to the overall phase.
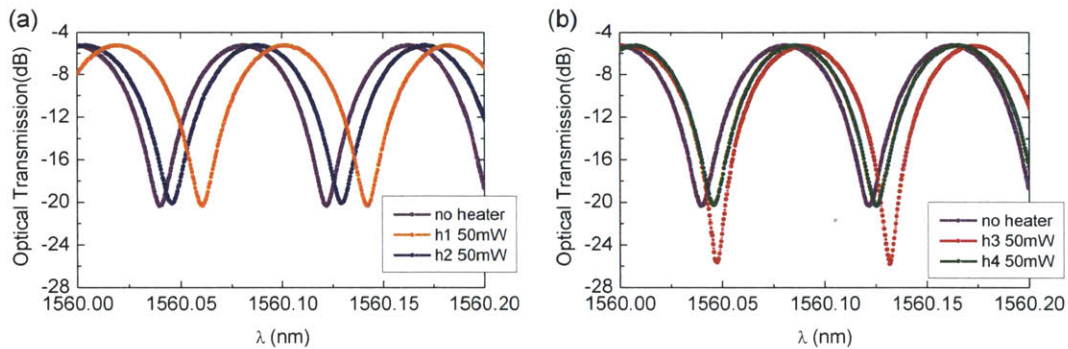
Figure 3-19: The impact of the different heaters on the optical transmission curve is measured in (a) for heaters adjusting the delay line lengths, (b) heaters affecting the coupling ratio.

Fig. 3-19 demonstrates the tuning impact of the two different heaters types: Heaters 1 and 2 tuned the delay line length for the interleaver stage from 1.25 GHz to 2.5 GHz (Channel 4 to 6), compare Fig. 3-7. (Heaters 3 and 4 effectively tune the coupling ratios.) Thus, in Fig. 3-19 (a), the maximum suppression of 15.1 dB hardly changed, but the filter spacing increased from 8.2 pm to 11.3 pm and additional phase shifts were introduced for 50 mW power applied to heater 2. Thermal tuning of heater 3, which adjusted the coupling ratio by modifying the phase shifts in the Mach-Zehnder interferometer stage, increased the suppression ratio to 20.5 dB. This measurement implied that the filter spacing and coupling ratio adjustment were not completely independently tunable from each other, as tuning of heater 3 changed the periodicity to 8.4 pm. Thus, a complex interplay between thermal

tuning and polarization conversion due to birefringence is likely occurring. In particular, for more interleaver stages, tuning of multiple heaters in parallel could lead to stronger birefringence effects. As these measurements were taken to emphasize the heater dynamics, the reported suppression levels do not necessarily reflect the maximum obtainable results.

The wavelength dependent coupling coefficients in the directional couplers determine an optimized wavelength regime for the waveguide interleavers. In Fig. 3-20, the maximum suppression from cw-transmission measurements for the 2-stage interleaver system from 625 MHz to 2.5 GHz is displayed, together with the periodicity of the interleaving filter (20 pm spacing corresponds to 2.5 GHz). For the wavelength regime of interest around 1555 nm to 1565 nm, comparable suppression ratios around 33 dB were measured for the same input polarization state into the interleaver chip. For wavelengths around 1545 nm, the suppression was reduced to 25 dB.
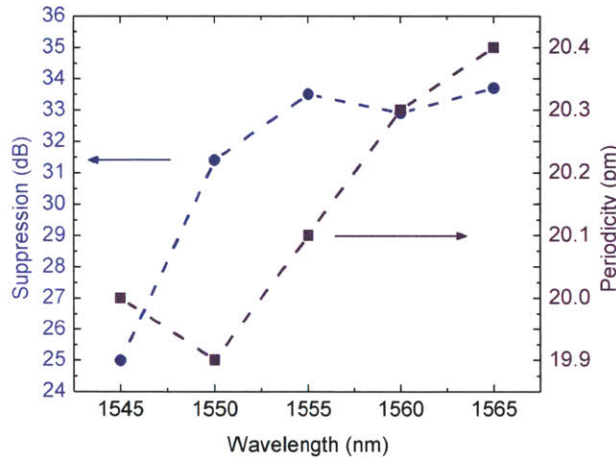
Figure 3-20: Suppression and periodicity of two-stage interleaver.

3.4.3 RF Characterization

The RF spectrum measurement provided an evaluation of the combined fiber and interleaver system, whose performance metrics are of interest for low-noise microwave generation.

In order to optimize the system performance, the position of the EDFAs with respect

to the interleaver output was varied: For the 2-stage interleaver, pre-amplification of the pulses before coupling into the waveguide chip was compared with post-amplification as sketched in Fig. 3-21. The RF performance for the two different configurations is displayed in Fig. 3-22. Due to nonlinear amplification/four-wave mixing in the EDFA after interleaving, more power was distributed to the harmonics with initially less power. The side-mode suppression was thus reduced consistently by 3 dB for all the corresponding lines beyond
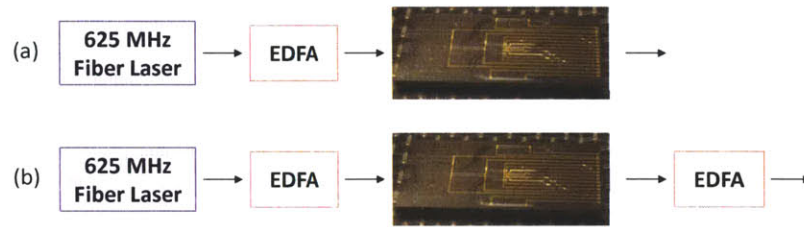
Figure 3-21: Schematic illustrating (a) pre-amplification and (b) post-amplification of interleaver output.
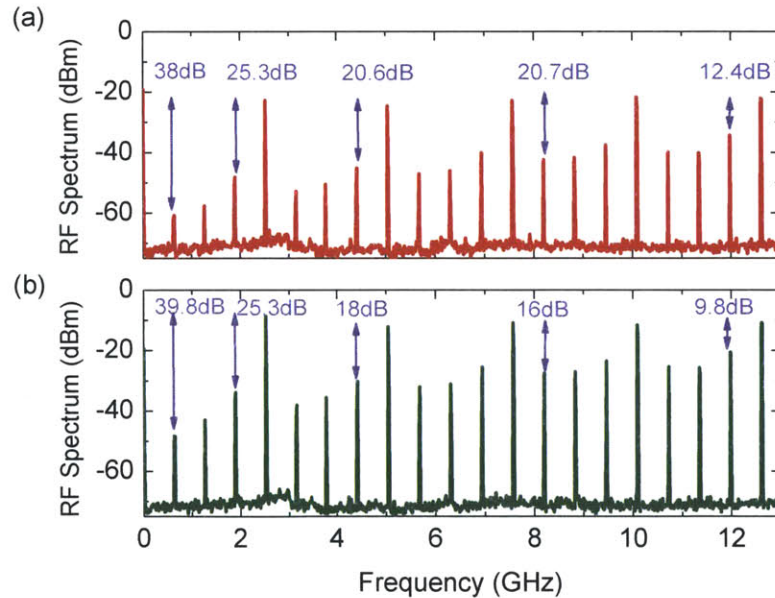
Figure 3-22: Comparison of (a) a pre-amplified 2.5 GHz output pulse train with (b) post-amplified output pulses. The side-mode suppression was consistently reduced by 3 dB for the post-amplified signal.

the initial fundamental frequency interval up to 2.5 GHz for the post-amplified pulse train. In this particular configuration, the post-amplification EDFA was operated at only about one fourth of the usual pump power (pump current of 120 mA). This indicates that for full pumping power this effect could be further enhanced. Thus, to minimize distortions in the suppression of the side-modes, pre-amplification of the pulses in two isolated EDFAs before coupling into the waveguide chips was preferred over amplification in between interleaver stages or post-amplification at the final output.

The RF data, as illustrated in Fig. 3-23, was taken for a fundamental repetition rate of the fiber laser at 624.5 MHz, where the suppression was found to have been maximized. The RF-domain interleaver output at a repetition rate of 2.5 GHz is presented in Fig. 3-23 (a) and Fig. 3-23 (b). Without thermal tuning, the sub-harmonics were suppressed in the RF domain by 14.3 dB for the immediately adjacent side-bands, while the maximum suppression amounted to 22.4 dB. Significant improvement was achieved by thermal tuning, as presented in Fig. 3-23 (b). The maximum suppression increased to 55.8 dB for one line, where the interleaver response and input frequency directly lined up in a transmission minimum. Over the frequency span up to 12 GHz, the side-mode suppression amounted to at least 30.5 dB. In the thermally tuned state, the side-mode suppression decreased with higher harmonics, which can be partially explained by the limiting impact of wavelength dependent coupling coefficient offsets and waveguide dispersion. As the RF signal is given by the sum of the convoluted frequency lines, wavelengths at the edges of the optical spectrum could deteriorate the suppression, if the suppression of the individual lines was not as optimized in those regions. The 2.5 GHz pulse train was then transmitted through the second interleaver chip, which multiplied the repetition rate to 10 GHz. The initial RF suppression around 15.4 dB for the adjacent side-mode, as shown in Fig. 3-23 (c), was significantly enhanced in the thermally tuned system, as demonstrated in Fig. 3-23 (d). Here, a side-band suppression of 31.3 dB was recorded. Due to the low output power from the interleaver chips, the maximum side-mode suppression of 36.3 dB was limited by the detector noise floor. Therefore, the actual maximum suppression may have been greater than the measured value. For these measurements, the RF suppression was maximized by tun-

112
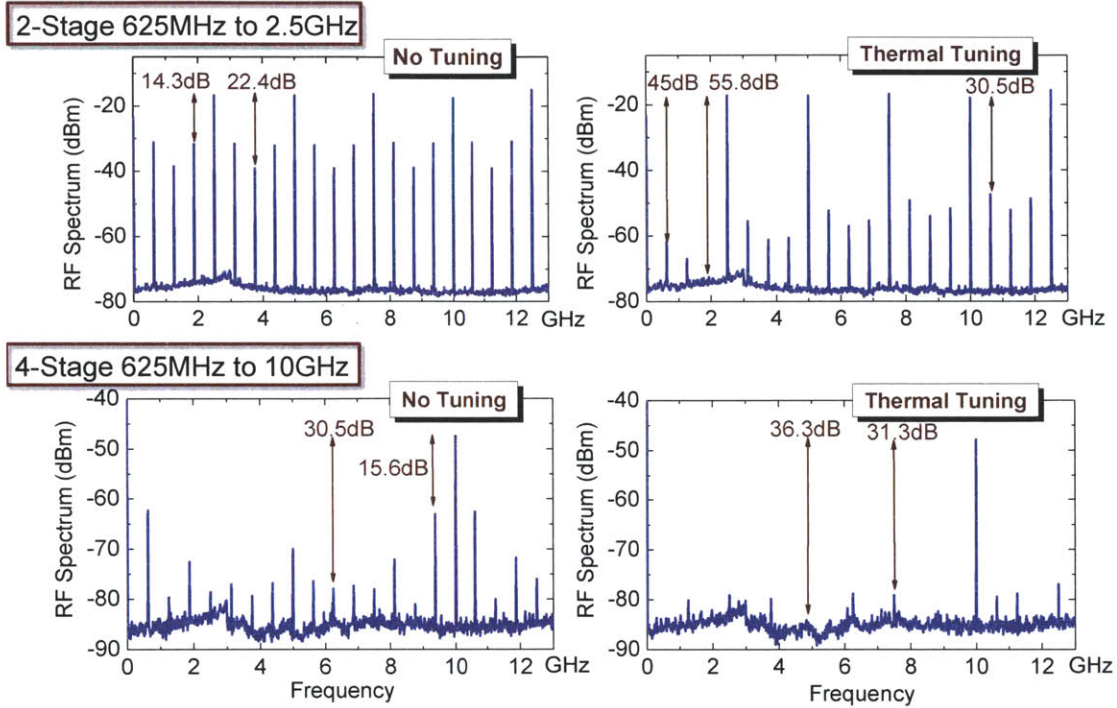
Figure 3-23: RF spectrum: (a) Minimum suppression of 14.3 dB for 2.5 GHz output without thermal tuning. (b) Minimum suppression of 30.5 dB for 2.5 GHz output with thermal tuning. (c) Minimum suppression of 15.6 dB for 10 GHz output without thermal tuning. (d) Minimum suppression of 31.3 dB for 10 GHz output with thermal tuning. All measurements were recorded with a resolution bandwidth of 300 kHz.

ing of the heaters that primarily adjusted the coupling ratio. Thermal tuning of the delay lines mostly influenced the optical suppression of each individual line, as discussed in the following section.

3.4.4 Optical Heterodyne Beat

In order to confirm the phase-coherence of the interleaved pulses and to gain insight into the achievable optical suppression, optical heterodyne beat measurements between the interleaved pulse train and a narrow-linewidth tunable laser source were performed.

An optical heterodyne system, as shown in Fig. 3-24 (a), was employed to determine the optical suppression for the individual optical modes in a frequency comb, which is

in particular of interest for frequency metrology applications: The interleaver output was combined with a single frequency narrow-bandwidth line of a stable tunable laser whose polarization was matched to the interleaver output with an external polarization control unit. The signal was photo-detected by an InGaAs EOT ET-3500F detector. An electronic signal analyzer was the preferred instrument of choice (over a RF power meter) to not only record the amplitude but also the frequency position of the beat notes.

The measured heterodyne optical beat was determined by the respective electric field strengths of the tunable laser source E_{TLS} and the interleaver $E_{TLS} \cdot E_{Int}$. Thus, the detected beat note in the RF spectrum analyzer was proportional to the optical interleaver power and the measured suppression corresponded directly to the optical suppression. As the cw transmission measurements from Section 3.4.2 recorded the transmitted optical power through the interleaver device, both measurements provide an independent evaluation of the optical suppression.

In order to detect the heterodyne beat note, two variations of the measurement set-up were pursued. In a first configuration, the photodetected signal was low-pass filtered with a cut-off frequency at 450 MHz, as shown in Fig. 3-24 (a). The frequency line sketches illustrate how for different wavelengths from the tunable laser source (as denoted by different colors), different optical suppression values are measured. During each measurement, the beat notes with two neighboring optical lines were captured, if the TLS wavelength output was positioned accordingly. For the first interleaver stage, shown in Fig. 3-24 (b), a optical suppression of 31 dB was recorded at 1560 nm. However, even though the measurement sensitivity of the instrument was optimized to the signal input power, the lower optical beat note disappeared in the noise floor.

To obtain the optical suppression for subsequent lines and examine two or more cascaded interleavers, multiple measurements were made while the tunable laser wavelength source was swept over the desired wavelength range. In Fig. 3-24 (c), three such optical heterodyne measurements for two cascaded interleaver stages were superimposed. The measurements were each taken with 5 pm spacing (corresponding to the initial ~ 625 MHz repetition rate) so that directly neighboring lines were resolved. The sketch of the frequency lines next to
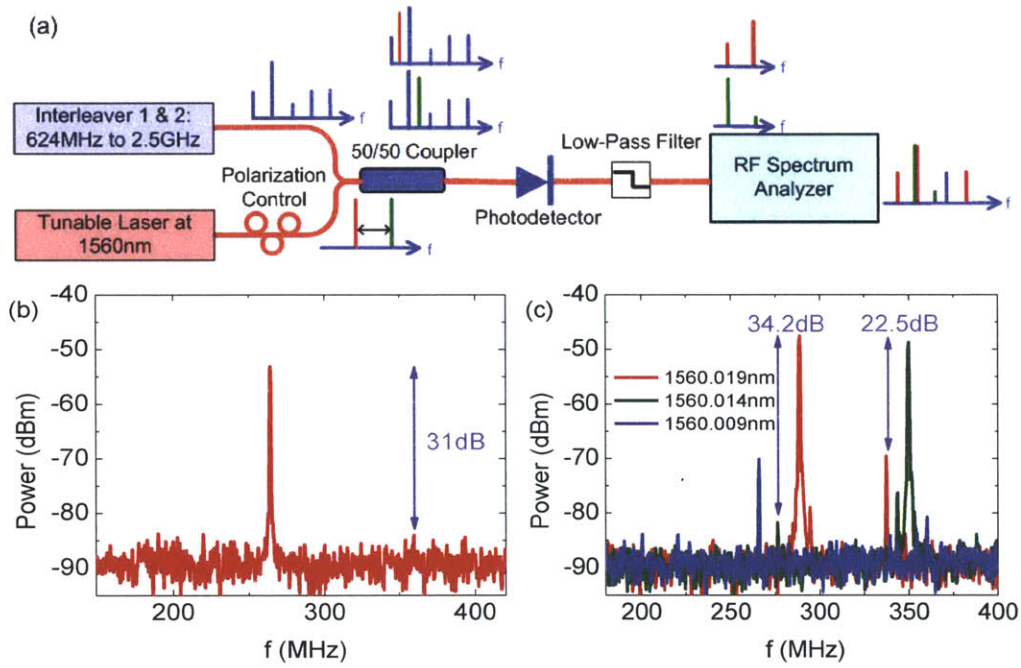
Figure 3-24: (a) Measurement set-up to detect the optical heterodyne beat for two cascaded interleaver stages. Different colors (red, green) indicate two different wavelengths of the tunable laser. (b) Measured optical suppression of 31 dB at 1560 nm for 1.25 GHz interleaver. (c) Optical suppression of 34.2 dB around 1560 nm for 2.5 GHz interleaver. Three measurements at different wavelengths are combined in one plot to obtain information about the suppression over one free spectral range. The sketch of the frequency lines next to the RF spectrum analyzer indicates the corresponding ordering of the frequency lines. All measurements featured a resolution bandwidth of 300 kHz.
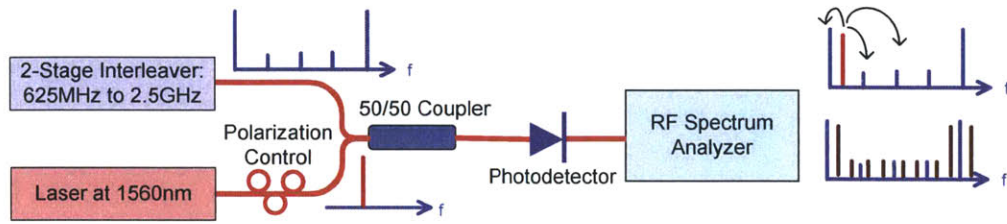
Figure 3-25: Schematic of measurement set-up to record the optical suppression of multiple lines simultaneously.

the RF spectrum analyzer Fig. 3-24 (a) indicates the corresponding ordering of the optical lines. The best suppression amounted to 34.2 dB for the immediate adjacent side-mode, whereas the other two optical lines were suppressed by 22.5 dB. With the chosen wavelength spacings, the optical heterodyne beat corresponding to the previous measurement was recorded again. As identical amplitudes for the same beat note were detected, the consistency of the measurements was confirmed over the recorded interval. However, due to the number of measurements required, this method was only suitable for an interleaver analysis with few stages.

In order to maximize the optical suppression information that was collected within one measurement, a second measurement configuration with a wide-band frequency approach (similar to the configuration in Fig. 3-24(a) without the low-pass filter) was pursued, see Fig. 3-25. In this set-up, the beat notes between the single wavelength laser and all optical interleaver lines were detected simultaneously. Results for the two-stage interleaver at 2.5 GHz are shown in Fig. 3-26. The obtained suppression ratio varied between 25.2 dB and 29.9 dB. In this particular state, the system was optimized by tuning the coupler and delay line heaters for a symmetric suppression of the side-modes. This more uniform power distribution was particularly attractive for astrocomb calibrations.

During each measurement the harmonics of the repetition rate lines (plotted in gray in Fig. 3-26) were detected together with the optical heterodyne beats (highlighted in red). As the repetition rate signal and its harmonics were given by a convolution of all optical lines, they possessed significantly more power (up to 25 dBm). Thus, the sensitivity towards the
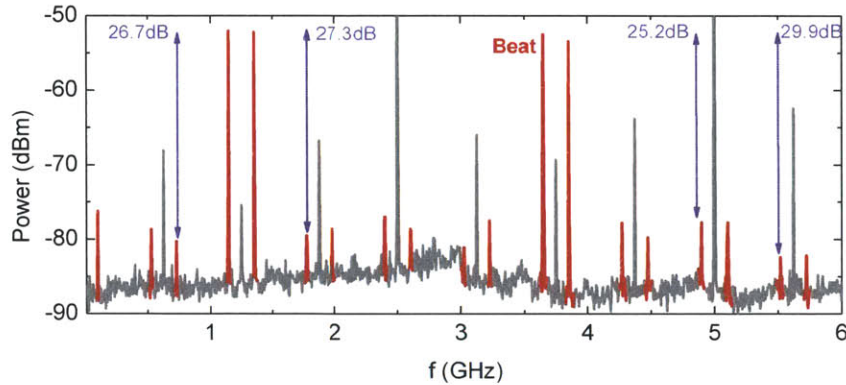
Figure 3-26: Heterodyne beat measurement for thermally tuned 2.5 GHz interleaver. The optical beat notes are denoted in red, the gray lines depict multiples of the initial repetition rate.

low-power optical beat notes had to be reduced so that the higher power RF lines did not to saturate the detector. This can partially explain the difference in maximum side-mode suppression of 29.9 dB as compared to the first measurement result of 34.2 dB. In addition, each state was highly dependent on the thermal tuning and input polarization, as discussed previously. The good optical suppression over the measurement interval indicated that after thermal tuning, the delay line lengths were well matched to the frequency comb lines, as otherwise, the suppression would have significantly worsened with higher harmonics.

The optical suppression for subsequent stages could be evaluated with this measurement set-up. When this measurement technique was applied to the 10 GHz interleaver stage, suppression levels around 31 dB were recorded for individual lines.

3.5 Discussion

3.5.1 Drift of Free-Running Laser System

All characterizations in this chapter were performed with a free-running laser. The laser was isolated from air current and environmental perturbations, by placing it in an enclosed environment by itself and the overall set-up was encased in an additional box. In this configuration, the repetition rate line was measured to fluctuate between 630.784,650 MHz

and 630.784,425 MHz (resolution bandwidth of 10 Hz) over a time interval of 10 minutes, corresponding to a ~ 225 Hz relative drift, as shown in Fig. 3-27. This corresponded to a 68.5 MHz drift of the optical line. This value was considered small enough so that for the duration of the measurement stable frequency lines could be assumed, because carrier-envelope drifts were expected to be even smaller than repetition rate drifts. The optical comb line of the mode-locked laser itself varied around 50 MHz over a time span of four minutes.

However, drift from the tunable laser source was assumed to lead to slightly increased deviations. Without any isolation from the environment (for an open box cover) the frequency jitter increased by at least a factor of 5 to 280 MHz, as measured over a time span of 3 minutes. Thus, with a repetition rate stabilized source (or with a fully stabilized frequency comb), the frequency fluctuations are expected to be reduced so that the measured optical side-mode suppression could be improved further.
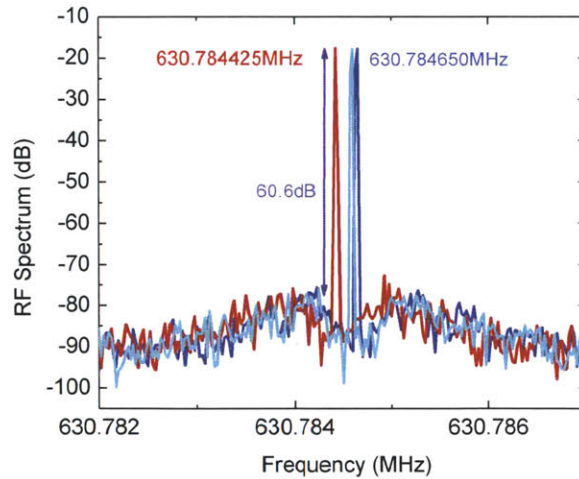
Figure 3-27: Drift of the free-running laser repetition rate by ~ 225 Hz over 10 minutes.

3.5.2 Double-Passing of Interleaver

Throughout this chapter, the suppression of each individual interleaver stage was found to be limited by dispersion and the degree of compensation for fabrication tolerances. To

improve the side-mode suppression, double-passing the same interleaver structure (cf. [104]) was studied, as illustrated in Fig. 3-28: The fiber-coupled output of the first interleaver stage was butt-coupled to a silver mirror, which reflected the interleaved pulse train back into the interleaver. This pulse train then propagated a second time through the identical interleaver stage in the reverse direction, thus yielding ideally twice the single-stage suppression. A 50-50 coupler (with an isolator at the input port) or a fiber circulator separated the input from the output pulse train.

The modeled cw-transmission for the first interleaver stage from 625 MHz to 1.25 GHz (with ideal coupling coefficients and -5 fs^2/mm of waveguide dispersion) is plotted in Fig. 3-29. The suppression is doubled, e.g. as visible in the troughs from 63.4 dB to 122.9 dB. In addition, for the double-passed interleaver the troughs are wider so that suppression levels higher than 60 dB are attained over a larger bandwidth of 36 MHz, as compared to the single-pass transmission.
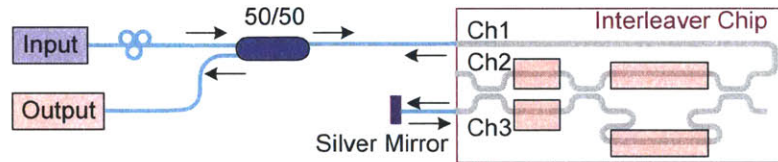
Figure 3-28: The interleaver is double-passed by reflecting one output back into the chip with a silver mirror. The 50-50 coupler was replaced by a circulator for some measurements.

RF measurements with and without thermal tuning of the coupling ratio heaters for the first interleaver stage are plotted in Fig. 3-30 for the case of (a) single-passing and (b) double-passing the interleaver. While the suppression for the single-stage interleaver amounted to 31 dB, the double-passed interleaver featured a suppression of at least 36 dB, which was limited by the noise floor. The RF side-modes in Fig. 3-30 (b) appeared to have been amplitude-modulated by ~ 5 dB magnitude (without thermal tuning). This effect got enhanced in the thermally tuned case, with at least 20 dB strength. Previously, in Fig. 3-2 (b), offsets between the input frequencies and the filter response (due to dispersion and/or delay line length offsets) resulted in a periodic amplitude modulation of the lower side-mode,
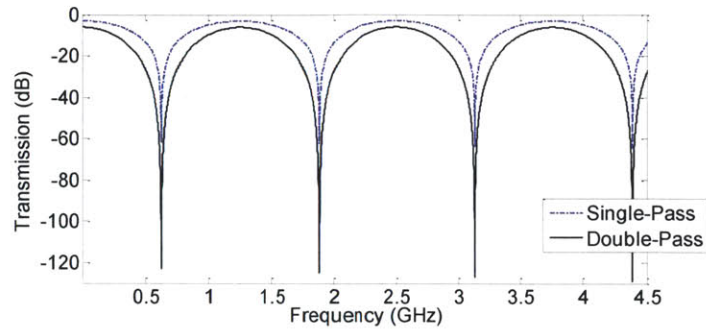
Figure 3-29: Modeling of single-passing and double-passing the same interleaver stage from 625 MHz to 1.25 GHz, including waveguide dispersion and assuming ideal coupling ratios.

however, over a much larger wavelength scale. In double-passing the same interleaver, this limiting effect seemed enhanced: Simulations of the double-passed interleaver with small delay line length offsets of 0.01λ and 0.03λ in Fig. 3-31 indicated that such offsets could induce periodic amplitude modulations of the peaks and troughs in the interleaver response, on the order of ~ 5 GHz.
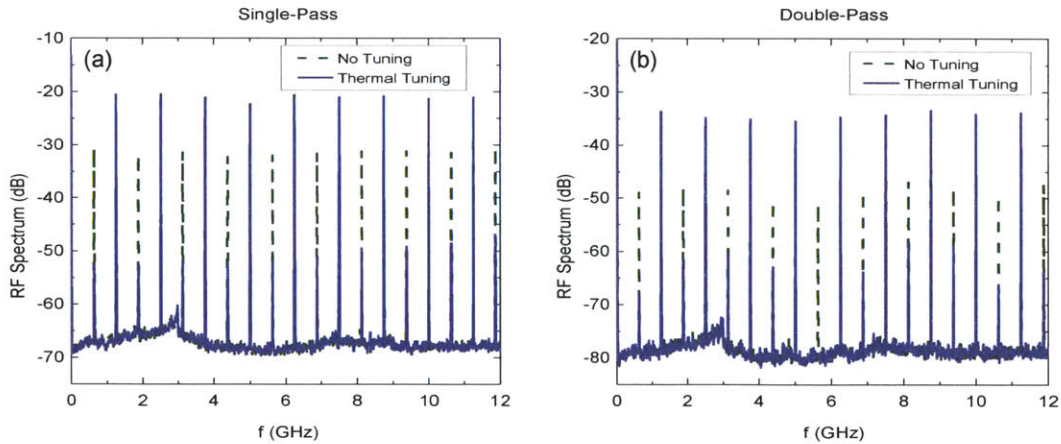
Figure 3-30: Single and double passing through the first interleaver stage with and without thermal tuning.

However, since the RF trace consists of a convolution of all the optical lines across the spectral bandwidth and phase offsets can add/decrease the contributions to the individual

RF lines, this behavior does not directly correlate with the optical suppression. Thus, the optical suppression was studied in more detail. In Fig. 3-32 (a), the optical beat with a cw laser at 1560 nm for the double-passed 1.25 GHz stage indicated that the suppression amounted to at least 25 dB. The heterodyne beat measurement notes were marked in blue, while the harmonics of the repetition rate were denoted in gray. However, for an accurate measurement, a better detection resolution was required to really evaluate by how much the optical suppression of the double-pass improved compared to the single-pass through the interleaver.

As the first interleaver stage proved to contribute the largest accumulated waveguide dispersion and losses in the cascaded interleaver stage, a 1.25 GHz fiber laser was built. With this input source, one could directly couple into the second interleaver stage. For this purpose, a free-space, repetition rate tunable EDFL and a butt-coupled laser was developed, as described in Section 2.4.2. Since the butt-coupled laser provided higher output power, this oscillator was used as the preferred input source in order to study the double-passing effect on the 2.5 GHz interleaver stage in more detail. Preliminary optical heterodyne beat measurement results in Fig. 3-32 imply that suppression levels higher than 31.2 dB could be attained. As some of the integrated heaters were not functioning and one of the output channels suddenly malfunctioned, more detailed studies require wire-bonding of another interleaver chip. The simulations, combined with the preliminary measurements on double-passing interleaver stages, indicate that this is a promising pathway to generate higher side-mode suppression.
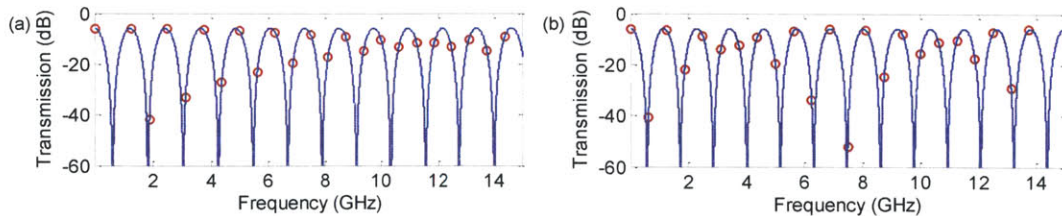
Figure 3-31: Simulations of optical transmission for double-passing the first interleaver with (a) delay line length offset of 0.01 λ and (b) 0.03 λ.
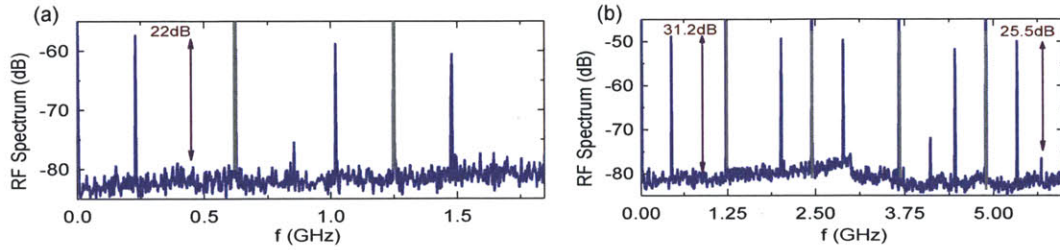
Figure 3-32: Optical heterodyne beat (a) at 1560 nm for double-passed 1.25 GHz interleaver and (b) at 1553 nm for double-passed 2.5 GHz interleaver. The gray lines mark multiples of the repetition rate.

3.5.3 Summary and Future Work

Different performance metrics for thermally tunable planar waveguide interleavers were analyzed. The optical transmission measurements confirmed the expected device performance and provided insight into how well the fabrication met the target design. It was extremely beneficial to have such a verification that was independent of the fiber oscillator operation and any challenges that came from adding complexity to the system. In addition, these optical suppression values corresponded directly to those obtained with the optical hetero-dyne measurement. While the maximum optical cw transmission suppression for the first interleaver stage amounted to 26.5 dB, the heterodyne beat measurement inferred a value of at least 31 dB (for complete summary, cf. Table 3.2). As discussed already in Section 3.4.2, for the first interleaver stage with narrow minima, the full depth of the notches might not be fully detected due to the limited wavelength resolution and precision of the TLS. The measurement might have further been limited by the single power feedback point that was provided to optimize the input polarization and thermal tuning state. Thus, the cw transmission did not necessarily indicate the maximum suppression levels achievable.

Although remaining slight offsets between the repetition rate line and the filter peri-odicity could have influenced the recorded suppression levels attained from the heterodyne measurements, the detection was limited by the low optical power in each line. However, the optical beat measurements resulted in improved suppression levels for the first inter-leaver stage. The variation between the two measurements could additionally be explained

by different thermally tuned states. For subsequent stages at GHz operating frequencies, the maximum measured optical suppression for the two cascaded interleaver stages from the transmission and heterodyne beat measurements both independently verified equivalent suppression levels. The maximum suppression was reported in one case as 34.2 dB, whereas, for another operating point, the optical suppression was measured to be 29.9 dB. This underlined further how critical the thermal tuning was and how small offsets in the delay lines could affect the optical suppression levels significantly. These measurement results are summarized in Table 3.2.

The signal-to-noise ratio in the optical heterodyne beat measurements was fairly low: The optical signal power usually varied between $150\,\mu$W and 2 mW. This power was spread over the whole optical bandwidth of ~ 30 nm or 3.75 THz, which corresponded to around 6000 optical lines. Thus, with ~ 25 nW of power in each optical line, the detection was limited by the noise floor. In order to increase the power in each optical line, a slice of the output spectrum can be filtered optically first. This signal of only a few nm bandwidth could then be optically amplified. Although the nonlinear post-amplification might introduce some distortions, such a measurement set-up is expected to result in a stronger beat detection. With higher signal-to-noise performance, more accurate values for the actual optical suppression should be received. By tilting the filter or using bandpass filters that are centered at different parts of the spectrum, the optical suppression for different wavelength regions can be explored as well.

The measured harmonics of the repetition rate in the RF spectrum were created by a convolution of all optical frequency lines in the frequency comb; including the lower power

Characterization Method	1-Stage Interleaver Max. Suppression	2-Stage Interleaver	
		Max. Suppression	Min. Suppression
Opt. Transmission	26.5 dB	34.2 dB	21.8 dB
Opt. Beat	31 dB	34.2 dB (29.9 dB)	22.5 dB (25.2 dB)
RF Measurement	31 dB	55 dB	30.5 dB

Table 3.2: Summary of measured suppression levels, depending on different characterization mechanism.

wings of the spectrum (± 15 nm from 1558 nm) that did not necessarily have an optimized side-mode suppression. The coupling coefficients deviated more strongly from the ideal splitting ratio in this regime, since the directional couplers were wavelength dependent and dispersion could have limited the suppression of individual lines. In addition, phase effects could cancel or enhance certain harmonics of the repetition rate, and the delay line lengths were not necessarily matched well over the whole wavelength spectrum. Therefore, it was crucial to measure the optical and RF suppressions individually, since it is challenging to establish a direct and general relation between the optical suppression and the RF suppression.

The time delay accumulated in the longer waveguide arms, waveguide dispersion and delay line offsets, which had to be controlled to within a small fraction of the wavelength, limited the side-mode suppression over a wider bandwidth range. Minimizing the waveguide dispersion or creating dispersion compensating designs could reduce this impact. In addition, scaling the fundamental repetition rate of the fiber oscillator to higher input repetition rates allows shortening the delay line lengths in the first interleaver. This in turn reduces the accumulated dispersion and improves the accuracy of the fabricated delay line length. The described 1.25 GHz butt-coupled and free-space lasers (cf. Section 2.4.2) were designed for such a demonstration, and preliminary results were collected. As discussed before, multiple stages of identical interleavers can be cascaded or the same device can be double-passed in order to obtain better overall suppression levels.

It was already mentioned that, for a first demonstration of this technology, a free-running fiber laser source was used. Since the laser source was well isolated, the observed repetition rate drifts were below 0.3 kHz over a time span of 10 minutes and fluctuations in the carrier-envelope phase shift were expected to have been even smaller. Therefore, these drifts were not considered to have imposed severe limitations on the measurement results.

In addition, current efforts are underway to optimize the interleaver design and the fabrication so that losses in the interleavers can be minimized. As the excess losses in these waveguide interleavers originated mostly from the high front-end reflections of the waveguide interleaver chip, improving the coupling from the fiber array to the chip can potentially

124

reduce the losses. Polarization conversion seemed to have significantly contributed to losses, which can be reduced by integrating design options that guide only a single polarization or that feature a single-mode waveguide design.

Therefore, a re-design of new interleaver chips is currently being pursued. Y-splitters can reduce the fabrication sensitivity of the current directional couplers. In addition, designs that cascade two identical interleaver stages are being considered, to improve the suppression. By starting with a higher repetition rate input source, limiting effects of dispersion are expected to impair performance to a lesser degree. Thus, this second generation design poses a promising approach to demonstrate even better performance metrics from integrated waveguide interleaver chips.

3.6 Conclusion

A compact system, consisting of a repetition rate tunable fiber laser combined with four interleaver stages to multiply the repetition rate by a factor of 16, from 625 MHz to 10 GHz, was demonstrated. An amplified femtosecond pulse train was coupled from the fiber oscillator source into interleavers that were defined in planar waveguide geometry. The optical and RF side-mode suppression of the frequency lines was analyzed. The measured RF suppression of 30 dB up to 12 GHz was partially limited by waveguide dispersion and delay line length offsets. In the optical domain, suppression levels of at least around 30 dB were confirmed by heterodyne beat measurements. Thus, the promising potential of thermally tunable interleavers in planar waveguide geometry for coherent pulse interleaving for applications in astrocomb calibration, frequency metrology and low-noise microwave signal generation was presented. With more optical power available in each line, a fully stabilized laser source and reduced interleaver losses, even better performance metrics can be achieved for generating wide-spaced frequency combs.

Chapter 4

Erbium-doped Waveguide Lasers

Waveguide lasers on a silica platform are attractive femtosecond sources due to high achievable Er-doping concentration, compactness, robustness, ease of integration, and mass-producibility. Progress in planar waveguide (WG) technology has previously enabled mode-locked Er-doped WG lasers with repetition rates of 400 MHz [105] and 500 MHz [100]. Based on these successful demonstration of mode-locked waveguide chips, the goal of this research is to scale chip waveguide lasers to higher repetition rates, while optimizing performance.

4.1   Introduction

Although compact and robust femtosecond fiber laser systems have been developed, commercially available fiber systems are, in general, limited to repetition rates of 250 MHz or lower. While solid-state counterparts can be scaled more easily to higher repetition rates due to higher extracted gain, the cavities incorporate free-space sections, which make them sensitive to alignment and environmental perturbations. As any fiber or solid-state femtosecond laser is custom-designed and individually assembled, these lasers come at a high price point and usually require expert knowledge for maintenance.

Waveguide femtosecond lasers address these limitations and offer compact set-ups with reduced footprints, robust performance metrics, ease of integration, and low costs due to scalability of fabrication. Thus, waveguide lasers on a silica platform exhibit a promi-

sing potential to enable wider adoption of femtosecond technologies and to offer integrated systems with added functionalities in an on-chip platform.

With the development of Er-doped glass waveguides as gain media (for an overview of fabrication details, the reader is referred to [106]), first attempts at mode-locked waveguide laser sources with pico-second pulse durations were undertaken. Actively mode-locked glass waveguide lasers at harmonics of the fundamental repetition rate implied that low timing jitters around 21 fs can be supported in waveguide chip systems [107]. Passively mode-locked systems, relying on free-space coupling to saturable absorbers, were demonstrated with Er-Yb co-doped waveguides at repetition rates up to 1 GHz. However, these systems produced ps-pulses, e.g., with between 4.1 ps and 6 ps pulse duration [108, 109, 110] or 9.8 ps pulses at a repetition rate of 100 MHz [111]. In fiber-coupled femtosecond-written waveguides, 1.6 ps pulse trains at a repetition rate of 16.7 MHz were attained by utilizing a carbon-nanotube saturable absorber [112]. In a similar configuration with a femtosecond-written Er-doped bismuthate waveguide, mode-locking resulted in 320 fs pulse durations at a 40 MHz repetition rate [113]. By employing nonlinear polarization rotation in an extended free-space cavity with waveplates, femtosecond operation with 116 fs pulses at 130 MHz was achieved [114]. However, all these cavities relied on free-space coupled optical components, externally to the chip, to support mode-locking. Thus, while these lasers benefited from higher gain due in the waveguide, they did not take full advantage of the potential for highly integrated waveguide lasers.

Hyunil Byun *et al.* first demonstrated compact femtosecond waveguide lasers, without any external free-space cavity section [100, 105]. In Er-doped glass waveguides (for details on the technology, the reader is referred to [115]), 440 fs pulses at 394 MHz with 30 pJ of intracavity pulse energy (for an estimated 16 mW of intracavity power) were attained. The integrated timing jitter was measured at 24 fs [10 kHz to 20 MHz]. In another waveguide device, the pulse durations were further shortened to 285 fs at 500 MHz for 10 pJ of intracavity pulse energy (cf. [116]).

128

4.2 Fabrication Details

The silicon platform features well-developed fabrication processes and an inherent insulating silicon oxide. For this research, a silicon wafer provided the base substrate for the laser fabrication. A silicon dioxide layer served as a lower cladding layer that separated the mode from the high-refractive-index silicon substrate. Rectangular waveguides were designed to guide the mode in their higher refractive index.

The active gain section consisted of RF sputtered erbium-doped alumina-silicate glass, which provided a better solubility for Er ions than fused silica. Thus, higher Er-doping concentrations could be deposited before cluster formation and quenching limited the number of active Er ions in the host material. For the passive waveguide sections, fused silica glass layers were doped either with germanium (Ge) or phosphorus (P) ions to provide waveguide cores with 1.5 % and 0.75 % index contrast, respectively. The previously demonstrated waveguide structures [105, 100] were based on P-doped glass, since this technology had been optimized to integrate passive and active waveguide sections on one chip. For Ge-doped waveguides, the higher index contrast allowed fabrication of more compact waveguide structures with a smaller minimum bending radius to support single mode propagation (> 1 - 2 mm compared to > 6-7 mm). The core section of the waveguide was defined by standard lithography and $10 \, \mu$m of SiO_2 was deposited with Low Pressure Chemical Vapor Deposition (LPCVD) to form the upper cladding layer. The fabrication of the waveguide chips was performed by CyOptics, Inc., in New Plainfield, New Jersey.

In order to combine undoped waveguide regions with doped waveguides in the same layer, a proprietary mode-converter transitioned between the regions. At the same time, the mode-converter tapered the mode in both vertical and horizontal directions to $\sim 7 \, \mu \times 7 \, \mu$m at the input and output of the waveguides. This facilitated coupling to single-mode fiber and estimated losses for the mode-converter amounted to 0.15 dB.

The geometrical waveguide dimensions were confirmed by examining the waveguide facets by SEM (Scanning Electron Microscopy), as shown in Fig. 4-1. Fig. 4-1 (a) depicts the coupling cross-section at the input (and output) of the WG chip. The lateral waveguide
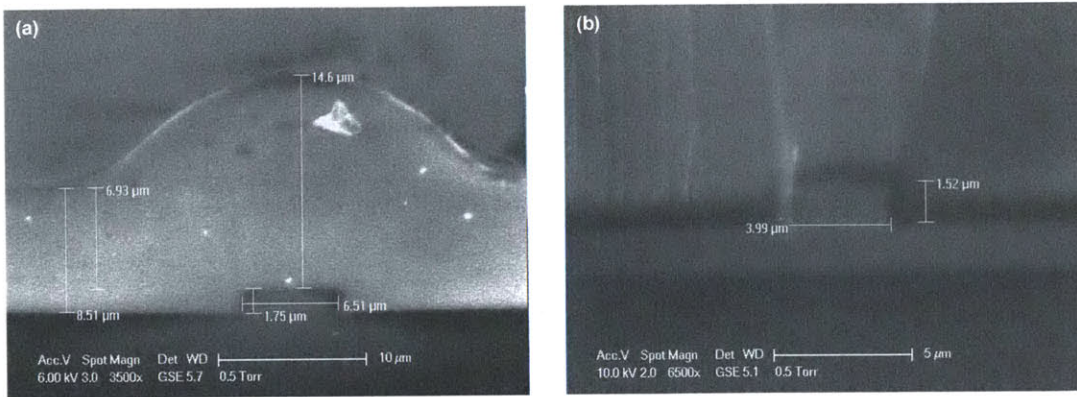
Figure 4-1: SEM characterization of (a) the coupling cross-section at the input and output of the WG chip. Tapering to $\sim 7\,\mu$m x $7\,\mu$m is clearly defined in the lateral direction through waveguide tapering. (b) Cross-section of the Er-doped gain WG section, which confirms dimensions of 1.52 x $4\,\mu$m.

dimensions of $\sim 6.5\,\mu$m confirm the tapering of the waveguide to the specified dimensions of ~ 7 x $7\,\mu$m, with a $10\,\mu$m SiO_2 cladding layer on top. As the measurements were performed on the actual sample (which had some dust speckles on the surface), the onset of surface charging effects were visible. Coating the samples can enhance the resolution and measurement contrast of the SEM analysis. Fig. 4-1 (b) displays the cross-section of the Er-doped WG, which confirms the designed waveguide dimensions of $1.52\,\mu$m x $4\,\mu$m. The deposited SiO_2 lower cladding layer on top of the silicon wafer is clearly visible in Fig. 4-1 (b). The structured lines at the side of the image can be attributed to the cleaved interface.

4.3   Waveguide Chip Design

In order to obtain repetition rates in the GHz regime directly from a waveguide chip, the length of the demonstrated WG lasers at repetition rates of 400 MHz and 500 MHz had to be reduced. The previously incorporated passive waveguides, which compensated in larger WG dimensions for the normal gain WG dispersion, were therefore eliminated. That way, gain sections of the same length as for the 400 MHz WG laser provided comparable amplification while the necessary dispersion compensation for soliton mode-locking was moved off-chip.
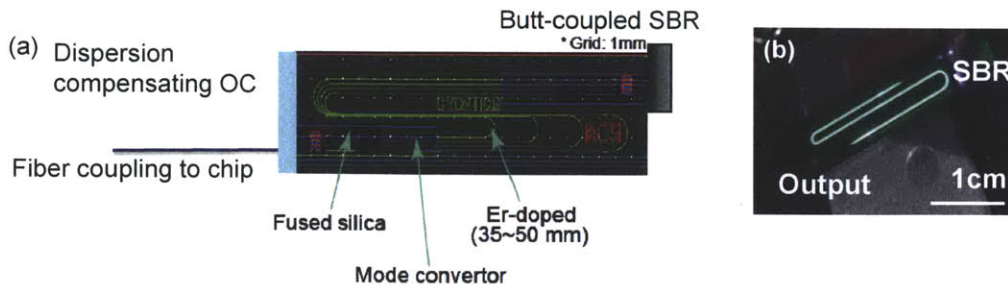
Figure 4-2: (a) Schematic of final WG chip with waveguide layout, courtesy of CyOptics. (b) Photograph of mounted WG chip with the green fluorescence in the Er-doped gain WG section.

This led to a new laser waveguide design that contained only short sections of erbium-doped waveguides. Each chip incorporated four different gain sections of 35 mm, 40 mm, 45 mm and 50 mm length, as depicted in the waveguide layout in Fig. 4-2 (a). Mode converters (of 5.5 mm length on each side of the Er-gain section) connected the Er-doped WG to the tapers at the facets of the chip. For dispersion compensation, this work used a thin-film output coupler, thin-film coating that was deposited on the fiber-waveguide interface to provide the desired anomalous dispersion, as shown in the waveguide schematic in Fig. 4-2 (a). A photograph of the actual lab set-up for the WG chip is presented in Fig. 4-2 (b).

4.4 Waveguide Characterization

In the following, different parameter values of importance for stable mode-locked operation were characterized, consisting of available intracavity power, group delay dispersion and single-mode propagation in the WG.

4.4.1 cw Intracavity Power

In a first fabrication run, chips with gain waveguides width of $4\,\mu$m and height of $1.2\,\mu$m were fabricated. They were characterized in terms of available intracavity cw-power and overall dispersion to evaluate whether soliton mode-locking could be supported. The available intracavity power was determined by butt-coupling the chip between a silver mirror on one
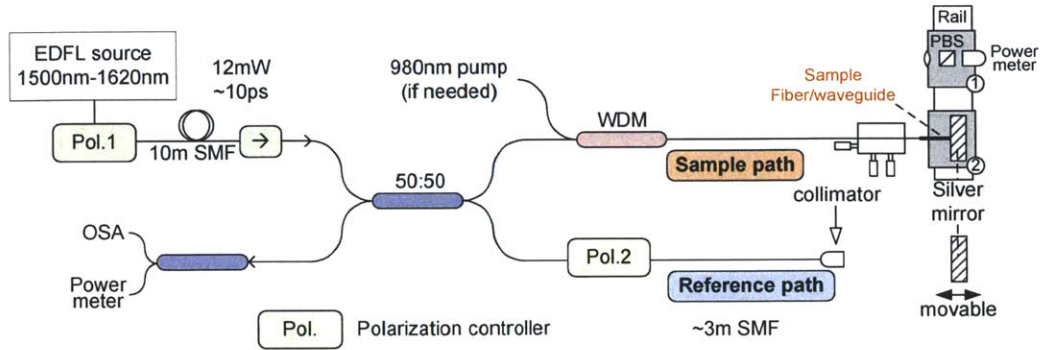
Figure 4-3: Schematic of spectrally resolved white-light interferometer [116].

end and an output coupler/partial reflector (PR1-1550-90-0525, CVI lasers) on the other end. The pump was focused through the partial reflector with an aspheric lens through free-space into the chip. The output was collected after a dichroic beam-splitter to filter out any unabsorbed pump light from the desired signal. Different output coupling ratios were tested to evaluate what loss can be introduced to optimize the intracavity lasing. For an output coupling ratio of $\sim 7\%$, a maximum of $50\,\mathrm{mW}$ of intracavity power was measured, resulting in sufficient intracavity power to facilitate mode-locking (cf. [116]).

4.4.2 Dispersion Measurement Set-Up

A common technique that is used to determine the group delay dispersion, e.g., in waveguide chips and other fiber-coupled devices, consists of white-light interferometry measurements. A home-built white-light dispersion measurement set-up, based on a spectrally resolved Michelson interferometer [117, 116] that was initially developed by Hyunil Byun, was employed to measure the waveguide group delay dispersion.

The dispersion measurement set-up is depicted in Fig. 4-3. The $12\,\mathrm{mW}$ output of a stretched pulsed, erbium-doped fiber laser was broadened in $\sim 10\,\mathrm{m}$ of SMF-28e. This source provided pulse durations of $\sim 10\,\mathrm{ps}$ and covered a wide spectral range from $1500\,\mathrm{nm}$ - $1620\,\mathrm{nm}$, as illustrated in Fig. 4-4. For the measurement, the pulses were split into a sample and reference path as shown in Fig. 4-3. The adjustable reference path incorporated a free-

4.4. Waveguide Characterization

space section with a motorized translation stage. In the sample path, a cleaved SMF fiber tip allowed coupling into the device under test. The samples were characterized in a double-pass set-up in which the other end of the device was butt-coupled to a silver mirror. In order to characterize active materials, the device under test could be pumped with a WDM coupler. Besides enabling pumping of the sample, the WDM coupler selectively introduced a high dispersion offset into the sample path ($\sim 90{,}000\,\mathrm{fs}^2$), which served to enhance the measurement resolution. As the combined output of both arms was spectrally resolved on an OSA, the dispersion was accurately determined from the detected fringe pattern, which is proportional to $\phi(\omega)$.
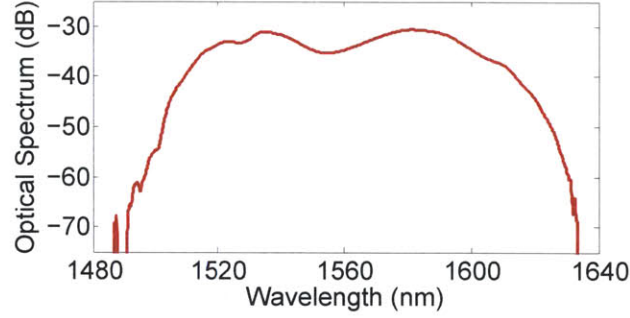
Figure 4-4: The SMF broadened EDFL laser white-light source with an output power of 12 mW for the dispersion measurements.

$$I = |E_s(t) \ + \ E_r(t)|^2 = \left| E_s \ \cdot \ e^{-2j(\phi_{s1}+\phi_{s2})} \ e^{j\omega t} \ + \ E_r \ \cdot \ e^{-2j(\phi_{r1}+\phi_{r2})} \ e^{j\omega t} \right|^2 \tag{4.1}$$

$$= |E_s|^2 \ + \ |E_t|^2 \ + 2 \, |E_s| \, |E_r| \, \cos\left[2(\phi_{s1} - \phi_{r1}) + 2(\phi_{s2} - \phi_{r2})\right] \tag{4.2}$$

$$= |E_s|^2 \ + \ |E_t|^2 \ + 2 \, |E_s| \, |E_r| \, \cos(\phi(\omega)) \tag{4.3}$$

In Eq. 4.3, the variable E_s denotes the electric field in the sample path. The phase ϕ_{s1} describes the accumulated phase without the device under test, and ϕ_{s2} represents the phase change after a sample was incorporated into the measurement set-up. Similarly, ϕ_{r1} denotes the reference path phase without a sample and ϕ_{r2} the change in the air path after

incorporating the sample to be measured. I represents the measured output intensity. By approximating the phases with Taylor expansions, the phase can be rewritten in terms of the group delay, group delay dispersion, and higher order dispersion terms. From a calibration measurement without a sample (when the cleaved fiber tip was directly butt-coupled to the silver mirror), the phases ϕ_{s1} and ϕ_{r1} were determined. Normalization of the measurement with respect to $|E_s|$ and $|E_r|$ in baseline measurements was achieved by individually blocking the sample and reference path. For more details, the reader is referred to [116].

From the detected fringe pattern on the OSA, the positions of the individual zero-crossings are derived. As the phase difference between two neighboring zero crossings is equal to π, the group delay dispersion and third order dispersion can be calculated by solving an equation array for all the displayed consecutive zero crossings, using the least mean square method. Thus, the more interference fringes are detected, the better the measurement resolution. As a consequence, longer sample lengths usually result in higher accuracy, and dispersion values greater than $1000\,\mathrm{fs}^2$ can be best characterized. By averaging over a certain number of measurements (usually 30, from which 10 % of the outlier values are discarded), results with small standard deviations can be obtained. In order to measure a dispersion profile over a range of wavelengths, this spectrally resolved method requires individual measurements to be performed for each center wavelength of interest.

4.4.3 Dispersion Measurement

With this white-light interferometer set-up, the dispersion for the waveguide chips was measured. Since the dispersion varied from chip to chip, due to fabrication tolerances in the thickness of the Er-doped waveguide core, 145 different waveguides were measured to obtain a reliable average dispersion value. The overall average dispersion amounted to around $3300\,\mathrm{fs}^2$ and $4500\,\mathrm{fs}^2$ for the 35 mm and the 50 mm waveguides, respectively. The group delay dispersion for five waveguide chips with similar dispersion values is shown in Fig. 4-5. The linear extrapolation between the measured points indicates that the normal dispersion increased proportionally for longer gain sections. The total measured dispersion value cor-

responded to a normal group delay dispersion of $40\,\mathrm{fs}^2/\mathrm{mm}$ for the Er-doped waveguide, if a waveguide dispersion of $45\,\mathrm{fs}^2/\mathrm{mm}$ was assumed for the passive taper sections. This GDD of $40\,\mathrm{fs}^2/\mathrm{mm}$ seemed higher than initially designed for.
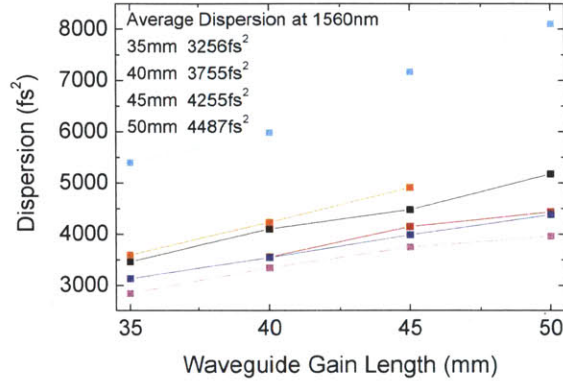
Figure 4-5: Dispersion measurement for five different waveguide chips.

However, for dispersion values of this order, a complex thin film coating with significant thickness would be required to compensate for the dispersion. As the beam experiences diffraction during propagation into the output coupler, high intracavity losses due to mode-mismatch when coupling back into the WG chip could be encountered. Therefore, the waveguide chips were refabricated. By increasing the height of the waveguide from $1.2\,\mu\mathrm{m}$ to $1.5\,\mu\mathrm{m}$, the overall dispersion was expected to be reduced significantly.

4.4.4 Waveguide Dispersion Characterization

In order to confirm a reduced group delay dispersion value, the re-fabricated waveguide chips with raised height were measured. However, to obtain a representative result, a large sample of chips had to be characterized. As the active waveguides were deposited by RF sputtering in a planetary rotation chamber, localized fabrication tolerances limited the height uniformity across the wafer. For one of the fabricated wafers (wafer 280), the Er-doped waveguide core center section measured $1.39\,\mu\mathrm{m}$, whereas the waveguide thickness towards the side of the wafer amounted to $1.45\,\mu\mathrm{m}$. The same effect occurred on the second wafer (wafer 281), which featured thickness variations between $1.48\,\mu\mathrm{m}$ and $1.53\,\mu\mathrm{m}$.

Because of this non-uniform fabrication profile, slightly varying mode-profiles and dispersion values were induced, depending on the original die location on the wafer.
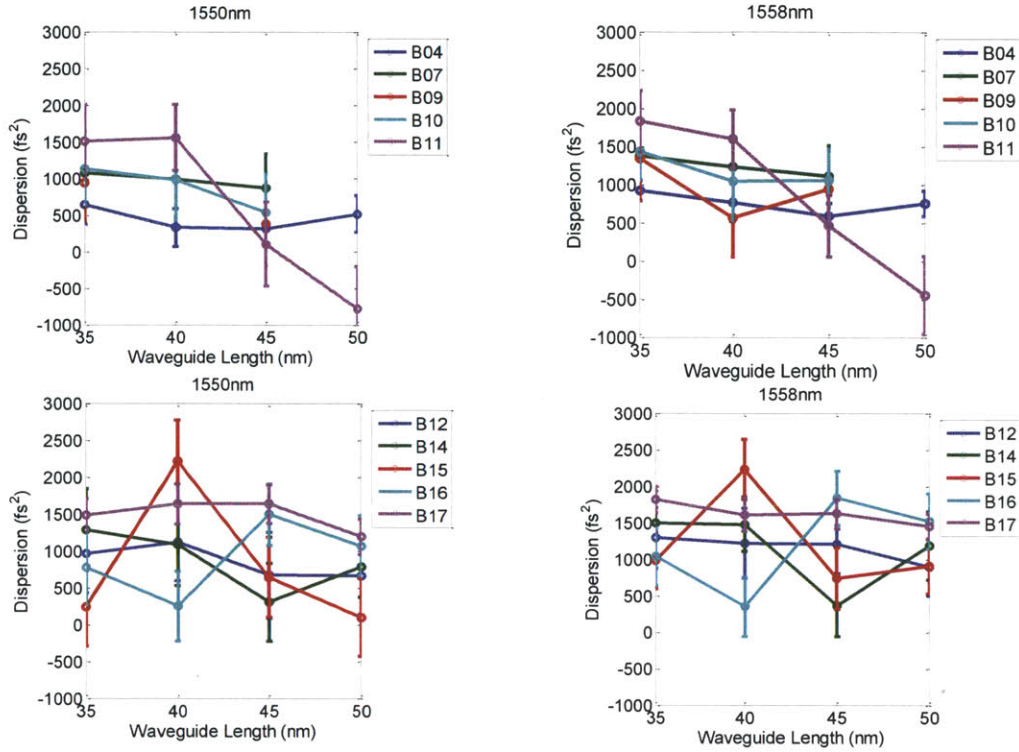
Figure 4-6: Waveguide dispersion measurement for refabricated WG chips.

A selection of the measured dispersion values are portrayed for 13 different waveguide chips in Fig. 4-6. Each measurement point was obtained by averaging over 30 dispersion measurement values for each wavelength. The error bar indicated the measurement deviation. The presented samples all originated from wafer 281, which featured slightly thicker Er-doped layers and thus smaller normal dispersion values. If these results are compared with the results in Fig. 4-5, the average dispersion for a 35 mm long waveguide was reduced from $\sim 3250\,\mathrm{fs}^2$ to $\sim 1400\,\mathrm{fs}^2$. This corresponded to a normal dispersion around $14\,\mathrm{fs}^2/\mathrm{mm}$ for the gain section, which implied a reduction in the dispersion by almost a factor of three when compared to the $1.2\,\mu\mathrm{m}$ thick waveguides. However, instead of the expected linear increase of the dispersion with longer waveguide lengths, as seen in Fig. 4-5, the disper-

sion evolution seemed less systematic in these measurements. Some measurements were even characterized by a negative slope, indicating anomalous dispersion for the longer gain sections on the waveguide. Thus, the mode profile was examined further.

4.4.5 Spatial Beam Profile Measurements

Fig. 4-7 shows numerical simulations of the desired fundamental mode in the gain waveguide (TE polarization). This mode features $1/e^2$ beam diameters of $3.5\,\mu$m x $1.7\,\mu$m. However, due to the $4\,\mu$m width of the waveguide, multiple modes were supported within the designed waveguide structure. In order to achieve single-mode operation, the waveguide layout was designed such that higher order modes encountered higher losses. For the $1.2\,\mu$m thick waveguide, the waveguide bends selectively introduced losses of 80 % for the higher order modes. However, the efficiency of the bends as mode strippers in the re-fabricated waveguide with $1.53\,\mu$m height was reduced and provided only 60 % multi-mode losses in the bends. Therefore, the cw beam profile was characterized to evaluate whether clean single-mode operation could be supported.
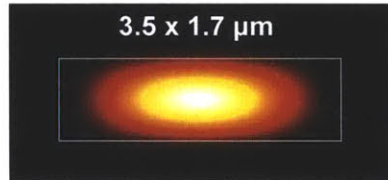
Figure 4-7: Simulation of fundamental TE mode in Er-doped waveguide (outlined as white rectangle) with $1/e^2$ beam diameters of $3.5\,\mu$m x $1.7\,\mu$m.
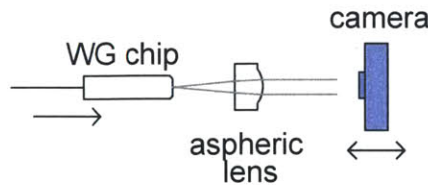
Figure 4-8: Set-up for single-pass beam profile measurement.

First, the spatial beam profile for a single-pass through the waveguide was evaluated. For low pump powers, the output of a 45 mm long gain waveguide was collected with an aspheric lens (C220TME-C). With an IR CCD camera (WinCamD), the spatial beam profile was recorded for varying distances to the lens, as shown in Fig. 4-8. After determining the half-angle of divergence Θ for the beam in the tangential (horizontal, x) and sagittal (vertical axis, y) plane, the mode profile was compared with the beam expansion for an ideal diffraction-limited Gaussian beam with the same waist ω_0. The M^2 beam quality (or beam propagation) factor is defined such that a value of 1.0 implies that the beam is diffraction-limited, which is the case for single-mode beams. The theoretical far-field divergence θ, e.g. for TEM_{00} Gaussian beams, is calculated by $\theta = \dfrac{\lambda^2}{\pi \omega_0}$. Thus, M^2 can be evaluated by Eq. 4.4:

$$M^2 = \frac{\Theta}{\theta} = \frac{\Theta}{\frac{\lambda^2}{\pi \omega_0}} \tag{4.4}$$

For low pump powers, the output beam diameters were measured when TE polarized light was coupled into the waveguide (assuming a Gaussian fit for the beam diameter), as shown in Fig. 4-9. From this measurement, the beam waist ω_0 and Θ (slope of measured beam diameter for small angles) were extracted. With Eq. 4.4, the resulting M^2 parameter for the two planes (denoted with x and y), were calculated as $M_x^2 = 3.5$ and $M_y^2 = 2.9$. These values imply the presence of higher order modes which are not sufficiently suppressed upon single-pass through the waveguide device. Depending on the input coupling, a combination of different higher order modes was excited, which resulted in slightly larger M^2 values when the measurement was repeated.

However, in the mode-locked laser cavity, resonator feedback in combination with gain saturation for the lowest loss mode was expected to suppress the higher order modes more efficiently than in the considered single-pass scenario. Therefore, the measurements were repeated for a cw-laser cavity, where 10 % output couplers on both ends of the waveguide defined the laser cavity. At the input, a coated fiber was coupled to the waveguide facet, while an output coupler mirror was butt-coupled on the other end.

138
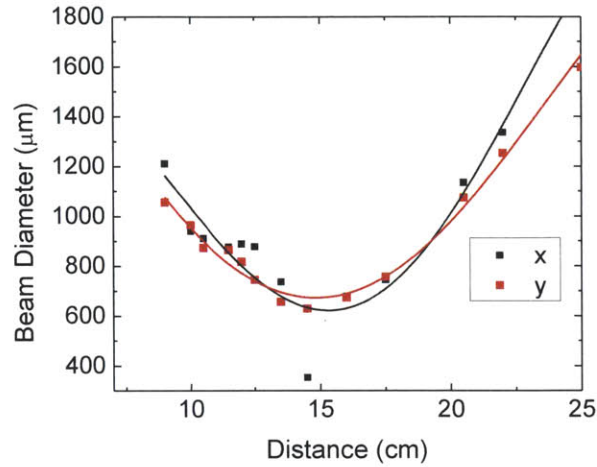
Figure 4-9: Gaussian beam diameter plotted for the WG output when TE polarized light was coupled into the WG.
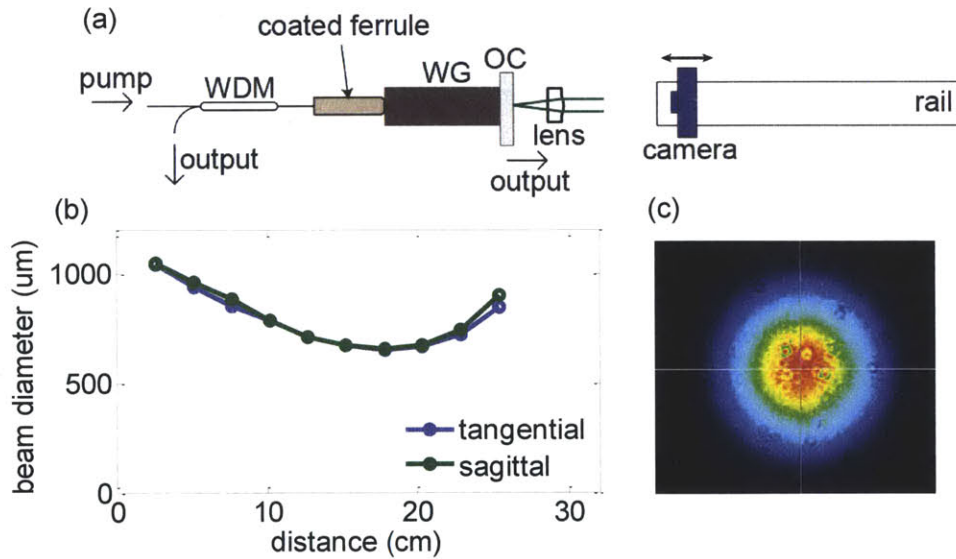
Figure 4-10: (a) Schematic to measure beam profile for a cw laser cavity. (b) Recorded beam diameter depending on the distance from the collimating lens for the tangential and sagittal axis, resulting in M^2 factors of 1.1. (c) Spatial beam profile close to the focus. Courtesy of Hyunil Byun.

The set-up for the measurement is depicted in Fig. 4-10 (a). The recorded beam diameters in the tangential and sagittal plane in Fig. 4-10 (b) follow each other closely, resulting in an estimated M^2 value of 1.1 for both dimensions. This M^2 value indicated that after multiple passes in the cavity, single-mode operation was supported, as desired. Fig. 4-10 (c) shows the recorded beam profile close to the focus with good uniformity and good resemblance to a Gaussian beam. At the same time, this measurement implied that the waveguide supported multiple modes during single-pass propagation through the waveguide. Thus, an accurate determination of the dispersion in the current configuration was challenging.

4.4.6 Modeling of Waveguide Dispersion

In order to obtain theoretically calculated values for the waveguide dispersion, numerical Finite-Difference Time-Domain (FDTD) simulations can be applied to solve for the modes and dispersion. Alternatively, analytical approximations to determine the effective refractive group index for rectangular waveguides can be used. In the following, the latter approach was chosen. After calculating an effective refractive index for the waveguide structure, the expected waveguide dispersion could be derived.

The effective index method was first proposed by Knox and Toulios [118] and has been extensively applied to rectangular waveguide structures (e.g., [119, 120, 121]). According to this methodology, the rectangular waveguide structure is approximated by two slab waveguides, whose effective indices can be evaluated individually. These two waveguides are coupled orthogonally to each other to reconstruct the original waveguide structure. This method can be applied as long as the total electromagnetic field can be well approximated by two de-coupled variable functions. Then, by separation of variables, two independent wave equations for each waveguide dimension with effective refractive indices can be formulated. For a more detailed derivation, the reader is referred to literature, e.g. [122].

In Fig. 4-11, the effective index concept is illustrated. The rectangular waveguide of interest in Fig. 4-11 (a) was decomposed into two corresponding slab waveguides. Depending on the chosen boundary conditions in each subsystem, the eigenvalues were determined

numerically for the TE and TM modes. By combining the various configurations for the respective mode numbers m and n, the supported TE and TM modes were calculated.
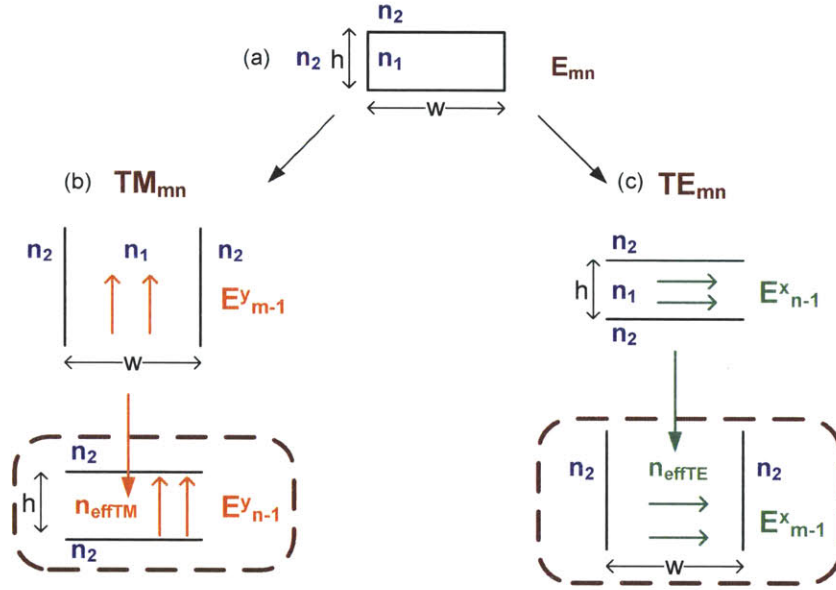
Figure 4-11: (a) Rectangular waveguide analyzed by effective-index method. (b) Calculation of TE mode by using slab of width w to approximate effective index for a slab waveguide of height h. (c) Calculation of TM mode by using a slab of height h to approximate effective index for a slab waveguide of width w.

After reducing the rectangular waveguide dispersion calculation to individual slab waveguides, a formalism by Kogelnik and Ramaswamy [123] for slab waveguide structures was applied. For a normalized guide index b and a normalized frequency $V = k_0 \, h \cdot (n_1^2 - n_2^2)$ (with k_0 the wave vector and h the waveguide core height), the dispersion relation for a symmetric slab waveguide (where the index of refraction for the substrate and cover layer are identical) can be expressed in the following form:

$$V \cdot \sqrt{1-b} \;=\; m\pi \,+\, 2 \cdot \tan^{-1}\left(\sqrt{\frac{b}{1-b}} \right) \qquad \text{TE mode} \qquad (4.5)$$

$$V \cdot \sqrt{1-b} \;=\; m\pi \,+\, 2 \cdot \tan^{-1}\left(\frac{n_1^2}{n_2^2} \cdot \sqrt{\frac{b}{1-b}} \right) \qquad \text{TM mode} \qquad (4.6)$$

$$b \;=\; \frac{n_{eff}^2 - n_2^2}{n_1^2 - n_2^2} \quad \Leftrightarrow \quad n_{eff} = \sqrt{b \cdot (n_1^2 - n_2^2) + n_2^2} \qquad (4.7)$$

In this notation, n_1 and n_2 denote the index of refraction in the core and cladding, respectively, and the integer m represents the mode index. For the waveguide evaluation, the following parameters were used: a height of $h = 1.53\,\mu$m, a width of $w = 4\,\mu$m, $n_1 = 1.62$ and $n_2 = 1.45$. By numerically solving the above equations, 11 guided modes (for $m = 4$ and $n = 2$), as shown in Table 4.1, were supported by the waveguide width. The validity of this approach was compared against numerical mode-solver solutions, which confirmed the obtained results. Thus, for the given waveguide configuration, slightly anomalous waveguide dispersion values (as measured in Fig. 4-6) were theoretically predicted. In particular, the calculated waveguide dispersion in Fig. 4-12 is consistent with the decrease in the measured anomalous waveguide dispersion with increasing wavelength in Fig. 4-6 (d), which became more anomalous with increasing waveguide length. As the lower order modes are highly confined within the waveguide core, the waveguide dispersion generally dominates over material dispersion.

The analysis in Sections 4.4.5 and 4.4.6 implied that for the dispersion measurement pure single-mode operation within the waveguide cannot be necessarily assumed. Thus, during the dispersion measurement, higher order modes were expected to have been excited besides the fundamental mode, depending on the input coupling. As the waveguide chip was double-passed, these higher order modes were not necessarily well suppressed. This can explain the recorded waveguide dispersion points for different waveguide lengths in Fig. 4-6.

The material dispersion contribution in fused glass amounts to $\sim 25\,\text{fs}^2/\text{mm}$, which has to be added to the modal waveguide dispersion. Thus, based on the theoretical derivations,

Mode	Effective refractive index	Dispersion (in fs^2/mm)
TE 00	1.57390	-12.38
TM 00	1.57432	-2.87
TE 10	1.54775	-35.81
TE 20	1.50609	130.18
TE 30	1.45763	2713.49
TE 01	1.47646	769.53
TE 11	1.45858	1980.32
TM 10	1.54951	4.70
TM 01	1.47795	715.00
TM 11	1.46339	1317.36
TM 20	1.51046	205.65
TM 30	1.46561	1593.10

Table 4.1: Waveguide dispersion for the respective individual modes at 1550 nm.

a WG dispersion of $\sim 13\,\text{fs}^2/\text{mm}$ for the fundamental TE mode in the Er-doped gain section was expected. This value corresponded well to the experimentally measured value around $14\,\text{fs}^2/\text{mm}$. As the input polarization was matched to the TE mode, the anomalous waveguide dispersion seemed to correspond well to dispersion values for the first higher order TE mode. Measurements for an input TM mode should result in larger normal group dispersion values.

The wavelength dependency of the dispersion was in general evaluated without changes to the butt-coupled configuration. For the same input coupling, excitation of the same higher order modes for the measurements could be assumed, which led to consistent data trends for different wavelength measurements in Fig. 4-6 (d). This is in contrast to the measurements over different gain lengths, where the input coupling differed between each measurement. Thus, it can be deduced that the overall waveguide dispersion was only slightly normal in these refabricated structures. To force the waveguide into stronger single-mode operation, one could add single-mode fiber in between the end facet of the waveguide and the silver mirror. Ideally, higher order modes would get suppressed in the SMF and increased the probability of measuring the dispersion of the fundamental waveguide mode.
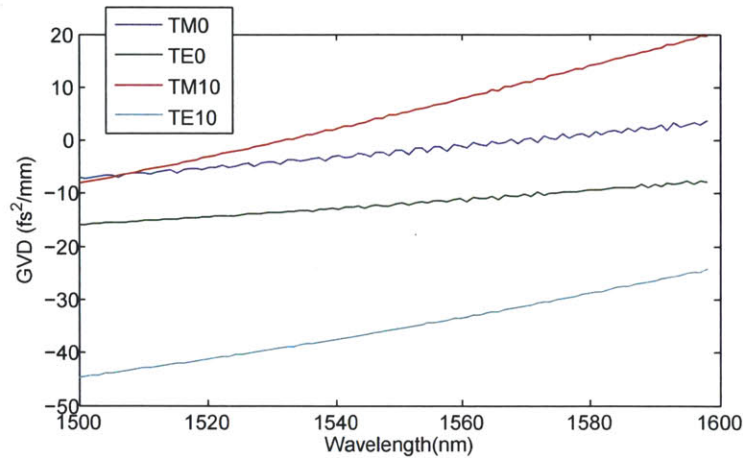
Figure 4-12: Estimate of waveguide dispersion in Er-doped gain section for different modes.

4.5 Design of Output Coupler Coating

In order to support soliton mode-locking, a mechanism for dispersion compensation was implemented so that an overall net anomalous intracavity dispersion could be achieved. Thus, a thin-film, dielectric coating was designed to provide the desired output coupling and dispersion compensation simultaneously. Such a coating could be either deposited directly on the waveguide facet or on a fiber ferrule to be butt-coupled against the waveguide. Both scenarios were numerically evaluated and their sensitivity towards small air gaps evaluated. Overall, the solution of coating the waveguide chips proved to be more robust and more insensitive to air gaps. Therefore, in order to reduce etalon effects for a non-ideal butt-coupling contact between the waveguide and the output coupler, the waveguide facet was coated directly.

4.5.1 Layer Design

A thin-film coating, based on a modified Bragg stack containing SiO_2 and Nb_2O_5 was designed, using the commercial thin-film design software OptiLayer. SiO_2 and Nb_2O_5 are standard dielectric materials for thin-film coatings because their deposition parameters can be well controlled (RMS thickness errors of less than 0.5% for ion beam sputtering by

Figure 4-13: Thin-film output coupler design: (a) Transmission, with wavelengths of interest at the pump and signal highlighted by purple box. (b) Magnified view of reflectivity around 1550 nm. (c) Group delay dispersion. (d) Magnification of group delay dispersion, which is practically flat for wavelengths around 1550 nm.

Advanced Thin Films, Inc.). As the waveguides were buried by a $10\,\mu$m thick oxide from the top surface (cf. Fig. 4-1), the WGs were considerably close to the chip surface (the input facet featured a cross-section with a height of $650\,\mu$m and width of 6 mm where the WGs were asymmetrically located just $10\,\mu$m below the top surface on a substrate of at least $633\,\mu$m thickness). However, the film uniformity of the deposited coating close to the edge and waveguide region should still be reasonable high.

The design goals for the coating were set to $90\,\% \pm 5\,\%$ transmission of the pump light between 970 nm - 980 nm, $10\,\% \pm 0.3\,\%$ output coupling over a bandwidth of 1525 nm - 1600 nm, and a group delay dispersion of $-1500\,\text{fs}^2 \pm 300\,\text{fs}^2$ for 1545 nm - 1575 nm. The designed coating reflectivity and dispersion matched these targets well, as illustrated in Fig. 4-13.

The optimized coating consisted of 32 layers, with SiO_2 as the first layer to be deposited on the WG in order to closely match the index of the Ge-doped glass, as illustrated in Fig. 4-14 (a). While the last 4 layers were fixed at quarter-wave thicknesses for 1560 nm, the other layer thicknesses were optimized by OptiLayer's inherent algorithm, including
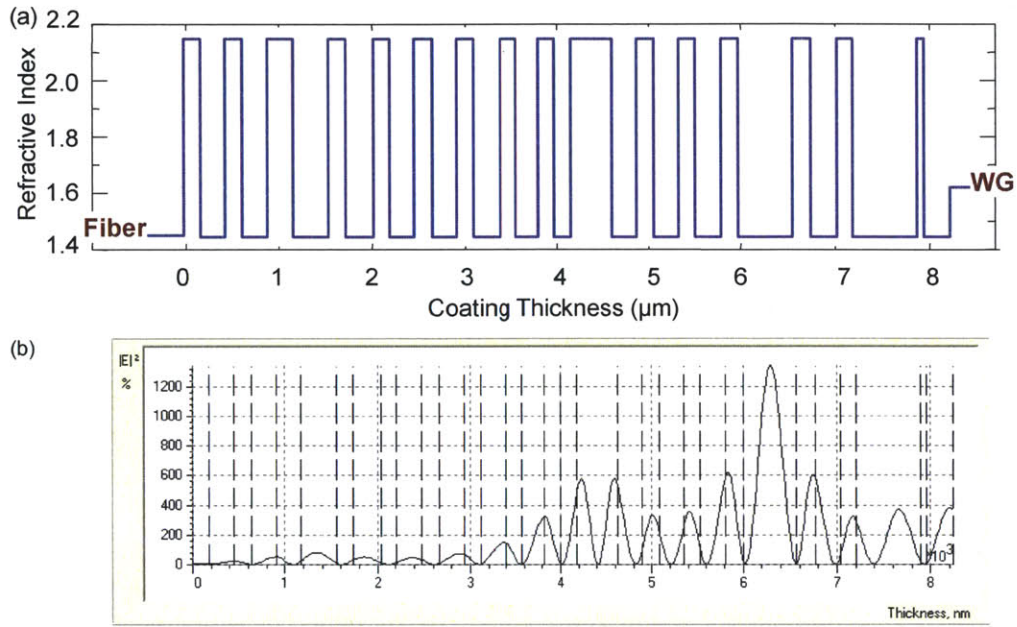
Figure 4-14: (a) Layer structure for output coating design with dispersion compensation. The coating was deposited on the waveguide input facet, to the very right of the layer stack. (b) Electric field distribution in output coupler coating for 1560 nm.

refinement procedures, automatic needle optimization and desensitization to fabrication errors. By evaluating the merit function MF for possible layer designs, the thickness for each layer is optimized until a local minimum is reached with the implemented routines $MF(x, \lambda) = \int_{\lambda_1}^{\lambda_2} [R(x, \lambda) - R_{target}(\lambda)]^2 \sim 0.62$. $R_{target}(\lambda)$ specifies the target design and $R(x, \lambda)$ represents the designed reflectivity, where x describes a vector containing all the individual thicknesses for each layer.

The designed coating thickness amounted to $8.24\,\mu$m and the corresponding electric field distribution at 1560 nm is plotted in Fig. 4-14 (b). Significant field contributions can be found at least up to $4\,\mu$m deep into the output coupler coating and longer wavelengths penetrate even deeper into the layer stack.

146

4.5.2 Beam Divergence in Coating

While the waveguide mode is guided on-chip, the mode diverges upon impinging on the SBR or any deposited thin-film coating. For coating thicknesses on the order of the mode dimensions, such beam divergence can impair the beam profile. Thus, diffraction of the reflected beam can lead to a decreased mode overlap with the WG mode, which reduces the coupling efficiency. Therefore, in the following, the impact of beam divergence is evaluated by modified thin-film simulations based on Hankel transforms, initially implemented in MATLAB by Li-Jin Chen. For this evaluation, radially symmetric modes are assumed, which pose a good approximation for the tapered out waveguide modes. The implemented framework is described in Appendix A.

In Fig. 4-15, the original output coupler reflectivity (denoted as 'Mirror') was calculated by superposition of forward and backward propagating electric fields. The coupling efficiency outlines the reduced coupling due to beam divergence, and the curve 'Total' combines the original output coupler reflectivity with the wavelength dependent coupling efficiency. For beam diameters between $6\,\mu m$ and $7\,\mu m$, the total reflectivity curve hardly undergoes any changes, as it gets reduced by $1.8\,\%$ and $0.6\,\%$, respectively, at $1560\,nm$.

However, for smaller mode diameters that have shorter Rayleigh ranges, beam divergence becomes a determining factor, as quantified in Table 4.2, and illustrated in Fig. 4-16. For beam diameters around $4\,\mu m$, the coupling efficiency is decreased by $11.5\,\%$ at $1560\,nm$.
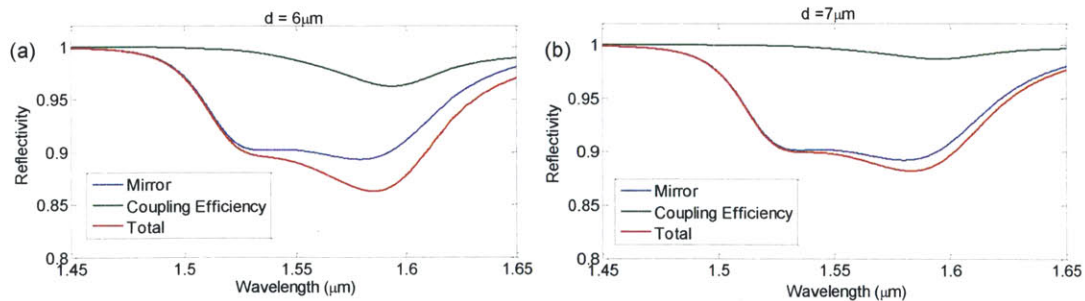
Figure 4-15: Output coupler reflectivity, coupling efficiency and resulting reflectivity profile for a beam diameter (a) of $6\,\mu m$ and (b) of $7\,\mu m$.

Beam diameter [μm]	Coupling Efficiency [%]		
	1550 nm	1560 nm	1590 nm
3	48.5	45.3	64
4	7.4	11.5	31
5	4.8	7.4	11
6	1.3	1.8	3.8
7	0.4	0.6	1.3
8	0.015	0.02	0.05

Table 4.2: Reduced coupling efficiency for various beam diameters upon propagation into output coupler coating.
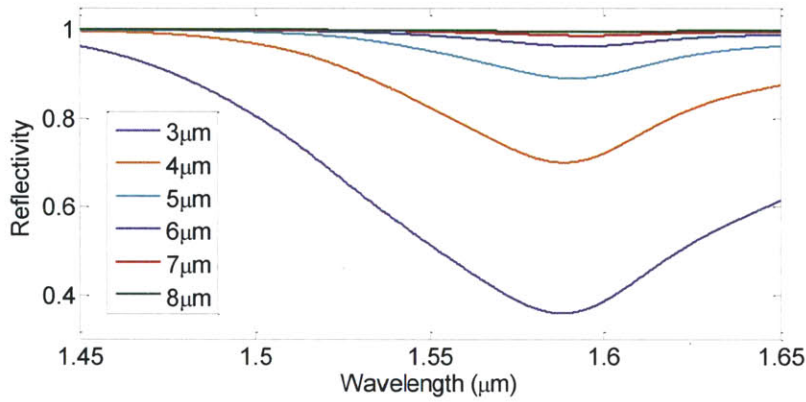
Figure 4-16: Coupling efficiency for output coupler depending on beam diameter.

Since the longer wavelengths penetrate deeper into the output coupler stack, their coupling efficiency gets reduced further.

Having evaluated the butt-coupling quality for the output coupler end of the waveguide, the other waveguide facet, which was coupled to the SBR, was examined w.r.t. the impact of beam divergence. As the SBR standing electric field pattern usually only exhibited significant intensities for penetration depths around $1\,\mu$m into the material stack, divergence effects were expected to have reduced impact compared to the output coupler case. Thus, simulations for various waveguide mode diameters and air gap lengths for a SBR (comparable to VA86 in terms of absorber layer but with a base reflectivity of only 94 %) were conducted. Fig. 4-17 summarizes the air gap lengths that could be tolerated, depending on the mode diameter, if intracavity coupling losses of less than 1 % were targeted. With

increasing spot sizes, larger air gaps of up to $5\,\mu$m for a beam diameter of $8\,\mu$m were acceptable because diffraction was reduced. Thus, in the case of mode dimensions around $7\,\mu$m by $7\,\mu$m, diffraction losses at the SBR end due to air gaps can be neglected. However, for modes with diameters of $2\,\mu$m or smaller, air gaps of $0.7\,\mu$m reduced the coupling efficiency by $6.5\,\%$, resulting in a total reflectivity of $87.8\,\%$, as shown in Fig. 4-18 (b). This analysis underlines the importance of mode tapering to achieve good butt-coupling.
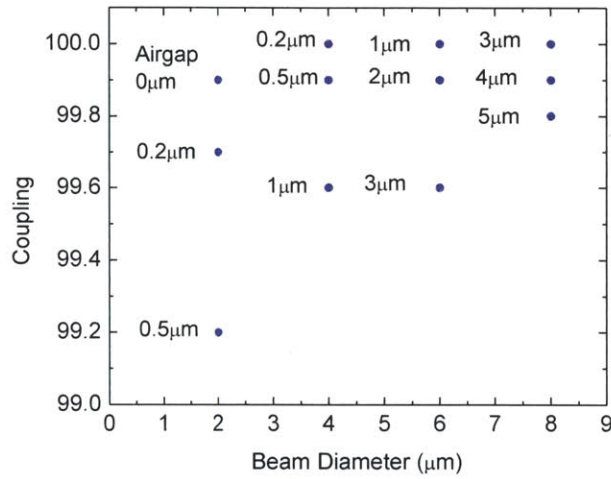
Figure 4-17: SBR coupling losses depending on beam diameter and air gap.
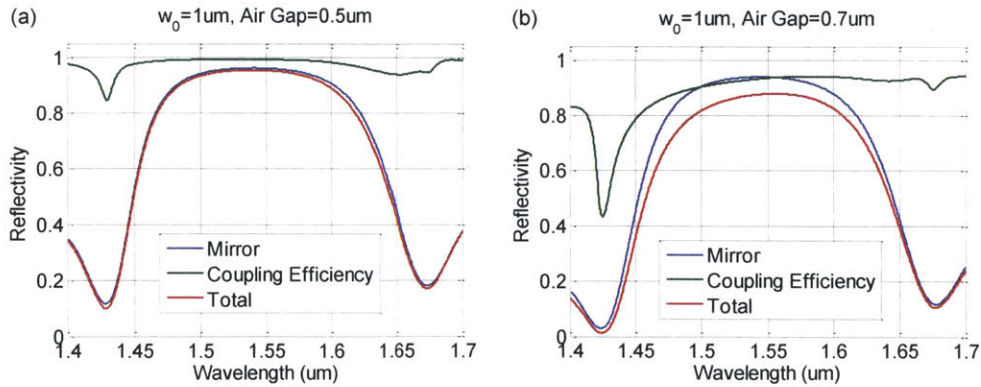
Figure 4-18: Impact of beam divergence on coupling efficiency for a beam diameter of $2\,\mu$m. (a) Without any air gap, (b) with an air gap of $0.7\,\mu$m, the coupling efficiency is reduced by $6.5\,\%$ at $1550\,$nm, resulting in a total reflectivity for the SBR-waveguide interface of $87.8\,\%$.

4.6   Conclusion and Future Work

In addition to careful characterization of the WG chips, numerical simulations were con-
ducted that captured the temporal dynamics of the resulting waveguide chip cavity by
applying the split-step Fourier method to a modified nonlinear Schrödinger equation. For
this evaluation, the measured intracavity power and the determined dispersion values were
used in order to identify a stable mode-locking regime. Thus, for the designed OC coat-
ing with an anomalous group delay dispersion of -1500 fs^2 and assuming high intracavity
pulse energies around 20 pJ, 200 fs short pulses were numerically predicted. However, the
mode-locking threshold is much lower and, depending on the repetition rate of the WG
laser, is below 10 mW. Measurements of the coated WG chips confirmed that for 370 mW of
launched pump power, intracavity powers up to 40 mW can be achieved. Thus, the analysis
so far indicated that mode-locking of the WG lasers should be achievable and detailed
characterization and analysis of the WG chips is currently in progress. Fig. 4-19 shows a
photograph of the WG chip.
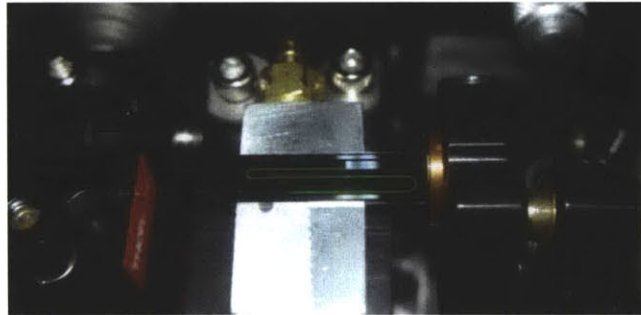
Figure 4-19: WG laser chip with pump-coupling through SMF fiber tip (on left) and butt-
coupled SBR (on right).

In the long run, the goal of this research is to obtain a highly integrated mode-locked
laser where the SBR is ideally directly integrated on the chip. Though different ideas
have been considered, these attempts are beyond the scope of this thesis since currently no
technology exists that can directly integrate semiconductor saturable absorbers with planar
waveguide technology.

As part of the EPHI (Electronic-Photonic Heterogeneous Integration) project, new mode-locked lasers were designed. The goal of this project is to build an ultra-low phase noise RF oscillator based on a wafer bonding approach between Si photonics and CMOS. Er-doped cw and mode-locked lasers are currently being implemented for this platform. The chosen waveguide structure consists of a low-loss, thin silicon nitride waveguide that provides single-mode guidance in an Er-doped gain film, which has been optimized for maximum overlap with the pump beam. Currently, different integrated components are being designed in order to assemble a complete mode-locked laser configuration capable of GHz repetition rates. In order to optimize the design, numerical simulations of different linear laser structures with repetition rates of a few GHz were performed. As the accumulated dispersion is relatively low in such short cavities, the numerical analysis revealed that sub-picosecond pulses can be supported, even without a specific implementation for a dispersion compensation mechanism.

As part of this new research thrust, different integration schemes for the SBR are being evaluated and more robust coupling methods to attach the SBR to a Si photonics wafer have been explored. Vertical coupling to the SBR on a planarized wafer surface can potentially reduce alignment sensitivity and air gap etalons in the current horizontal butt-coupling schemes. Mechanisms to redirect the mode towards the surface include mirrors etched at 45° or the use of integrated vertical grating couplers.

Therefore, these efforts are expected to produce a significant step forward towards highly integrated waveguide femtosecond lasers, compatible with Si photonics and CMOS technology.

Chapter 5

Saturable Bragg Reflector Design

In this Chapter, designs for saturable absorbers with modulation depths around 5 % are explored and a double-absorber structure is presented. Carrier lifetimes are engineered by proton bombardment, since reduced recovery times are particularly important for high-repetition rate laser cavities. The optical performance of different absorbers is explored and the wavelength tunability of butt-coupled SBRs (see also Chapter 2) is further analyzed. The work in this chapter was performed in collaboration with Prof. Leslie Kolodziejski and Gale Petrich, who grew the saturable absorber mirrors by molecular beam epitaxy (MBE).

5.1 Background

A saturable absorber is characterized by a nonlinear reflectivity response and is a key element for pulse shaping in femtosecond laser cavity. Low intensity light gets absorbed and encounters higher losses as carriers are excited from the ground state into the upper state conduction band levels. With increasing depletion of carriers in the ground state, saturation sets in so that higher intensities face reduced losses. Thus, high intensity spikes are amplified, whereas low-intensity noise and any small perturbation is absorbed. This effect provides an efficient self-starting and pulse stabilization mechanism for mode-locking. Moreover, during each round-trip, the low-intensity leading edge of the pulses is more

strongly absorbed, which results in pulse narrowing [31].

A saturable Bragg reflector (SBR) is a unique implementation that unites mirror resonator and absorber functionalities in one compact device that is based on a semiconductor Bragg mirror stack. Though alternative saturable absorbers are available (carbon nanotubes [45, 46, 47, 48] or graphene [124, 125]), an SBR is the preferred choice for the presented laser systems because the SBR exhibits high damage thresholds and can be engineered for short recovery times, which is ideal for high repetition rate cavities.

For an optimized femtosecond laser operation, the SBR modulation depth (maximum dynamic range in saturable absorption), the saturation fluence F_{Sat} (1/e onset value of saturation) and the recovery time τ are tailored to the laser operating point. In general, the laser fluence is desired to be larger by a factor of 2 to 3 than the saturation fluence [126] and ideally, full recovery of the absorber carriers should be achieved before the next pulse arrives at the absorber. In the following, different design options and the specific engineering of the absorber lifetimes through proton bombardment (PB) are presented.

5.2 Double Absorber Design

For efficient mode-locked operation, the saturable absorber losses should be of the same order as the intracavity losses. For fiber lasers with an external free-space focusing section on the SBR, a modulation depth higher than the measured SBR VA86 modulation depth of 2.5 % is desired. In addition, small saturation fluences allow operation even at low intracavity pulse energies. Therefore, different design options to increase the modulation depths are evaluated in the following.

A semiconductor SBR comprises two sections, a high reflectivity mirror (usually a Bragg mirror stack) and the actual absorber section. A Bragg reflector consists of alternating quarter-wave thick layers of high and low index semiconductor materials, which are transparent at the design wavelength of 1550 nm to minimize non-saturable (linear) losses. A high reflectivity over a wide bandwidth is achieved by choosing two mirror materials with high index contrast and by stacking a large number of mirror pairs. In the following, for all

the designed structures, the broad-band semiconductor mirror is defined by 22 pairs of GaAs and $Al_{0.95}Ga_{0.05}As$ quarter-wave thick layers. Close to octave-spanning bandwidths were pioneered in oxidized mirror structures in Prof. Leslie Kolodziejski's group [127, 128, 129].

The absorber section in semiconductor saturable absorbers can either be composed of multiple quantum wells or semiconductor bulk layers. As higher modulations depths were targeted, designs featuring bulk absorption sections were pursued. The VA86 SBR featured a 60 nm thick $In_{0.537}Ga_{0.463}As$ absorber layer that was centered with respect to the electric standing wave field pattern and embedded in a half-wave GaAs cladding layer. In the SBR designs, bulk semiconductor layers were favored over quantum wells, as bulk layers demonstrated comparable performance characteristics but featured reduced fabrication complexity and lower sensitivity to layer tolerances.

In order to achieve higher saturable absorption, a design consisting of a thicker absorber layer was considered, as illustrated in Fig. 5-1. By extending the absorber thickness beyond 60 nm, the overlap between the electric field pattern and the absorber section increased. However, the additional electric field contributions consisted mostly of lower intensities so that overall the absorption characteristics barely changed. Thus, the absorber layer thickness was widened further to capture a second peak of the electric field. A 240 nm thick $In_{0.537}Ga_{0.463}As$ absorber yielded a reflectivity decrease by $\Delta R = 13\%$, cf. Figs. 5-1 (a) and (b). Assuming that one third of ΔR were saturable losses, modulation depths on the order of 4.3 % can be obtained. By adding an anti-reflection coating layer on top of the SBR, as illustrated in Fig. 5-1 (c), the reflectivity was reduced to $\Delta R = 37.5\%$, which led to an estimated modulation depth of 12.5 %. The anti-reflection coating, which consisted of a quarter-wave thick layer at the mirror design wavelength, provided an effective impedance matching between the air and the semiconductor saturable absorber over a limited bandwidth. The refractive index was given by $n_{AR} = \sqrt{n_{GaAs}} \approx \sqrt{3.43} \approx 1.85$ with a thickness of 209.2 nm. Thus, such designs are good for fiber lasers with higher intracavity losses, e.g. in external free-space laser configurations, where round-trip coupling losses from fiber to air and back into the fiber can be on the order of 20 %.

Thermal damage of the saturable absorber was analyzed in Chapter 2.3.4 and was par-
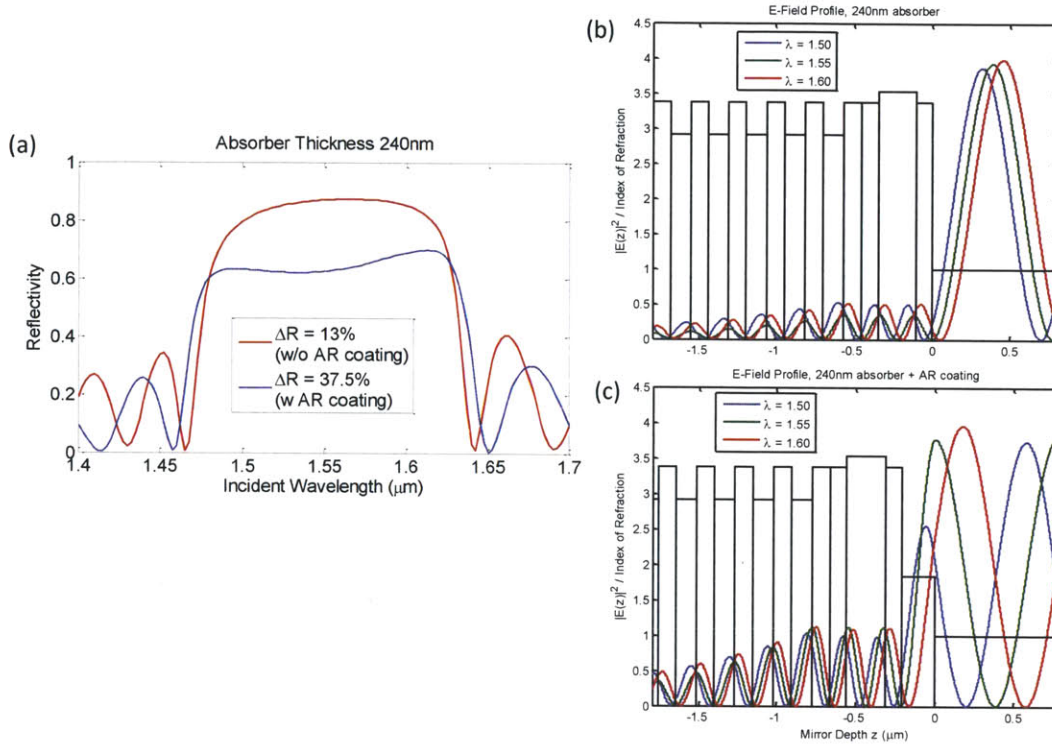
Figure 5-1: SBR design with 240 nm thick absorber. (a) Reflectivity curve with and without an additional anti-reflection coating. (b) Standing wave electric field pattern for three different wavelengths of $1.5\,\mu m$, $1.55\,\mu m$, and $1.60\,\mu m$ for a 240 nm thick absorber. (c) Standing wave electric field pattern for the same SBR as in (b) with an additional AR top-coating.

tially attributed to absorption of signal and pump light in the InGaAs absorber layer. Therefore, besides minimizing non-saturable losses, thermal damage thresholds were considered for the design of the SBR. The absorber overlap with the peaks of the electric field wave patterns was optimized, while minimizing the total absorber width. Thus, a double absorber structure was designed with layer thicknesses, as outlined for VA147 and VA148 in Table 5.1. Instead of one continuous absorber layer, two absorber layers of 67.5 nm were placed at the peak of the standing wave pattern of the electric field, surrounded by a GaAs cladding layer. With this design, a maximum reflectivity that was comparable to the presented design in Fig. 5-1 could be achieved. The reflectivity of this SBR amounted to 87 %,

Layer	Material	Thickness [nm]		
		VA147	VA148	VA86
Top Cladding	GaAs	68.1	83.2	83.2
1. Absorber	$In_{0.537}Ga_{0.463}As$	67.5	67.5	60
Cladding	GaAs	132.9	132.9	83.2
2. Absorber	$In_{0.537}Ga_{0.463}As$	67.5	67.5	0
Cladding	GaAs	64.8	64.8	0
Bragg Mirror(x 22)	GaAs	108.9	108.9	114.7
	$Al_{0.95}Ga_{0.05}As$	134.4	134.4	132.9

Table 5.1: Fabricated layer thicknesses of SBR VA147, VA148 and VA86.
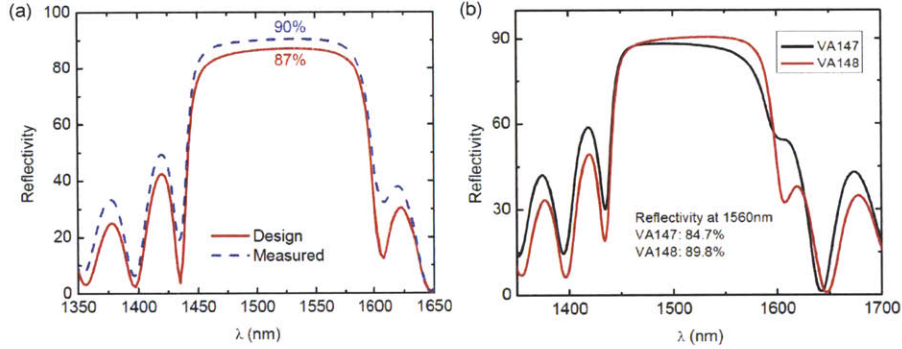
Figure 5-2: (a) Comparison between modeled and measured reflectivity for VA148. (b) Comparison between measured reflectivity curves of VA147 and VA148.

as illustrated in Fig. 5-2 (a), which yielded an estimated modulation depth of 4.3 %.

The SBR was grown with two slight modifications: In the first growth run of the structure VA147, the top cladding layer was thinner than the half-wave thick design, resulting in a tilted reflectivity profile, which favored shorter wavelengths over the operating wavelength at 1550 nm. Modeling of an additional top cladding layer (see Fig. 5-3) suggested that a more uniform reflectivity profile for a GaAs layer of ~ 20 nm on top of the grown VA147 could be achieved. While the absorber and mirror sections of VA147 and VA148 were identical, the top cladding layer for VA148 was re-grown and consisted of an additional 15.1 nm GaAs thick top layer. The measured reflectivity of VA148 with a maximum reflectivity of 89.9% at 1550 nm (which can have around 2% offset in the absolute reflectivity value due to the calibration of the system) agreed well with the design reflectivity of 87% in Fig. 5-2 (a).
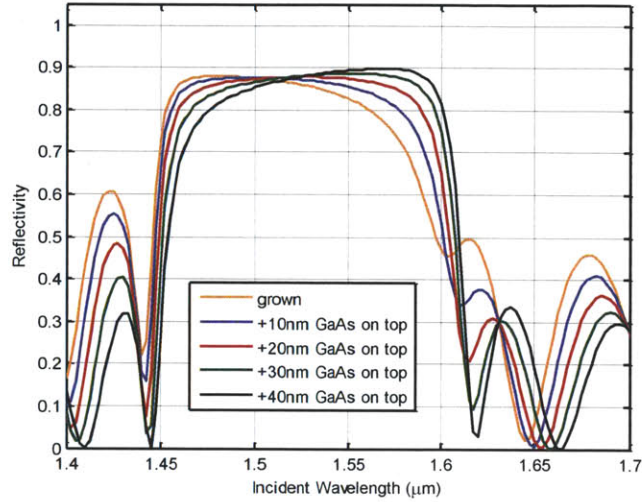
Figure 5-3: Impact of top cladding layer thickness changes on reflectivity.

The comparison of the measured reflectivity profile of VA147 and VA148 in Fig. 5-2 (b) (as determined by a Cary spectrophotometer measurement) illustrates the more uniform reflectivity for SBR VA148 through the additionally overgrown GaAs layer. The corresponding standing electric field wave pattern are shown in Fig. 5-4 for (a) SBR VA147 and (b) SBR VA148.

5.2.1 Pump Reflective Coating

In the discussed 1 GHz fiber lasers, the residual pump light impinging upon the saturable absorber constituted up to two-thirds of the coupled pump power since the overall pump absorption was limited by the short gain fiber length. Therefore, to protect the absorber layer from pump light, a pump-reflective coating was deposited on top of the grown SBRs by Peter O'Brien from Lincoln Labs.

The pump-reflective coating was composed of a series of alternating quarter-wave thick layers at 980 nm of SiO_2 and Ti_3O_5, with the bottom Ti_3O_5 and the top SiO_2 layers corresponding to a half-wave thicknesses (for details cf. Table 5.2). The total thickness of the PRC amounted to $1.255\,\mu$m. The design was optimized for a high-reflective pump window of 96.8% reflectivity while transmission at the signal wavelengths was maximized to 0.3 %,
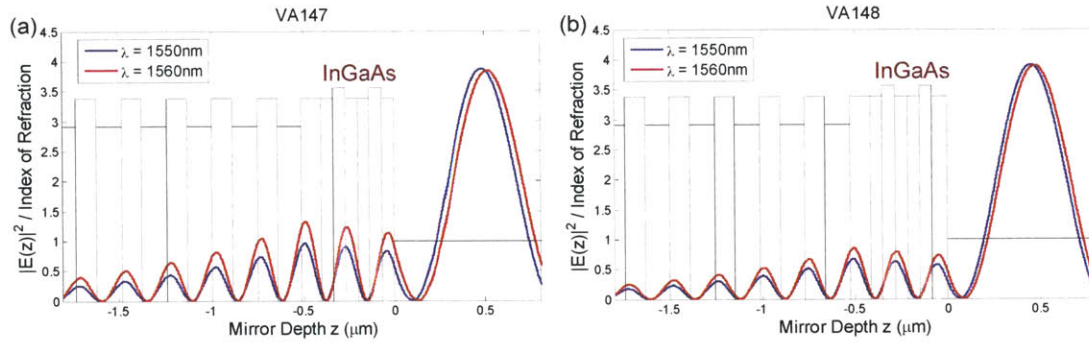
Figure 5-4: Standing electric field wave pattern for (a) VA147 and (b) VA148 at 1550 nm and 1560 nm for two absorber layers of InGaAs.

Layer	Material	Thickness [nm]	Index of Refraction at 980 nm
Top (Air)	SiO$_2$	232	1.45
3x	Ti$_3$O$_5$	105	2.25
	SiO$_2$	166	1.45
Bottom (SBR)	Ti$_3$O$_5$	210	2.25

Table 5.2: Layer sequence for pump-reflective coating, as designed by Peter O'Brien.

as shown in Fig. 5-5.

While the impact of the pump-reflective coating was already studied for the SBR VA86 in Section 2.2, the SBR VA147 and VA148 with pump-reflective coatings are analyzed in the following. Fig. 5-6 (a) shows a comparison between the numerically predicted and the measured reflectivity for VA147 PRC. At a wavelength of 1550 nm, the design featured a reflectivity of 70.5 %, whereas the measured result indicated a higher value of 82.2 %. However, for the numerical simulation only estimates for the refractive indices of the dielectric materials were used, which resulted in a certain tolerance for the designed reflectivity characteristics. Moreover, the spectrophotometer can determine relative differences in reflectivities very accurately, but can add an offset into any absolute measurements. Fig. 5-6 (b), which shows the same sample measured with a Perkin Elmer instrument at Lincoln Lab and at MIT with the Varian Cary spectrophotometer, suggests that different reflectivity calibrations affect the absolute measurement (while the wavelength calibration agrees very well). For the design wavelength at 1550 nm, the reflectivity was determined as 75.1 % and 81 %
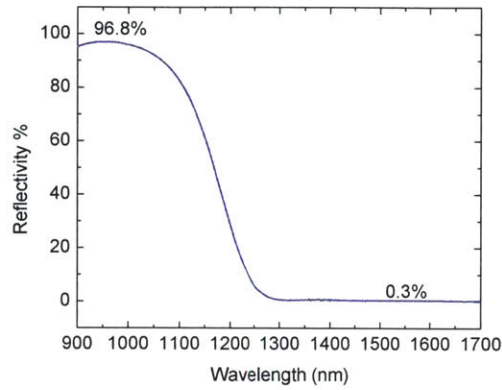
Figure 5-5: Measured reflectivity of pump-reflective coating. Courtesy of Peter O'Brien.

by the LL and MIT measurement, respectively. Combined with the variation between the design and measurement, this implies that the reflectivity measurement at MIT might have generated slightly higher values. Nonetheless, both measurements in Fig. 5-6 (b) emphasize the high reflectivity pump window and the same reflectivity shape curve.
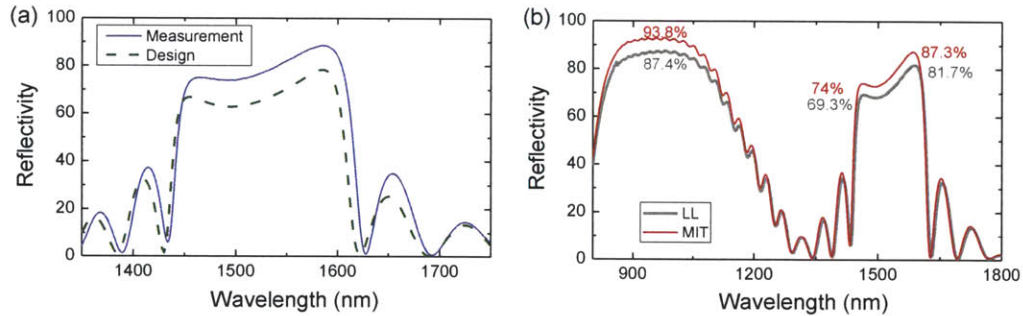
Figure 5-6: (a) Design and measured reflectivity of VA147 PRC and (b) Reflectivity measurements at LL and MIT (Perkin Elmer used with an integration sphere and Varian Cary spectrophotometer).

5.2.2   Reduction of Carrier Lifetimes

The relevant time constants associated with the absorption dynamics in SBRs can be studied by pump-probe characterization. In a pump-probe measurement, the pump or excitation pulse is absorbed by the material. A second probe pulse, whose delay time is varied relative

to the pump pulse, efficiently traces the induced changes in the material properties.

After excitation by the first femtosecond pulse, carriers are generated and form a non-equilibrium distribution. Due to scattering effects, the carriers thermalize and can be described by a hot Fermi distribution, usually on a time-scale of around 200 fs. This hot carrier gas interacts with lattice phonons and through carrier cooling, carriers get distributed around the bottom of the conduction band (~ 1 ps). On a longer time-scale, the carriers get trapped in impurity states (100 fs to 100 ps), recombine in recombination centers and midgap states, or induce radiation (up to nanoseconds) [130, 131]. Thus, each saturable absorber is characterized by two relevant time constants: a fast component, dominated by the intraband thermalization and a slow component due to carrier recombination and trapping.

Shorter absorber recovery times are favorable to generate high repetition rate lasers and to facilitate the onset of self-starting for the mode-locking process (determined by the slow time constant). Therefore, different approaches to reducing the carrier lifetimes can be pursued. During low-temperature MBE growth of lattice-mismatched materials, strain and additional defect points are introduced at the interface of different materials. With ion bombardment after the completed growth of the SBR [132, 133], the recovery times can be engineered further to the desired specifics. Light ions like protons are favored because they can be implanted without excessive accelerating voltages [134] and they introduce less non-saturable losses compared to heavier ions. Along its trajectory path, each proton generates defects before it is stopped and implanted in the material.

Two different effects can contribute to energy loss of the proton. Coulomb interactions with the complete electron clouds results in an effective 'viscosity' material effect that reduces the kinetic energy of the protons and induces ionization of the target material. This energy loss per unit propagation length $\frac{dE}{dx}$ due to inelastic scattering is proportional to the incoming ion energy E (for low energies) [135] and is referred to as electronic stopping S_e. Nuclear interactions between the proton and lattice leads to elastic collisions, change in momentum and direction of the proton. If the incoming ion is sufficiently slow, damage sites, interstitial defects, and vacancies can be generated in the material. However, for

proton bombardment of the presented SBRs, electronic stopping predominates [136] and is larger by approximately a factor of 100. This mean energy loss/stopping power curve is described by the Bethe-Bloch formula [137, 138]. The statistical distribution of the protons in the material can be estimated to first order by a Gaussian distribution [135], as shown in Eq. 5.1.

$$N(x) = \frac{\Phi}{\sqrt{2\pi} \cdot \Delta R_p} \, \mathrm{e}^{(x-R_p)^2/(2 \cdot \Delta R_p^2)} \tag{5.1}$$

Here, the projected range R_p describes the average deposition depth and the straggle ΔR_p denotes the standard deviation of the range. The skewness (related to the third moment) captures any asymmetry of the distribution. A negative skewness indicates an increased accumulation towards the surface side of the projected range. The kurtosis is related to the distortion of the distribution (fourth moment), with values larger than 3 (3 is representative of a normal Gaussian) indicating a flatter top. These parameters can generally be obtained from tables or calculated by Monte-Carlo simulations.

To model the impact of proton bombardment, SRIM (Stopping Range of Ions in Matter) and TRIM (Transport of Ions in Matter) simulations were conducted. The core of these simulations is provided by the TRIM package, which calculates the distribution of ions through Monte-Carlo methods in compound semiconductors. This numerical simulation tool can be used to estimate the projected range and target damage profile of the protons in the saturable absorber (see [139], version SRIM-2008) and the straggle, defect generation and ionization for various SBRs was determined.

The goal of the proton bombardment is to generate a uniform damage profile that reduces the carrier lifetimes. Defects are generated at the expense of increasing non-saturable absorption by proton implantation. For single-absorber SBRs, energies of 40 keV were used for the proton bombardment (cf. VA86 in [140]). However, for a more complex double-absorber design, optimizing the effect of the implanted protons at various points in the SBR stack with TRIM calculations is critical. SRIM calculations confirmed that the electronic stopping dominated over nuclear interactions ($S_e \approx 2 \cdot 10^{-1}\,\mathrm{MeV/(mg/cm^2)}$ and $S_n \approx 7 \cdot 10^{-4}\,\mathrm{MeV/(mg/cm^2)}$ for InGaAs).

162

For VA148, the first and second absorber layer end 150.7 nm and 351.1 nm deep in the layer stack, respectively, while the Bragg mirror starts at a depth of 415.9 nm. For proton bombardment energies of 40 keV and 60 keV, the projected range of the protons with R_p = 297.6 nm, ΔR_p = 80 nm and R_p = 418.5 nm, ΔR_p = 97.6 nm, respectively, is displayed in Figs. 5-7 (a) and (d). Thus, for higher energies, the protons penetrate deeper into the material and generate more defects in the second absorber layer for energies of 60 keV. The collision event plots shown in Figs. 5-7 (b) and (e) indicate two phenomena: First, the peak of the target displacements/vacancies is shifted by about 40 nm towards the surface from the projected range. This implies that once the protons have lost a significant amount of their kinetic energy (towards the end of their trajectory), their interaction time with atoms increases and the highest concentration of defects is created. Second, defects accumulate at the interface between different layers where due to lattice mismatch, the material growth itself has been strained. Figs. 5-7 (b) and (e) highlight the number of In vacancies in the InGaAs absorber. The ionization curves Figs. 5-7 (c) and (f) describe the fairly uniform energy loss to the target electrons throughout the absorber section, which partially gets released as heat or phonons.

In order to obtain a more uniform damage profile, multi-energy proton bombardment schedules were studied where the material is bombarded with protons of varying acceleration and dosage. Such multi-energy bombardments have been shown to generate superior performance characteristics in n-GaAs [141]. Thus, a bombardment schedule with energies of 25 keV and 60 keV was chosen to provide a more uniform damage profile along the saturable absorber, as depicted in Fig. 5-8. Table 5.3 provides an overview over the three selected proton-bombardment schedules for samples VA147 and VA148. Discussions with Joe Donnelly from Lincoln Lab provided helpful insight into optimizing the proton-bombardment schedules.

After proton-bombardment of quarter wafer SBRs, some samples were coated with a pump-reflective coating. The device reflectivity was measured with a Cary spectrophotometer in CMSE, as shown in Fig. 5-9. The reflectivity at 1550 nm amounts to 82.2 % for no PB and 81.0 % for PB IIIb, which features the highest proton dosage of all schedules.
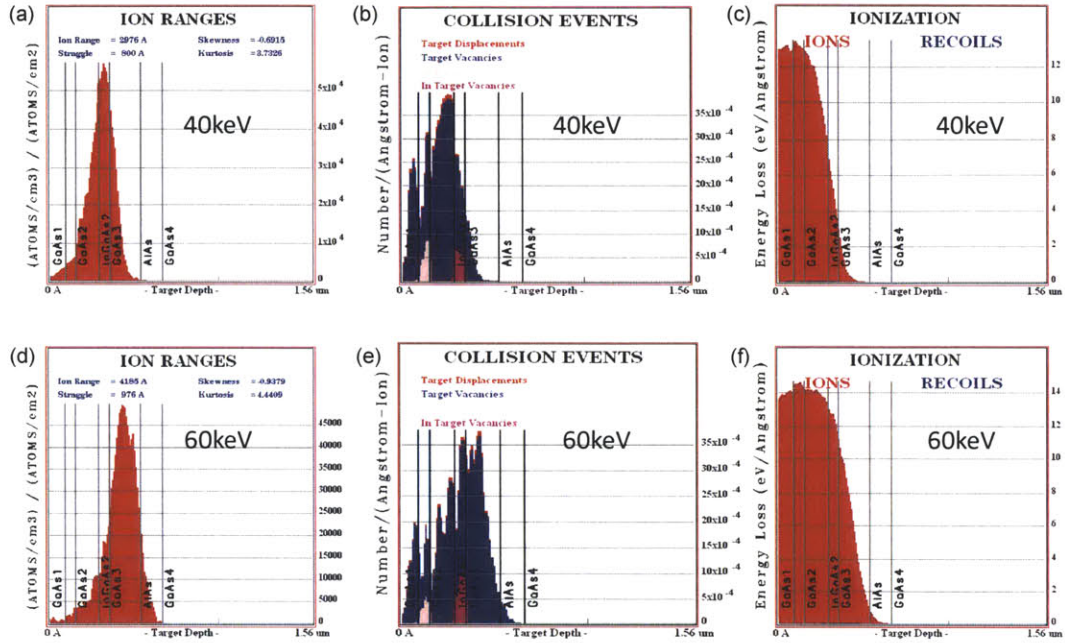
Figure 5-7: TRIM modeling of proton bombardment with $40 \, \text{keV}$ ($R_p = 297.6 \, \text{nm}$, $\Delta R_p = 80 \, \text{nm}$) and $60 \, \text{keV}$ ($R_p = 418.5 \, \text{nm}$, $\Delta R_p = 97.6 \, \text{nm}$).

Schedule Name	Proton Energy	Dose [protons/cm^2]
PBI	$40 \, \text{keV}$	$1 \cdot 10^{14}$
PBIIa	$60 \, \text{keV}$	$5 \cdot 10^{13}$
PBIIb	$60 \, \text{keV}$	$1 \cdot 10^{14}$
PBIIIa	$25 \, \text{keV}$	$1 \cdot 10^{13}$
	$60 \, \text{keV}$	$5 \cdot 10^{13}$
PBIIIb	$25 \, \text{keV}$	$5 \cdot 10^{13}$
	$60 \, \text{keV}$	$1 \cdot 10^{14}$

Table 5.3: Proton bombardment schedules for the double absorber SBRs VA147 and VA148.

164
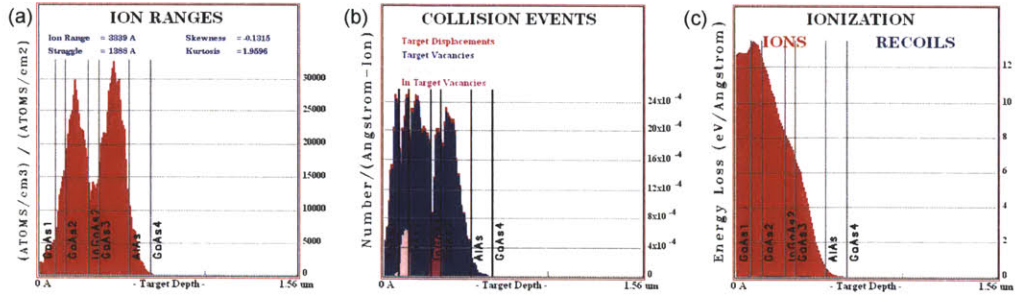
Figure 5-8: TRIM modeling for proton bombardment with 25 keV and 60 keV for a more uniform damage profile.
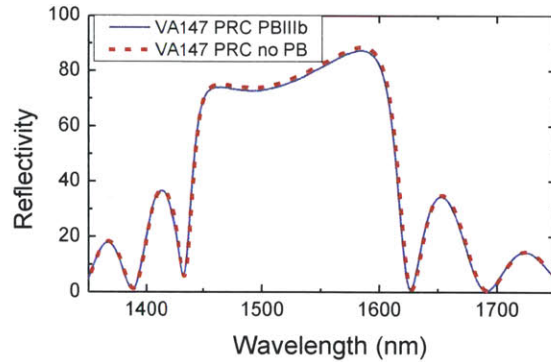
Figure 5-9: Reflectivity for VA147 PRC without any proton bombardment and with PB schedule IIIc. The reflectivity at 1550 nm is measured at 82.2 % for no PB and 81.0 % for PB IIIb.

However, the losses introduced through the creation of new defect states only contributed to ~1 % change in reflectivity. Pump probe measurements on the proton-bombarded samples confirmed these results that the reflectivity barely changed [140]. This indicates that the proton bombardment design was optimized well such that the ion implantation did not significantly increase the linear absorption losses.

Pump probe measurements, conducted by Ali Motamedi, on VA147 and VA148 implied that recovery times were reduced from ~11 ps to ~6.5 ps for PBIIIc. Table 5.4 gives an overview of the SBR parameters, for more details, the reader is referred to [140]. Table 5.5 summarizes the pump probe measurement results for four different SBRs.

SBR	PB	Modulation Depth	Saturation Fluence	Non-saturable Losses
VA147	no PB	7.5 %	$4.7\,\mu\mathrm{J/cm^2}$	8 %
VA148	PB0	3.9 %	$5.4\,\mu\mathrm{J/cm^2}$	6.2 %
	PBI	5.0 %	$6.1\,\mu\mathrm{J/cm^2}$	5.2 %
	PBIIa	4.0 %	$5.8\,\mu\mathrm{J/cm^2}$	6.0 %
	PBIIb	3.9 %	$6.4\,\mu\mathrm{J/cm^2}$	6.2 %
	PBIIIa	3.7 %	$6.5\,\mu\mathrm{J/cm^2}$	6.4 %
	PBIIIb	9.0 %	$4.4\,\mu\mathrm{J/cm^2}$	8.0 %

Table 5.4: Pump-probe measurement results for SBR VA147 and proton-bombarded SBR VA148 [140].

Sample	Modulation Depth ΔR [%]	Sat. Fluence F_{Sat} [$\mu\mathrm{J/cm^2}$]	Non-saturable Loss [%]	Recovery Time τ [ps]
VA86	3.9	11	1.1	9.0
VA86 PRC	12	3.7	1.1	9.0
VA147	7.5	4.7	8	10.5
VA148	4.0	5.4	6.2	10.5

Table 5.5: Summary of characterized SBRs [140].

5.2.3 Optical Performance

In the following, the optical performance of different proton-bombarded SBRs VA148 and selected SBRs were tested in developed fiber laser systems.

Various samples of the proton-bombarded SBR VA148 were incorporated into a 625 MHz fiber laser with an external free-space section (see Chapter 2.4.4). Fig. 5-10 and Table 5.6 summarize the optical performance parameters for different levels of proton-bombardment for SBR VA148 at comparable pump power levels. Small shifts in the center wavelength were observed and the 3-dB bandwidth increased slightly for the proton-bombarded samples.

VA148 PRC	Pump Current[mA]	P_{out} [mW]	$\Delta\lambda$ [nm]	λ_{Center} [nm]
no PB	711	5.6	5.8	1560.9
PBI	901	7.1	7.9	1558.9
PBIIIb	704	5.1	6.7	1561.3

Table 5.6: Optical performance parameters for proton-bombarded VA148 in an external 625 MHz EDFL.

166
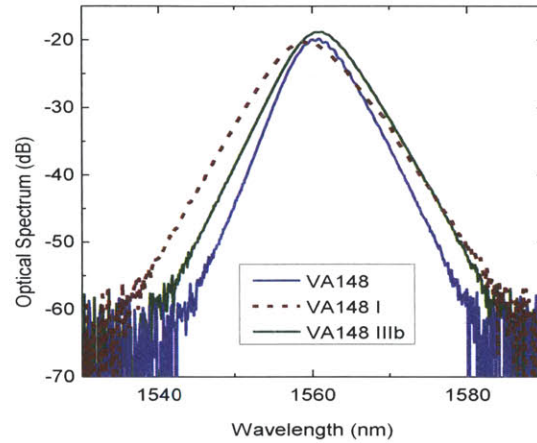
Figure 5-10: 625 MHz EDFL with free-space focusing on SBR with varying proton bombardment levels.

The optical performance of SBR VA86 PRC and VA148 PRC was compared in the 1 GHz EDFL (for EDFL set-up see Chapter 2). FWHM spectral bandwidths of 14 nm centered at 1569 nm with the VA86 PRC and 11 nm centered at 1567 nm for the VA148 PRC were obtained for comparable pump power levels, as shown in Fig. 5-11. The EDFL output power with SBR VA86 PRC was measured at 9.8 mW as compared to 11 mW for VA148 PRC. As the intracavity losses, which depend on the fiber birefringence and butt-coupling, might have slightly varied in both cases, the performance comparison did not lead to any preference of one absorber over the other. In particular, in the 1 GHz EDFL configuration, both absorbers were used interchangeably to achieve similar output characteristics.

5.3 Conclusion and Future Work

Optimizing SBR performance is crucial to obtain good optical performance for mode-locked laser configurations. Thus, a double-absorber SBR was presented and different modifications with a dielectric top-coating as well as reductions of lifetimes were analyzed. Extensive characterization and testing of these designed SBRs resulted in the demonstration of several high repetition rate GHz fiber lasers.
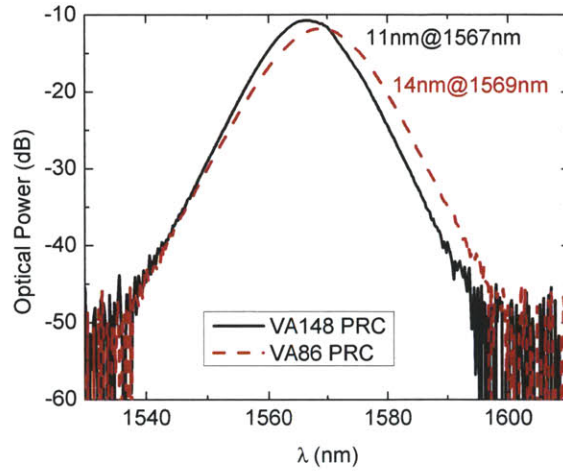
Figure 5-11: Mode-locking of 1 GHz EDFL with VA86PRC and VA148PRC.

Preliminary studies of unique oxidized saturable absorbers [129] in laser cavities, which combined the broadband reflectivity of a 7-pair oxidized mirror stack with an absorber, implied good optical performance. The reduced thickness of these absorbers can yield a smaller thermal load than the conventional 22-pair mirror stack. Therefore, recent achievements of large-scale oxidization in inverted mesa structures, where the whole surface has been oxidized (except for center spots of $\sim 12\,\mu m$ diameter, spaced apart by $150\,\mu m$, see [129]) constitute a promising path forward for new SBR designs. Furthermore, designs with an anti-resonant placement of the absorber layer could help mitigate thermal damage issues by increasing the saturation fluence. Another interesting aspect to be explored is combining dispersion compensation with saturable absorber properties.

Appendix A

Theory for Beam Divergence Simulations

In this thesis, the electric field profiles for multi-layered mirror structures in SBRs or thin-film output couplers were calculated. Therefore, the theoretical framework to determine the reflectivity and dispersion of any layered mirror stack is presented in the following. By combining a transformation matrix approach with Hankel transforms, one can evaluate the beam divergence effects in thin-film coatings. In the following, matrices and vectors are denoted in bold.

A.1 Thin-Film Coating Reflectivity

In a layered medium, multiple reflections occur at each layer interface, resulting in multiple forward and backward propagating electric field contributions. By introducing a propagation matrix approach, Kong [142] summarized the contribution of all forward and backward propagating waves for each medium and related them via boundary conditions to the electric field in the adjoining layer. This mathematical formalism can be used to determine the wave amplitudes in any region of the mirror stack with respect to the field in the neighboring layer.

Appendix A. Theory for Beam Divergence Simulations

If A and B denote the forward-propagating and backward-propagating electric fields, each field in layer $l+1$ can be expressed in terms of the electric field in the previous layer l (compare [142]).

$$A_{l+1} \cdot e^{j\ k_{l+1}\ d_l} = \frac{1 + \rho_{(l+1),l}}{2} \cdot \left[A_l e^{j\ k_l\ d_l} + R_{(l+1),l} \cdot B_l\ e^{-j\ k_l\ d_l} \right] \tag{A.1}$$

$$B_{l+1} \cdot e^{-j\ k_{l+1}\ d_l} = \frac{1 + \rho_{(l+1),l}}{2} \cdot \left[R_{(l+1),l} \cdot A_l e^{j\ k_l\ d_l} + B_l\ e^{-j\ k_l\ d_l} \right] \tag{A.2}$$

Here, $k_l = \dfrac{2\,\pi\,n_l}{\lambda} \cdot \cos(\theta)$ describes the wave-vector for a given angle of incidence θ at a wavelength λ and d_l represents the thickness of layer l. The refractive index n_l of the l-th layer $n_l = \sqrt{\epsilon_l\,\mu_l}$ is defined by material constants, the relative permittivity ϵ_l and relative permeability μ_l for the respective layer. The Fresnel reflection $R_{(l+1),l}$ coefficient can be determined as:

$$R_{(l+1),l} = \frac{1 - \rho_{(l+1),l}}{1 + \rho_{(l+1),l}} = -R_{l,(l+1)} \tag{A.3}$$

with

$$\rho_{(l+1),l,TE} = \frac{\mu_{l+1} \cdot k_l}{\mu_l \cdot k_{l+1}} = \frac{1}{\rho_{l,(l+1),TE}} \qquad \text{for TE waves} \tag{A.4}$$

$$\rho_{(l+1),l,TM} = \frac{\epsilon_l \cdot k_{l+1}}{\epsilon_{l+1} \cdot k_l} \qquad\qquad \text{for TM waves.} \tag{A.5}$$

Eq. A.1 and Eq. A.2 can be rewritten so that the following forward matrix equation governs the relationship between the consecutive electric fields:

$$\begin{bmatrix} A_{l+1} \\ B_{l+1} \end{bmatrix} = \mathbf{V}_{(l+1),l} \cdot \begin{bmatrix} A_l \\ B_l \end{bmatrix} \tag{A.6}$$

$$\mathbf{V}_{(l+1),l} = \frac{1 + \rho_{(l+1),l}}{2} \cdot \begin{bmatrix} e^{-j\ (k_{l+1} - k_l)\ d_l} & R_{(l+1),l} \cdot e^{-j\ (k_{l+1} + k_l)\ d_l} \\ R_{(l+1),l} \cdot e^{j\ (k_{l+1} + k_l)\ d_l} & e^{j\ (k_{l+1} - k_l)\ d_l} \end{bmatrix} \cdot$$
$$\tag{A.7}$$

As this matrix approach allows calculating the electric field based on the previous layer,

the electric field after propagation through the whole mirror stack, consisting of m layers, can be obtained by multiplying the respective matrices of all layers. At the same time, the equations can be rewritten to directly express the transmission T and reflectivity R for the whole mirror stack ($B_m = 0$):

$$\begin{bmatrix} T \\ 0 \end{bmatrix} = \mathbf{V}_{m,(m-1)} \cdot \mathbf{V}_{(m-1),(m-2)} \cdot \ldots \cdot \mathbf{V}_{2,1} \cdot \mathbf{V}_{1,0} \cdot \begin{bmatrix} 1 \\ R \end{bmatrix} = \mathbf{V}_{total} \cdot \begin{bmatrix} 1 \\ R \end{bmatrix} \tag{A.8}$$

with

$$T = \frac{A_m}{A_0} \quad \text{and} \quad R = \frac{B_0}{A_0}$$

Thus, the complex reflectivity R for the layer structure was derived in terms of the layer specific material constants and propagation wave vectors. In this notation, $\mathbf{V}_{total}$ denotes the resulting 2-by-2 matrix with individual single matrix elements $V_{total}(k, l)$ for $1 \leq k, l \leq 2$.

$$R = -\frac{V_{total}(2, 1)}{V_{total}(2, 2)} = R_{mirror}\, e^{j\, \phi_{mirror}} \tag{A.9}$$

A.2 Thin-Film Coating Reflectivity Incorporating Beam Divergence

The derivations presented so far were based on plane wave propagation in the layer stack. In order to evaluate beam dispersion effects, the spatial distribution of the light in each layer has to be incorporated into the calculations. Hankel transforms for radially symmetric beam profiles are therefore combined with the propagation matrix calculation approach presented earlier.

The p-th order Hankel Transform (HT) and the inverse Hankel Transform (ITH) for

Appendix A. Theory for Beam Divergence Simulations

cylindrical coordinates are defined in integral form as

$$F(\nu) = 2\pi \int_0^\infty f(r) \cdot J_p(2\pi\nu r) \, r \, dr \qquad \text{(HT)} \qquad \text{(A.10)}$$

$$f(r) = 2\pi \int_0^\infty F(\nu) \cdot J_p(2\pi r\nu) \, \nu \, d\nu \qquad \text{(IHT)}. \qquad \text{(A.11)}$$

Here, r denotes the spatial coordinate and ν the corresponding spatial frequency. Further, p describes the angular dependence of the wavefront $e^{jp\theta}$ and determines the order of the Bessel function J_p. For simplicity, the optical systems being considered are assumed to have a uniform phase profile along the azimuthal axis, equivalent to $p = 0$. In order to obtain a valid discretization of the Hankel Transform, the values of $f(r)$ have to be finite and have to extend to zero for large r. For each beam profile, the condition of $f(r \geq R) = 0$ for a spatial distribution with a maximum beam radius of R is met. R serves also as the truncated radius of the spatial variable $\mathbf{r}$ and sets the maximum window size, such that the input beam is divided into N slices along its radius vector $\mathbf{r}$. For this model, a quasi-discrete Hankel Transform [143, 144] is adapted for the numerical calculation.

The discretization of the spatial grid for discrete case is scaled with respect to the i-th root α_i of the Bessel function J_p to replace the infinite integral by a finite sum. As the space-bandwidth product S governs the limit V of the spatial frequency $S = 2\pi R V = \alpha_{p,N+1}$, this yields the following spatial and spatial frequency discretization for the i-th layer (assuming $p = 0$):

$$r_i = R \cdot \frac{\alpha_i}{\alpha_{N+1}} \qquad \text{for } 1 \leq i \leq N \qquad \text{(A.12)}$$

$$\nu_i = V \cdot \frac{\alpha_i}{\alpha_{N+1}} \qquad \text{for } 1 \leq i \leq N. \qquad \text{(A.13)}$$

The discretized HT and IHT can then be expressed, as shown in the following two

172

equations.

$$F_2(m) = \sum_{n=1}^{N} T_{mn} \, F_1(n), \qquad \qquad \text{for } 1 \leq m \leq N \qquad \qquad \text{(A.14)}$$

$$F_1(n) = \sum_{m=1}^{N} T_{nm} \, F_2(m) \qquad \qquad \text{for } 1 \leq n \leq N. \qquad \qquad \text{(A.15)}$$

For $p = 0$, the transformation matrix $\mathbf{T}$ is defined by the individual matrix elements $T_{m,n}$:

$$T_{mn} = \frac{2 \, J_0 \left(\alpha_n \, \alpha_m / \alpha_{N+1} \right)}{|J_1(\alpha_n)| \, |J_1(\alpha_m)| \, \alpha_{N+1}} \qquad \qquad \text{for } 1 \leq n, m \leq N. \qquad \qquad \text{(A.16)}$$

In order to transfer this methodology to the thin-film simulation, a Gaussian beam profile is assumed for an input beam vector $\mathbf{A}_0$ with components $A_{0,i} = e^{(-r_i^2/\omega_0^2)}$ that is evaluated at radial points, as discretized in Eq. A.12. The column vector $\mathbf{u}$ contains elements of u_i, as defined in Eq. A.17. The vector $\mathbf{u}$ scales each beam amplitude element with the Bessel function at the corresponding root.

$$u_i = \frac{|J_i(\alpha_i)|}{R} \qquad \qquad \text{for } 1 \leq i \leq N \qquad \qquad \text{(A.17)}$$

$$B_i = \frac{A_{0,i}}{u_i} \qquad \qquad \text{(A.18)}$$

The discretized Hankel transform is applied by multiplying the transformation matrix $\mathbf{T}$ with the scaled input beam vector $\mathbf{B}$, according to $\mathbf{A}_k = \mathbf{T} \cdot \mathbf{B}$. Here, $\mathbf{A}_k$ is a vector where the subscript k denotes that the vector is represented in the frequency domain.

By evaluating the thin-film reflectivity in each beam slice for the respective spatial frequency/k-vector ν_j and by recording the individual contributions in the matrix $\mathbf{R}_{mat}$, the impact of the beam divergence can be derived by multiplication in the spatial frequency domain: $\mathbf{B}_{out,k} = \mathbf{R}_{mat} \cdot \mathbf{A}_k$. Introducing the vector $\mathbf{A}_{out,k} = \mathbf{B}_{out,k}/ \, \mathbf{u}$, where element by element division is applied, $A_{out,k,i} = B_{out,k,i}/ \, u_i$, the inverse Hankel transform $\mathbf{A}_{out} = \mathbf{T} \cdot \mathbf{A}_{out,k}$ leads to the desired beam profile result, which accounts for propagation through the thin-film coating and beam divergence effects.

Appendix A. Theory for Beam Divergence Simulations

Bibliography

[1] C. V. Shank and E. P. Ippen, "Subpicosecond kilowatt pulses from a mode-locked cw dye laser," *Applied Physics Letters*, vol. 24, no. 8, pp. 373–375, apr 1974.

[2] L. F. Mollenauer and R. H. Stolen, "The soliton laser," *Opt. Lett.*, vol. 9, no. 1, pp. 13–15, Jan 1984. [Online]. Available: http://ol.osa.org/abstract.cfm?URI=ol-9-1-13

[3] D. E. Spence, P. N. Kean, and W. Sibbett, "60-fsec pulse generation from a self-mode-locked Ti:sapphire laser," *Optics Letters*, vol. 16, no. 1, pp. 42 – 44, 1991.

[4] F. X. Kaertner, U. Morgner, T. Schibli, R. Ell, H. A. Haus, J. G. Fujimoto, and E. P. Ippen, *Topics in Applied Physics: Few-Cycle Laser Pulse Generation and Its Applications*. Berlin Heidelberg: Springer, 2004, vol. 95, ch. Few-Cycle Pulses Directly from a Laser, pp. 73 – 136.

[5] U. Keller, "Recent developments in compact ultrafast lasers," *Nature*, vol. 424, pp. 831 – 838, 2003.

[6] C. Rullière, *Femtosecond Laser Pulses*. Heidelberg: Springer, 1998.

[7] C. Shank, E. Ippen, and R. Bersohn, "Time-resolved spectroscopy of hemoglobin and its complexes with subpicosecond optical pulses," *Science*, vol. 193, no. 4247, pp. 50–51, 1976. [Online]. Available: http://www.sciencemag.org/content/193/4247/50.abstract

[8] C. Shank, E. Ippen, and O. Teschke, "Sub-picosecond relaxation of large organic molecules in solution," *Chemical Physics Letters*, vol. 45, no. 2, pp. 291 – 294, 1977. [Online]. Available: http://www.sciencedirect.com/science/article/pii/0009261477802728

[9] D. Du, X. Liu, G. Korn, J. Squier, and G. Mourou, "Laser-induced breakdown by impact ionization in SiO_2 with pulse widths from 7 ns to 150 fs," *Applied Physics Letters*, vol. 64, no. 23, pp. 3071–3073, jun 1994.

[10] R. R. Gattass and E. Mazur, "Femtosecond laser micromachining in transparent materials," *Nature Photonics*, vol. 2, no. 4, pp. 219–225, Apr. 2008. [Online]. Available: http://www.nature.com/nphoton/journal/v2/n4/abs/nphoton.2008.47.html

[11] D. J. Jones, S. A. Diddams, J. K. Ranka, A. Stentz, R. S. Windeler, J. L. Hall, and S. T. Cundiff, "Carrier-Envelope Phase Control of Femtosecond Mode-Locked Lasers and Direct Optical Frequency Synthesis," *Science*, vol. 288, pp. 635 – 639, 2000.

[12] S. T. Cundiff, "Metrology: New generation of combs," *Nature*, vol. 450, no. 7173, pp. 1175–1176, Dec. 2007. [Online]. Available: http://dx.doi.org/10.1038/4501175b

[13] P. Juodawlkis, J. C. Twichell, G. E. Betts, J. J. Hargreaves, R. D. Younger, J. L. Wasserman, F. J. O'Donnell, K. G. Ray, and R. C. Williamson, "Optically sampled analog-to-digital converters," *IEEE Trans. Microwave Theory Tech*, vol. 49, no. 10, p. 1840, 2001.

[14] R. Walden, "Analog-to-digital converter survey and analysis," *IEEE Journal on Selected Areas in Communications*, vol. 17, no. 4, pp. 539–550, 1999.

[15] G. C. Valley, "Photonic analog-to-digital converters," *Opt. Express*, vol. 15, no. 5, pp. 1955–1982, 2007. [Online]. Available: http://www.opticsexpress.org/abstract.cfm?URI=oe-15-5-1955

[16] F. X. Kärtner, J. Kim, J. Chen, and A. Khilo, "Photonic Analog-to-Digital Conversion with femtosecond lasers," *Frequenz*, vol. 62, pp. 7–8, 2008.

[17] A. M. Weiner, "Femtosecond pulse shaping using spatial light modulators," *Review of Scientific Instruments*, vol. 71, no. 5, pp. 1929–1960, 2000. [Online]. Available: http://link.aip.org/link/?RSI/71/1929/1

[18] E. Ippen, "Clocks, combs and optical arbitrary waveforms," in *IEEE International Topical Meeting on Microwave Photonics*, Oct. 2007, p. 45.

[19] E. Ippen, A. Benedick, J. Birge, H. Byun, L.-J. Chen, G. Chang, D. Chao, J. Morse, A. Motamedi, M. Sander, G. Petrich, L. Kolodziejski, and F. Kärtner, "Optical arbitrary waveform generation," in *Quantum Electronics and Laser Science Conference*. Optical Society of America, 2010, p. JThC4. [Online]. Available: http://www.opticsinfobase.org/abstract.cfm?URI=QELS-2010-JThC4

[20] M. T. Murphy, T. Udem, R. Holzwarth, A. Sizmann, L. Pasquini, C. Araujo-Hauck, H. Dekker, S. D'Odorico, M. Fischer, T. W. Hnsch, and A. Manescau, "High-precision wavelength calibration of astronomical spectrographs with laser frequency combs," *Monthly Notices of the Royal Astronomical Society*, vol. 380, no. 2, pp. 839–847, Sep. 2007. [Online]. Available: http://onlinelibrary.wiley.com/doi/10.1111/j.1365-2966.2007.12147.x/full

[21] C. Li, A. J. Benedick, P. Fendel, A. G. Glenday, F. X. Kärtner, D. F. Phillips, D. Sasselov, A. Szentgyorgyi, and R. L. Walsworth, "A laser frequency comb that enables radial velocity measurements with a precision of $1\,\mathrm{cm\,s^{-1}}$," *Nature*, vol. 452, no. 7187, pp. 610–612, Apr. 2008. [Online]. Available: http://dx.doi.org/10.1038/nature06854

176

[22] T. Steinmetz, T. Wilken, C. Araujo-Hauck, R. Holzwarth, T. W. Hnsch, L. Pasquini, A. Manescau, S. D'Odorico, M. T. Murphy, T. Kentischer, W. Schmidt, and T. Udem, "Laser frequency combs for astronomical observations," *Science*, vol. 321, no. 5894, pp. 1335–1337, 2008. [Online]. Available: http://www.sciencemag.org/content/321/5894/1335.abstract

[23] Z. Jiang, C.-B. Huang, D. E. Leaird, and A. M. Weiner, "Optical arbitrary waveform processing of more than 100 spectral comb lines," *Nature Photonics*, vol. 1, pp. 463–467, 2007. [Online]. Available: http://www.nature.com/nphoton/journal/v1/n8/abs/nphoton.2007.139.html

[24] J. A. Salehi, "Emerging OCDMA communication systems and data networks," *J. Opt. Netw.*, vol. 6, no. 9, pp. 1138–1178, Sep 2007. [Online]. Available: http://jon.osa.org/abstract.cfm?URI=jon-6-9-1138

[25] J. Cao, R. Broeke, N. Fontaine, C. Ji, Y. Du, N. Chubun, K. Aihara, A.-V. Pham, F. Olsson, S. Lourdudoss, and S. Yoo, "Demonstration of spectral phase O-CDMA encoding and decoding in monolithically integrated arrayed-waveguide-grating-based encoder," *Photonics Technology Letters, IEEE*, vol. 18, no. 24, pp. 2602–2604, Dec. 15, 2006.

[26] C. W. Holzwarth, R. Amatya, M. Araghchini, J. Birge, H. Byun, J. Chen, M. Dahlem, N. A. DiLello, F. Gan, J. L. Hoyt, E. P. Ippen, F. X. Kärtner, A. Khilo, J. Kim, M. Kim, A. Motamedi, J. S. Orcutt, M. Park, M. Perrott, M. A. Popovic, R. J. Ram, H. I. Smith, G. R. Zhou, S. J. Spector, T. M. Lyszczarz, M. W. Geis, D. M. Lennon, J. U. Yoon, M. E. Grein, R. T. Schulein, S. Frolov, A. Hanjani, and J. Shmulovich, "High speed analog-to-digital conversion with silicon photonics," in *Proc. SPIE 7220, Photonics West, San Jose, CA*, Jan. 2009.

[27] A. Khilo, S. J. Spector, M. E. Grein, A. H. Nejadmalayeri, C. W. Holzwarth, M. Y. Sander, M. S. Dahlem, M. Y. Peng, M. W. Geis, N. A. DiLello, J. U. Yoon, A. Motamedi, J. S. Orcutt, J. P. Wang, C. M. Sorace-Agaskar, M. A. Popović, J. Sun, G.-R. Zhou, H. Byun, J. Chen, J. L. Hoyt, H. I. Smith, R. J. Ram, M. Perrott, T. M. Lyszczarz, E. P. Ippen, and F. X. Kärtner, "Photonic ADC: overcoming the bottleneck of electronic jitter," *Opt. Express*, vol. 20, no. 4, pp. 4454–4469, Feb 2012. [Online]. Available: http://www.opticsexpress.org/abstract.cfm?URI=oe-20-4-4454

[28] J. Kim and F. Kärtner, "Attosecond-precision ultrafast photonics," *Laser and Photonics Reviews*, vol. 4, pp. 432–456, 2010.

[29] J. Kim, M. J. Park, M. H. Perrott, and F. X. Kärtner, "Photonic subsampling analog-to-digital conversion of microwave signals at 40-GHz with higher than 7-ENOB resolution," *Opt. Express*, vol. 16, no. 21, pp. 16509–16515, 2008. [Online]. Available: http://www.opticsexpress.org/abstract.cfm?URI=oe-16-21-16509

[30] M. E. Grein, S. Spector, A. Khilo, A. H. Nejadmalayeri, M. Y. Sander, M. Peng, J. Wang, C. M. Sorace, M. W. Geis, M. M. Willis, D. M. Lennon, T. Lyszczarz, E. P. Ippen, and F. X. Kaertner, "Demonstration of a 10 GHz CMOS-compatible integrated photonic analog-to-digital converter," in *CLEO:2011 - Laser Applications to Photonic Applications.* Optical Society of America, 2011, p. CThI1. [Online]. Available: http://www.opticsinfobase.org/abstract.cfm?URI=CLEO:SandI-2011-CThI1

[31] E. P. Ippen, "Principles of passive mode locking," *Appl. Phys. B*, vol. 58, pp. 158–170, 1994.

[32] H. Haus, "Theory of mode locking with a fast saturable absorber," *Journal of Applied Physics*, vol. 46, no. 7, pp. 3049 – 3058, 1975.

[33] E. P. Ippen, H. A. Haus, and L. Y. Liu, "Additive pulse mode locking," *J. Opt. Soc. Am. B*, vol. 6, no. 9, pp. 1736–1745, 1989.

[34] H. Haus, "Theory of mode locking with a slow saturable absorber," *IEEE Journal of Quantum Electronics*, vol. QE-11, no. 9, pp. 736 – 746, 1975.

[35] R. Paschotta and U. Keller, "Passive mode locking with slow saturable absorbers," *Appl. Phys. B*, vol. 73, no. 7, p. 653, 2001.

[36] F. X. Kärtner, I. D. Jung, and U. Keller, "Soliton mode-locking with saturable absorbers," *IEEE J. of Selected Topics in Quantum Electronics*, vol. 2, no. 3, pp. 540–556, 1996.

[37] D. Pudo, H. Byun, J. Chen, J. Sickler, F. X. Kärtner, and E. P. Ippen, "Scaling of passively mode-locked soliton erbium waveguide lasers based on slow saturable absorbers," *Opt. Express*, vol. 16, no. 23, pp. 19 221–19 231, 2008. [Online]. Available: http://www.opticsexpress.org/abstract.cfm?URI=oe-16-23-19221

[38] L. F. Mollenauer and R. H. Stolen, "The soliton laser," *Opt. Lett.*, vol. 9, no. 1, pp. 13–15, 1984. [Online]. Available: http://ol.osa.org/abstract.cfm?URI=ol-9-1-13

[39] M. Y. Sander, J. Birge, A. Benedick, H. M. Crespo, and F. X. Kärtner, "Dynamics of dispersion managed octave-spanning titanium:sapphire lasers," *Journal of the Optical Society of America B*, vol. 26, no. 4, pp. 743–749, Apr. 2009. [Online]. Available: http://josab.osa.org/abstract.cfm?URI=josab-26-4-743

[40] M. Y. Sander, E. P. Ippen, and F. X. Kärtner, "Carrier-envelope phase dynamics of octave-spanning dispersion-managed Ti: sapphire lasers," *Optics Express*, vol. 18, no. 5, pp. 4948–4960, Mar. 2010.

[41] L. Chen, M. Y. Sander, and F. X. Kärtner, "Kerr-lens mode locking with minimum nonlinearity using gain-matched output couplers," *Optics Letters*, vol. 35, no. 17, pp. 2916–2918, 2010.

[42] F. X. Kärtner and U. Keller, "Stabilization of solitonlike pulses with a slow saturable absorber," *Opt. Lett.*, vol. 20, no. 1, pp. 16–18, 1995. [Online]. Available: http://ol.osa.org/abstract.cfm?URI=ol-20-1-16

[43] S. Tsuda, W. H. Knox, S. T. Cundiff, W. Y. Jan, and J. E. Cunningham, "Mode-locking ultrafast solid-state lasers with saturable Bragg reflectors," *IEEE J. Sel. Topics in Quantum Electronics*, vol. 2, pp. 454–464, 1996.

[44] O. Okhotnikov, A. Grudinin, and M. Pessa, "Ultra-fast fibre laser systems based on SESAM technology: new horizons and applications," *New Journal of Physics*, vol. 6, no. 1, p. 177, 2004. [Online]. Available: http://stacks.iop.org/1367-2630/6/i=1/a=177

[45] S. Yamashita, Y. Inoue, S. Maruyama, Y. Murakami, H. Yaguchi, M. Jablonski, and S. Y. Set, "Saturable absorbers incorporating carbon nanotubes directly synthesized onto substrates and fibers and their application to mode-locked fiber lasers," *Opt. Lett.*, vol. 29, no. 14, pp. 1581–1583, Jul 2004. [Online]. Available: http://ol.osa.org/abstract.cfm?URI=ol-29-14-1581

[46] S. Y. Set, H. Yaguchi, Y. Tanaka, and M. Jablonski, "Laser mode locking using a saturable absorber incorporating carbon nanotubes," *J. Lightwave Technol.*, vol. 22, no. 1, p. 51, Jan 2004. [Online]. Available: http://jlt.osa.org/abstract.cfm?URI=jlt-22-1-51

[47] K. Kieu and M. Mansuripur, "Femtosecond laser pulse generation with a fiber taper embedded in carbon nanotube/polymer composite," *Opt. Lett.*, vol. 32, no. 15, pp. 2242–2244, Aug 2007. [Online]. Available: http://ol.osa.org/abstract.cfm?URI=ol-32-15-2242

[48] F. Shohda, T. Shirato, M. Nakazawa, J. Mata, and J. Tsukamoto, "147 fs, 51 MHz soliton fiber laser at 1.56 μm with a fiber-connector-type SWNT/P3HT saturable absorber," *Opt. Express*, vol. 16, no. 25, pp. 20943–20948, Dec 2008. [Online]. Available: http://www.opticsexpress.org/abstract.cfm?URI=oe-16-25-20943

[49] S. Zeller, T. Sudmeyer, K. Weingarten, and U. Keller, "Passively modelocked 77 GHz Er:Yb:glass laser," *Electronics Letters*, vol. 43, no. 1, pp. 32–33, 4 2007.

[50] A. E. Oehler, T. Südmeyer, K. J. Weingarten, and U. Keller, "100 GHz passively mode-locked Er:Yb:glass laser at 1.5 μm with 1.6-ps pulses," *Opt. Express*, vol. 16, no. 26, pp. 21930–21935, Dec 2008. [Online]. Available: http://www.opticsexpress.org/abstract.cfm?URI=oe-16-26-21930

[51] K. S. Abedin, M. Hyodo, and N. Onodera, "Active stabilization of a higher-order mode-locked fiber laser operating at a pulse-repetition rate of 154 GHz," *Opt. Lett.*, vol. 26, no. 3, pp. 151–153, Feb 2001. [Online]. Available: http://ol.osa.org/abstract.cfm?URI=ol-26-3-151

[52] J. J. McFerran, L. Nenadovic, W. C. Swann, J. B. Schlager, and N. R. Newbury, "A passively mode-locked fiber laser at 1.54 μm with a fundamental repetition frequency reaching 2 GHz," *Optics Express*, vol. 15, no. 20, pp. 13 155–13 166, Oct. 2007. [Online]. Available: http://www.opticsexpress.org/abstract.cfm?URI=oe-15-20-13155

[53] J. Chen, J. W. Sickler, H. Byun, E. P. Ippen, S. Jiang, and F. X. Kärtner, "Fundamentally mode-locked 3 GHz femtosecond Erbium fiber laser," in *Ultrafast Phenomena XVI*. Springer Berlin Heidelberg, 2009, vol. 92, pp. 732–734.

[54] S. Yamashita, Y. Inoue, K. Hsu, T. Kotake, H. Yaguchi, D. Tanaka, M. Jablonski, and S. Set, "5-GHz pulsed fiber Fabry-Perot laser mode-locked using carbon nanotubes," *Photonics Technology Letters, IEEE*, vol. 17, no. 4, pp. 750–752, 2005.

[55] A. Martinez, K. Fuse, and S. Yamashita, "10 GHz pulsed Er-Yb fiber laser using an optically deposited carbon-nanotube film in a fiber mirror," in *Conference on Lasers and Electro-Optics*. Optical Society of America, 2010, p. CTuII5. [Online]. Available: http://www.opticsinfobase.org/abstract.cfm?URI=CLEO-2010-CTuII5

[56] H. Byun, D. Pudo, J. Chen, E. P. Ippen, and F. X. Kärtner, "High-repetition-rate, 491 MHz, femtosecond fiber laser with low timing jitter," *Opt. Lett.*, vol. 33, no. 19, pp. 2221–2223, 2008. [Online]. Available: http://ol.osa.org/abstract.cfm?URI=ol-33-19-2221

[57] A. M. Smith, "Birefringence induced by bends and twists in single-mode optical fiber," *Applied Optics*, vol. 19, no. 15, p. 26062611, 1980.

[58] D. N. Christodoulides and R. I. Joseph, "Vector solitons in birefringent nonlinear dispersive media," *Opt. Lett.*, vol. 13, no. 1, pp. 53–55, 1988. [Online]. Available: http://ol.osa.org/abstract.cfm?URI=ol-13-1-53

[59] D. B. Leviton and B. J. Frey, "Temperature-dependent absolute refractive index measurements of synthetic fused silica," in *Proc. SPIE 6273*, May 2006. [Online]. Available: http://arxiv.org/abs/0805.0091

[60] S. Cundiff, B. Collings, and W. Knox, "Polarization locking in an isotropic, mode-locked soliton Er/Yb fiber laser," *Optics Express*, vol. 1, no. 1, p. 1221, 1997.

[61] N. N. Akhmediev, J. M. Soto-Crespo, S. T. Cundiff, B. C. Collings, and W. H. Knox, "Phase locking and periodic evolution of solitons in passively mode-locked fiber lasers with a semiconductor saturable absorber," *Optics letters*, vol. 23, no. 11, p. 852854, 1998.

[62] I. P. T. Institute, http://www.ioffe.ru/SVA/NSM/Semicond/GaAs/thermal.html.

[63] T. C. of Common Materials, http://www.engineeringtoolbox.com/thermal-conductivity-d_429.html.

[64] L. Li, H. Li, T. Qiu, V. L. Temyanko, M. M. Morrell, A. Schülzgen, A. Mafi, J. V. Moloney, and N. Peyghambarian, "3-Dimensional thermal analysis and active cooling of short-length high-power fiber lasers," *Optics Express*, vol. 13, no. 9, pp. 3420–3428, May 2005. [Online]. Available: http://www.opticsexpress.org/abstract.cfm?URI=oe-13-9-3420

[65] D. Brown and H. Hoffman, "Thermal, stress, and thermo-optic effects in high average power double-clad silica fiber lasers," *Quantum Electronics, IEEE Journal of*, vol. 37, no. 2, pp. 207 –217, feb 2001.

[66] Y. O. Barmenkov, A. V. Kir'yanov, and M. V. Andrés, "Resonant and thermal changes of refractive index in a heavily doped erbium fiber pumped at wavelength 980 nm," *Applied Physics Letters*, vol. 85, no. 13, pp. 2466–2468, 2004. [Online]. Available: http://link.aip.org/link/?APL/85/2466/1

[67] T. Liu, Z. M. Yang, and S. H. Xu, "3-dimensional heat analysis in short-length Er^{3+}/Yb^{3+} co-doped phosphate fiber laser with upconversion," *Opt. Express*, vol. 17, no. 1, pp. 235–247, Jan 2009. [Online]. Available: http://www.opticsexpress.org/abstract.cfm?URI=oe-17-1-235

[68] C. Saraceno, C. Schriber, M. Mangold, M. Hoffmann, O. Heckl, C. Baer, M. Golling, T. Südmeyer, and U. Keller, "Sesams for high-power oscillators: Design guidelines and damage thresholds," *Selected Topics in Quantum Electronics, IEEE Journal of*, vol. 18, no. 1, pp. 29 –41, Jan.-Feb. 2012.

[69] R. Paschotta, "Timing jitter and phase noise of mode-locked fiber lasers," *Opt. Express*, vol. 18, no. 5, pp. 5041–5054, Mar 2010. [Online]. Available: http://www.opticsexpress.org/abstract.cfm?URI=oe-18-5-5041

[70] A. B. Grudinin, D. J. Richardson, and D. N. Payne, "Passive harmonic modelocking of a fibre soliton ring laser," *Electronics Letters*, vol. 29, no. 21, pp. 1860–1861, Oct. 1993.

[71] B. C. Collings, K. Bergman, and W. H. Knox, "Stable multigigahertz pulse-train formation in a short-cavity passively harmonic mode-locked erbium/ytterbium fiber laser," *Optics Letters*, vol. 23, no. 2, pp. 123–125, Jan. 1998. [Online]. Available: http://ol.osa.org/abstract.cfm?URI=ol-23-2-123

[72] S. Zhou, D. G. Ouzounov, and F. W. Wise, "Passive harmonic mode-locking of a soliton Yb fiber laser at repetition rates to 1.5 GHz," *Optics Letters*, vol. 31, no. 8, pp. 1041–1043, Apr. 2006. [Online]. Available: http://ol.osa.org/abstract.cfm?URI=ol-31-8-1041

[73] J. Kutz, B. Collings, K. Bergman, and W. Knox, "Stabilized pulse spacing in soliton lasers due to gain depletion and recovery," *Quantum Electronics, IEEE Journal of*, vol. 34, no. 9, pp. 1749 –1757, Sept. 1998.

[74] K. S. Abedin, J. T. Gopinath, L. A. Jiang, M. E. Grein, H. A. Haus, and E. P. Ippen, "Self-organization of harmonic pulses in a passively modelocked stretched pulse erbium fiber ring laser," in *The 15th Annual Meeting of the IEEE Lasers and Electro-Optics Society, 2002. LEOS 2002*, vol. 2. IEEE, Nov. 2002, pp. 465– 466 vol.2.

[75] Y. Deng and W. H. Knox, "Self-starting passive harmonic mode-locked femtosecond Yb^{3+}-doped fiber laser at 1030 nm," *Optics Letters*, vol. 29, no. 18, pp. 2121–2123, 2004. [Online]. Available: http://ol.osa.org/abstract.cfm?URI=ol-29-18-2121

[76] T. Schibli, E.R.Thoen, F. Kärtner, and E. Ippen, "Suppression of Q-switched mode locking and break-up into multiple pulses by inverse saturable absorption," *Appl. Phys. B*, vol. 70, pp. S41–S49, 2000.

[77] Y. Song, K. Jung, and J. Kim, "Impact of pulse dynamics on timing jitter in mode-locked fiber lasers," *Opt. Lett.*, vol. 36, no. 10, pp. 1761–1763, May 2011. [Online]. Available: http://ol.osa.org/abstract.cfm?URI=ol-36-10-1761

[78] B. C. Stuart, M. D. Feit, S. Herman, A. M. Rubenchik, B. W. Shore, and M. D. Perry, "Nanosecond-to-femtosecond laser-induced breakdown in dielectrics," *Physical Review B*, vol. 53, no. 4, pp. 1749–1761, Jan. 1996. [Online]. Available: http://link.aps.org/doi/10.1103/PhysRevB.53.1749

[79] L. A. Emmert, M. Mero, and W. Rudolph, "Modeling the effect of native and laser-induced states on the dielectric breakdown of wide band gap optical materials by multiple subpicosecond laser pulses," *Journal of Applied Physics*, vol. 108, no. 4, pp. 043 523–043 523–7, Aug. 2010. [Online]. Available: http://jap.aip.org/resource/1/japiau/v108/i4/p043523_s1

[80] J. Bonse, S. Baudach, W. Kautek, E. Welsch, and J. Kruger, "Femtosecond laser damage of a high reflecting mirror," *Thin Solid Films*, vol. 408, no. 1, pp. 297–301, 2002.

[81] J. Jasapara, A. Nampoothiri, W. Rudolph, D. Ristau, and K. Starke, "Femtosecond laser pulse induced breakdown in dielectric thin films," *Physical Review B*, vol. 63, no. 1, pp. 045 117–1 – 045 117–5, 2001.

[82] A. Borowiec, M. MacKenzie, G. Weatherly, and H. Haugen, "Femtosecond laser pulse ablation of GaAs and InP: studies utilizing scanning and transmission electron microscopy," *Applied Physics A: Materials Science Processing*, vol. 77, pp. 411–417, 2003.

[83] H. Qi, Q. Wang, X. Zhang, Z. Liu, S. Zhang, J. Chang, W. Xia, and G. Jin, "Theoretical and experimental study of laser induced damage on GaAs by nanosecond pulsed irradiation," *Optics and Lasers in Engineering*, vol. 49, no. 2, pp. 285–291, Feb. 2011. [Online]. Available: http://www.sciencedirect.com/science/article/pii/S0143816610002265

[84] L. Huang, J. P. Callan, E. N. Glezer, and E. Mazur, "GaAs under intense ultrafast excitation: Response of the dielectric function," *Phys. Rev. Lett.*, vol. 80, pp. 185–188, Jan 1998. [Online]. Available: http://link.aps.org/doi/10.1103/PhysRevLett.80.185

[85] B. J., B. S., K. W., W. E., and K. J., "Femtosecond laser damage of a high reflecting mirror," *Thin Solid Films*, vol. 408, no. 1, pp. 297–301, 2002.

[86] D. Chao, M. Y. Sander, G. Chang, J. L. Morse, J. A. Cox, G. S. Petrich, L. A. Kolodziejski, F. X. Kärtner, and E. P. Ippen, "Self-referenced erbium fiber laser frequency comb at a GHz repetition rate," in *Optical Fiber Communications Conference (OFC)*, 2012, p. OW1C.2.

[87] D. Chao, "Self-referenced $1.5\,\mu$m fiber frequency combs at GHz repetition rates," Ph.D. dissertation, Massachusetts Institute of Technology, 2012.

[88] A. Bartels, S. A. Diddams, C. W. Oates, G. Wilpers, J. C. Bergquist, W. H. Oskay, and L. Hollberg, "Femtosecond-laser-based synthesis of ultrastable microwave signals from optical frequency references," *Optics Letters*, vol. 30, no. 6, pp. 667–669, Mar. 2005. [Online]. Available: http://ol.osa.org/abstract.cfm?URI=ol-30-6-667

[89] J. Millo, R. Boudot, M. Lours, P. Y. Bourgeois, A. N. Luiten, Y. L. Coq, Y. Kersal, and G. Santarelli, "Ultra-low-noise microwave extraction from fiber-based optical frequency comb," *Optics Letters*, vol. 34, no. 23, pp. 3707–3709, Dec. 2009. [Online]. Available: http://ol.osa.org/abstract.cfm?URI=ol-34-23-3707

[90] F. Quinlan, T. M. Fortier, M. S. Kirchner, J. A. Taylor, M. J. Thorpe, N. Lemke, A. D. Ludlow, Y. Jiang, C. W. Oates, and S. A. Diddams, "Ultralow phase noise microwave generation with an Er:fiber-based optical frequency divider," *1105.1434*, May 2011. [Online]. Available: http://arxiv.org/abs/1105.1434

[91] S. A. Diddams, M. Kirchner, T. Fortier, D. Braje, A. M. Weiner, and L. Hollberg, "Improved signal-to-noise ratio of 10 GHz microwave signals generated with a mode-filtered femtosecond laser frequency comb," *Optics Express*, vol. 17, no. 5, pp. 3331–3340, Mar. 2009. [Online]. Available: http://www.opticsexpress.org/abstract.cfm?URI=oe-17-5-3331

[92] M. Kuznetsov, "Cascaded coupler Mach-Zehnder channel dropping filters for wavelength-division-multiplexed optical systems," *Lightwave Technology, Journal of*, vol. 12, no. 2, pp. 226–230, 1994.

[93] X. Liu, C. Yu, Z. Zeng, and L. Liu, "Design and applications of planar waveguide interleaving filters," in *Proceedings of SPIE - The International Society for Optical Engineering*, vol. 5623, 2004, pp. 594–604. [Online]. Available: http://www.scopus.com/inward/record.url?eid=2-s2.0-17644421784&partnerID=40&md5=35879c2c921221ca965bb03e3db557a6

[94] M. Oguma, T. Kitoh, Y. Inoue, T. Mizuno, T. Shibata, M. Kohtoku, and Y. Hibino, "Compact and low-loss interleave filter employing lattice-form structure and silica-based waveguide," *Lightwave Technology, Journal of*, vol. 22, no. 3, pp. 895–902, 2004.

[95] T. Chiba, "Waveguide interleaving filters," in *Proceedings of SPIE*, Orlando, FL, USA, 2003, pp. 532–538. [Online]. Available: http://spie.org/x648.html?product_id=514003

[96] S. Cao, J. Chen, J. Damask, C. Doerr, L. Guiziou, G. Harvey, Y. Hibino, H. Li, S. Suzuki, K. Wu, and P. Xie, "Interleaver technology: Comparisons and applications requirements," *Journal of Lightwave Technology*, vol. 22, no. 1, pp. 281–289, 2004. [Online]. Available: http://www.scopus.com/inward/record.url?eid= 2-s2.0-10744223696&partnerID=40&md5=ceeb7247aea2fd4e8afa7d70ae9a4f8e

[97] M. Kawachi, "Silica waveguides on silicon and their application to integrated-optic components," *Optical and Quantum Electronics*, vol. 22, no. 5, pp. 391–416, Sep. 1990. [Online]. Available: http://www.springerlink.com/content/l18750h32743h70l/

[98] H. G. Weber and M. Nagazawa, *Ultrahigh-Speed Optical Transmission Technology*. Springer, 2007.

[99] P. Guan, T. Hirano, K. Harako, Y. Tomoyama, T. Hirooka, and M. Nagazawa, "2.56 Tbit/s/ch polarization-multiplexed DQPSK transmission over 300 km using time-domain optical Fourier transformation," in *ECOC Technical Digest*, 2011, p. We.10.P1.80.

[100] H. Byun, D. Pudo, S. Frolov, A. Hanjani, J. Shmulovich, E. P. Ippen, and F. X. Kärtner, "Integrated 2 GHz femtosecond laser based on a planar Er-doped lightwave circuit," in *Lasers and Electro-Optics (CLEO) and Quantum Electronics and Laser Science Conference (QELS), Conference on*, 2010.

[101] M. Y. Sander, H. Byun, J. Morse, D. Chao, H. M. Shen, A. Motamedi, G. Petrich, L. Kolodziejski, E. P. Ippen, and F. X. Kärtner, "1 GHz femtosecond erbium-doped fiber lasers," in *Conference on Lasers and Electro-Optics (CLEO) and Quantum Electronics and Laser Science Conference (QELS)*, 2010.

[102] H. Byun, M. Y. Sander, A. Motamedi, H. Shen, G. S. Petrich, L. A. Kolodziejski, E. P. Ippen, and F. X. Kärtner, "Compact, stable 1 GHz femtosecond Er-doped fiber lasers," *Appl. Opt.*, vol. 49, no. 29, pp. 5577–5582, 2010. [Online]. Available: http://ao.osa.org/abstract.cfm?URI=ao-49-29-5577

[103] M. Y. Sander, H. Byun, M. Dahlem, D. Chao, A. R. Motamedi, G. Petrich, L. Kolodziejski, S. Frolov, H. Hao, J. Shmulovich, E. P. Ippen, and F. X. Kärtner, "10 GHz waveguide interleaved femtosecond pulse train," in *CLEO:2011 - Laser Applications to Photonic Applications*. Optical Society of America, 2011, p. CThY6. [Online]. Available: http://www.opticsinfobase.org/abstract.cfm?URI= CLEO:SandI-2011-CThY6

[104] T. Zhang, K. Chen, and Q. Sheng, "A novel interleaver based on dual-pass Mach-Zehnder interferometer," *Microwave and Optical Technology Letters*, vol. 42, no. 3, pp. 253–255, Aug. 2004. [Online]. Available: http://onlinelibrary.wiley.com/doi/10.1002/mop.20268/abstract

[105] H. Byun, D. Pudo, S. Frolov, A. Hanjani, J. Shmulovich, E. P. Ippen, and F. X. Kärtner, "Integrated Low-Jitter 400-MHz femtosecond waveguide laser," *IEEE Photonics Technology Letters*, vol. 21, no. 12, pp. 763–765, 2009. [Online]. Available: http://ieeexplore.ieee.org/lpdocs/epic03/wrapper.htm?arnumber=4806035

[106] J. D. Bradley and M. Pollnau, "Erbium-doped integrated waveguide amplifiers and lasers," *Laser & Photonics Reviews*, vol. 5, no. 3, pp. 368–403, May 2011. [Online]. Available: http://onlinelibrary.wiley.com/doi/10.1002/lpor.201000015/abstract

[107] J. Malowicki, M. Fanto, M. Hayduk, and J. P.J. Delfyett, "Harmonically mode-locked glass waveguide laser with 21-fs timing jitter," *Photonics Technology Letters, IEEE*, vol. 17, no. 1, pp. 40 –42, Jan. 2005.

[108] B. Callicoatt, J. Schlager, R. Hickernell, R. Mirin, and N. Sanford, "Compact solid-state waveguide lasers," *Circuits and Devices Magazine, IEEE*, vol. 19, no. 5, pp. 18 – 27, Sep. 2003.

[109] J. Schlager, B. Callicoatt, R. Mirin, and N. Sanford, "Passively mode-locked waveguide laser with low residual jitter," *Photonics Technology Letters, IEEE*, vol. 14, no. 9, pp. 1351 –1353, Sept. 2002.

[110] J. B. Schlager, B. E. Callicoatt, R. P. Mirin, N. A. Sanford, D. J. Jones, and J. Ye, "Passively mode-locked glass waveguide laser with 14-fs timing jitter," *Optics Letters*, vol. 28, no. 23, pp. 2411–2413, Dec. 2003. [Online]. Available: http://ol.osa.org/abstract.cfm?URI=ol-28-23-2411

[111] E. Thoen, E. Koontz, D. Jones, F. Kärtner, E. Ippen, and L. Kolodziejski, "Erbium-ytterbium waveguide laser mode-locked with a semiconductor saturable absorber mirror," *Photonics Technology Letters, IEEE*, vol. 12, no. 2, pp. 149 –151, Feb. 2000.

[112] G. Della Valle, R. Osellame, G. Galzerano, N. Chiodo, G. Cerullo, P. Laporta, O. Svelto, U. Morgner, A. G. Rozhin, V. Scardaci, and A. C. Ferrari, "Passive mode locking by carbon nanotubes in a femtosecond laser written waveguide laser," *Applied Physics Letters*, vol. 89, no. 23, pp. 231 115–231 115–3, Dec. 2006. [Online]. Available: http://apl.aip.org/resource/1/applab/v89/i23/p231115_s1

[113] S. J. Beecher, R. R. Thomson, N. D. Psaila, Z. Sun, T. Hasan, A. G. Rozhin, A. C. Ferrari, and A. K. Kar, "320 fs pulse generation from an ultrafast laser inscribed waveguide laser mode-locked by a nanotube saturable absorber," *Applied Physics Letters*, vol. 97, no. 11, pp. 111 114–111 114–3, Sep. 2010. [Online]. Available: http://apl.aip.org/resource/1/applab/v97/i11/p111114_s1

[114] D. Jones, S. Namiki, D. Barbier, E. Ippen, and H. Haus, "116-fs soliton source based on an Er-Yb codoped waveguide amplifier," *Photonics Technology Letters, IEEE*, vol. 10, no. 5, pp. 666–668, May 1998.

[115] J. Shmulovich, A. Bruce, G. Lenz, P. Hansen, T. Nielsen, D. Muehlner, G. Bogert, I. Brener, E. Laskowski, A. Paunescu, I. Ryazansky, D. Jacobson, and A. White, "Integrated planar waveguide amplifier with 15 dB net gain and 1550 nm," *Optical Fiber Communication Conference (OFC)*, vol. 13, no. 16, pp. PD42-1 3, 1999.

[116] H. Byun, "Integrated high-repetition-rate femtosecond lasers at 1.55 μm," Ph.D. dissertation, Massachusetts Institute of Technology, 2010.

[117] E. Wu, "Measuring chromatic dispersion of single-mode optical fibres using white light interferometry," Master of Science, The University of Auckland, 2006.

[118] R. M. Knox and P. Toulios, "Integrated circuit for millimeter through optical frequency range," in *Proceedings of MRI Symposium on Submillimeter Waves*, Brooklyn, 1970, pp. 497 – 516.

[119] G. B. Hocker and W. K. Burns, "Mode dispersion in diffused channel waveguides by the effective index method," *Applied Optics*, vol. 16, no. 1, pp. 113–118, Jan. 1977. [Online]. Available: http://ao.osa.org/abstract.cfm?URI=ao-16-1-113

[120] C. Kim, B. Jung, and C. Lee, "Analysis of dielectric rectangular waveguide by modified effective-index method," *Electronics Letters*, vol. 22, no. 6, pp. 296 –298, 1986.

[121] K. S. Chiang, "Dual effective-index method for the analysis of rectangular dielectric waveguides," *Applied Optics*, vol. 25, no. 13, pp. 2169–2174, Jul. 1986. [Online]. Available: http://ao.osa.org/abstract.cfm?URI=ao-25-13-2169

[122] K. Okamoto, "Chapter 2 - planar optical waveguides," in *Fundamentals of Optical Waveguides (Second Edition)*. Burlington: Academic Press, 2006, pp. 13–55. [Online]. Available: http://www.sciencedirect.com/science/article/pii/B9780125250962500039

[123] H. Kogelnik and V. Ramaswamy, "Scaling rules for thin-film optical waveguides," *Appl. Opt.*, vol. 13, no. 8, pp. 1857–1862, Aug 1974. [Online]. Available: http://ao.osa.org/abstract.cfm?URI=ao-13-8-1857

[124] Q. Bao, H. Zhang, Y. Wang, Z. Ni, Y. Yan, Z. X. Shen, K. P. Loh, and D. Y. Tang, "Atomic-layer graphene as a saturable absorber for ultrafast pulsed lasers," *Advanced Functional Materials*, vol. 19, no. 19, pp. 3077–3083, 2009. [Online]. Available: http://dx.doi.org/10.1002/adfm.200901007

[125] Z. Sun, T. Hasan, F. Torrisi, D. Popa, G. Privitera, F. Wang, F. Bonaccorso, D. M. Basko, and A. C. Ferrari, "Graphene mode-locked ultrafast laser," *ACS Nano*, vol. 4, no. 2, pp. 803–810, 2010, pMID: 20099874. [Online]. Available: http://pubs.acs.org/doi/abs/10.1021/nn901703e

[126] F. Kärtner, J. der Au, and U. Keller, "Mode-locking with slow and fast saturable absorbers - What's the difference?" *Selected Topics in Quantum Electronics, IEEE Journal of*, vol. 4, no. 2, pp. 159–168, Mar. 1998.

[127] S. N. Tandon, J. T. Gopinath, T. R. Schibli, G. S. Petrich, L. A. Kolodziejski, F. X. Kaertner, and E. P. Ippen, "Saturable absorbers with large area broadband bragg reflectors for femtosecond pulse generation," in *Conference on Lasers and Electro-Optics/Quantum Electronics and Laser Science Conference*. Optical Society of America, 2003, p. CWM5. [Online]. Available: http://www.opticsinfobase.org/abstract.cfm?URI=CLEO-2003-CWM5

[128] S. N. Tandon, J. T. Gopinath, H. M. Shen, G. S. Petrich, L. A. Kolodziejski, F. X. Kärtner, and E. P. Ippen, "Large-area broadband saturable bragg reflectors by use of oxidized AlAs," *Opt. Lett.*, vol. 29, no. 21, pp. 2551–2553, Nov 2004. [Online]. Available: http://ol.osa.org/abstract.cfm?URI=ol-29-21-2551

[129] S. Nabanja, M. Y. Sander, J. Morse, K. Shtyrkova, G. S. Petrich, L. A. Kolodziejski, F. X. Kärtner, and E. P. Ippen, "Widely tunable large area SBR for ultra-short pulse generation," in *Conference on Lasers and Electro-Optics (CLEO) and Quantum Electronics and Laser Science Conference (QELS), San Jose, CA, May 6-12, 2012, CF3L.4.*

[130] U. Keller, K. J. Weingarten, F. X. Kärtner, D. Kopf, B. Braun, I. D. Jung, R. Fluck, C. Hönninger, N. Matuschek, and J. Aus der Au, "Semiconductor saturable absorber mirrors (SESAMs) for femtosecond to nanosecond pulse generation in solid-state lasers," *Special issue on Ultrafast Electronics, Photonics and Optoelectronics, IEEE J. Selected Topics in Quantum Electronics (JSTQE)*, vol. 2, no. 3, pp. 435–453, 1996.

[131] J. T. Gopinath, "Studies of third-order nonlinearities in materials and devices for ultrafast lasers," Ph.D. dissertation, Massachusetts Institute of Technology, 2005.

[132] J. T. Gopinath, E. R. Thoen, E. M. Koontz, M. E. Grein, L. A. Kolodziejski, E. P. Ippen, and J. P. Donnelly, "Recovery dynamics in proton-bombarded semiconductor saturable absorber mirrors," *Applied Physics Letters*, vol. 78, no. 22, pp. 3409–3411, 2001.

[133] T. Hakkarainen, E.-M. Pavelescu, K. Arstila, V. D. S. Dhaka, T. Hakulinen, R. Herda, J. Konttinen, N. Tkachenko, H. Lemmetyinen, J. Keinonen, and M. Pessa, "Optical properties of ion irradiated and annealed InGaAs/GaAs quantum wells and semiconductor saturable absorber mirrors," *Journal of Physics D: Applied Physics*, vol. 38, no. 7, p. 985, 2005.

[134] Y. Silberberg, P. W. Smith, D. A. B. Miller, B. Tell, A. C. Gossard, and W. Wiegmann, "Fast nonlinear optical response from proton-bombarded multiple quantum well structures," *Applied Physics Letters*, vol. 46, no. 8, pp. 701–703, 1985.

[135] S. Campbell, *The Science and Engineering of Microelectronic Fabrication.* Oxford University Press, 2001.

[136] M. W. Focht, A. T. Macrander, B. Schwartz, and L. C. Feldman, "High resistivity in InP by helium bombardment," *Journal of Applied Physics*, vol. 55, no. 10, pp. 3859–3862, 1984. [Online]. Available: http://link.aip.org/link/?JAP/55/3859/1

[137] E. Kamaratos, "Developments regarding the bragg rule for stopping power and critical examination of its application to water," *Nuclear Instruments and Methods in Physics Research*, vol. 215, no. 12, pp. 337–344, Sep. 1983. [Online]. Available: http://www.sciencedirect.com/science/article/pii/0167508783913261

[138] D. Groom and S. Klein, "Passage of particles through matter," *The European Physical Journal C - Particles and Fields*, vol. 15, no. 1, pp. 163–173, Mar. 2000. [Online]. Available: http://www.springerlink.com/content/m321677145684107/abstract/

[139] Z. James F., "SRIM-2003," *Nuclear Instruments and Methods in Physics Research Section B: Beam Interactions with Materials and Atoms*, vol. 219220, no. 0, pp. 1027–1036, 2004.

[140] A. Motamedi, "Ultrafast nonlinear optical properties of passive and active semiconductor devices," Ph.D. dissertation, Massachusetts Institute of Technology, 2011.

[141] J. Donnelly and F. Leonberger, "Multiple-energy proton bombardment in n+-GaAs," *Solid-State Electronics*, vol. 20, no. 3, pp. 183–189, Mar. 1977.

[142] J. A. Kong, *Electromagnetic Wave Theory.* EMW Publishing, 2000.

[143] M. Guizar-Sicairos and J. C. Gutiérrez-Vega, "Computation of quasi-discrete hankel transforms of integer order for propagating optical wave fields," *J. Opt. Soc. Am. A*, vol. 21, no. 1, pp. 53–58, Jan 2004. [Online]. Available: http://josaa.osa.org/abstract.cfm?URI=josaa-21-1-53

[144] L. Yu, M. Huang, M. Chen, W. Chen, W. Huang, and Z. Zhu, "Quasi-discrete hankel transform," *Opt. Lett.*, vol. 23, no. 6, pp. 409–411, Mar 1998. [Online]. Available: http://ol.osa.org/abstract.cfm?URI=ol-23-6-409